Max-Planck-Institut für Meteorologie

EXAMENSARBEIT Nr. 81
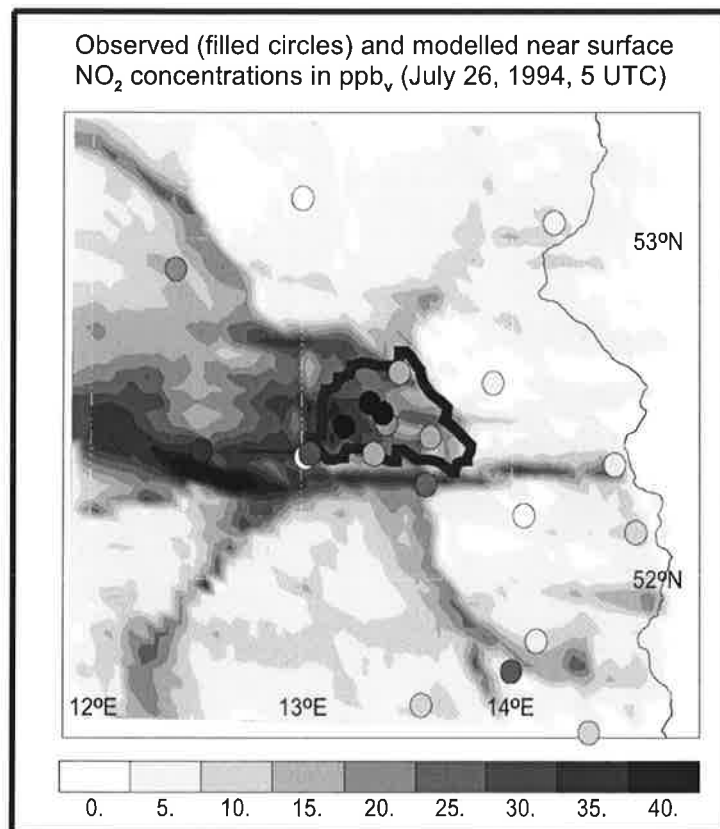
Observed (filled circles) and modelled near surface NO_2 concentrations in ppb_v (July 26, 1994, 5 UTC)

53°N

52°N

12°E   13°E   14°E

0.   5.   10.   15.   20.   25.   30.   35.   40.

PHOTOCHEMICAL SMOG IN BERLIN-BRANDENBURG: AN INVESTIGATION WITH THE ATMOSPHERE-CHEMISTRY MODEL GESIMA

by

Susanne Elisabeth Bauer

HAMBURG, December 2000

Dissertation zur Erlangung des Doktorgrades

Autor:

Susanne Elisabeth Bauer

Max-Planck-Institut
für Meteorologie

MAX-PLANCK-INSTITUT
FÜR METEOROLOGIE
BUNDESSTRASSE 55
D - 20146 HAMBURG
GERMANY

Tel.:   +49-(0)40-4 11 73-0
Telefax: +49-(0)40-4 11 73-298
E-Mail: <name> @ dkrz.de

Photochemical Smog in Berlin-Brandenburg: An Investigation with the Atmosphere-Chemistry Model GESIMA

Dissertation
zur Erlangung des Doktorgrades
der Naturwissenschaften
in Fachbereich Geowissenschaften
der Universität Hamburg

vorgelegt von
Susanne Elisabeth Bauer
aus Darmstadt

Hamburg
2000

Abstract

This thesis presents an analysis of a pollution episode in an urban atmosphere, using a complex model system. The model system simulates the atmospheric conditions during a measurement campaign, called FLUMOB, in July 1994 in the area of Berlin-Brandenburg during a distinct summer smog situation.

The model system consists of a non-hydrostatic atmosphere-chemistry model that is nested into a coarser regional atmosphere-chemistry model which, in turn, is embedded in an even coarser framework. Thus, a chain of mesoscale atmosphere-chemistry models is applied to the regions of Europe, Germany and Berlin-Brandenburg, respectively. The simulation at the highest resolution is used to analyse the polluted urban atmosphere in Berlin-Brandenburg while the observational data sets are used for model evaluation.

The analysis of the field measurements made during the FLUMOB campaign shows that naturally emitted hydrocarbons play the dominant role in the ozone formation in Berlin-Brandenburg. The composition of non-methane volatile organic compounds in the investigated area is dominated (70-80%) by biogenically emitted hydrocarbons. During the analysed case, ozone formation was sensitive to hydrocarbon concentrations so that the ozone production was limited by the availability of hydrocarbons and thus especially by the amount which were biogenically emitted. Furthermore it is shown that the FLUMOB episode was influenced by elevated concentrations of ozone in the free troposphere. In contrast to previous analysis the importance of ozone produced outside Europe is stressed. In spite of the stagnant high pressure situation which occurred during the FLUMOB episode, Germany was significantly influenced by long-range transport of ozone. This transport also influenced the near surface ozone concentrations.

The model evaluation suggests the high quality of simulated urban ozone and nitrogen species and hence of the anthropogenic emission inventory. The total amount of ozone is, however, underpredicted by the model for two reasons: Underprediction of biogenic hydrocarbon emissions and uncertainties of the chemical information at the lateral boundaries of the European domain.

Contents

1 Introduction

The Earth's atmosphere is a complex physical and chemical system interacting with the oceans, the continents, the biosphere and living organisms. It is also increasingly affected by human activity. To understand the atmosphere, all these subsystems have to be investigated and impacts and feedbacks have to be taken into account. Changes of one parameter of a subsystem can potentially influence and change the whole Earth system. One key parameter through which all these subsystems are coupled is the atmospheric composition. The major chemical components of the Earth's atmosphere are nitrogen (78%), oxygen (21%), water and the noble gas argon. The remaining gaseous constituents, the trace species, comprise less than 1% of the atmosphere. These trace species are those which are directly responsible for significant changes in the Earth atmosphere. These chemical trace substances are released at the earth's surface as a result of natural and anthropogenical activities. Furthermore they undergo transformation and removal processes which in turn depend on the physical and biological state of the system. The chemical composition has evolved in response to changes in natural biogeochemical cycles. The composition of the atmosphere is known to have continuously evolved since the formation of the Earth some 4.6 billion years ago. Changes, however, have accelerated during the last century as the result of human activities. Humans effects have, for example, altered the atmospheric concentration of relatively long-lived trace gases such as methane, nitrous oxide and some halogen species. These changes are believed to have influenced directly or indirectly the physical state of the atmosphere through chemical and radiative processes. Greenhouse gases, which absorb infrared radiation impact climate by altering the radiative balance of the atmosphere. Human activities also lead to enhanced release of nitrogen oxides, carbon monoxide and a variety of hydrocarbons from fossil fuel and biomass burning. These gases effect the oxidizing or self-cleaning capacity of the atmosphere, i.e. the ability of the atmosphere to oxidize chemical species into partly water soluble compounds that can be more rapidly removed from the atmosphere. The formation rate of tropospheric ozone, a gas with severe consequences on biological productivity and human health has been enhanced by these changes in the atmospheric composition.

The changing atmosphere rises air quality as one of the prominent environmental issues of the last and the current century. It is increasingly recognized that changes in the emissions of chemicals associated with evolving land-use (including agricultural practices, biomass burning) and industrial development (including urbanization and transportation) are becoming major causes of global changes in the Earth system. The industrial development leads to urban smog: The first recognized type of air pollution was that characterized by high concentrations of sulfur compounds and particles, resulting from the combustion of coal and high-sulfur containing fuels. Cities with this type of air pollution are often located in cold climates where electric power generation and domestic heating are major sources of emissions. It occurs typically during the winter season when a high pressure situation suppresses the exchange of polluted air masses through a strong surface inversion layer. A second type of urban air pollution is attributed to traffic emissions. This problem was first recognized in Los Angeles around 1945 and now occurs worldwide in any metropolitan area. This type of air pollution has received the name of photochemical smog. Photochemical smog develops under summer conditions, during high temperatures, strong solar radiation and stagnant weather episodes. The main primary pollutants are rapidly converted into secondary pollutants, including ozone, organic nitrates and other oxidized hydrocarbons. These secondary pollutants are responsible for adverse effects such as

health and plant damages. Ozone is naturally present in the clean lower troposphere at mixing ratios ranging from 10 to 30 ppb_v. During photochemical smog events these values reach much higher concentrations. For example, ozone mixing ratios exceeding 400 ppb_v have been occasionally observed in Los Angeles.

The increased concentrations of tropospheric ozone and of other oxidants rises the problem of emission control strategies. The German government has defined the following ozone limiting values:

Table 1.1: Ozone limiting values

Objective	Mean average interval [h]	Threshold value [ppb_v]
health protection	8	55
protection of vegetation	1	100
	24	30
public information	1	90
smog alarm	1	120
public warning	1	180

It is important to analyse natural and anthropogenic air pollutant precursors to create effective emission control strategies. In case of the winter smog phenomena, regulations concerning sulfur emission reduction due to emission filtering have been successful. In case of the photochemical smog, peak ozone concentrations seem to have decreased during the last years but the background ozone level has increased. A annual increase of 1-2% in Europe has been observed in the past 30 years (*Seinfeld and Pandis*, 1998). Filtering methods, for example installation of catalysts in vehicles, are counterbalanced by increasing emissions due to industrialization and mobility. The observed increasing amounts of background ozone demonstrate that air pollution is not limited to the regional scale. From the global point of view it is important to analyse the impact of regional ozone formation on the global tropospheric ozone budget and thus on changes on the oxidizing capacity of the troposphere.

1.1   Air Pollution Chemistry

Today in many major urban areas around the world, air pollution is characterized by the formation of ozone. In these regions the high concentrations of ozone arise from high emissions of NO_x (mainly NO) and hundreds of reactive hydrocarbons (including alkanes, alkenes and aromatics). The hydrocarbons are emitted as a result of a range of human activities including combustion, fuel evaporation, solvent use, and chemical manufacturing. They are also released by vegetation.

The time depending relationship between precursors and oxidation products in a urban atmosphere during a summer smog situation is illus-
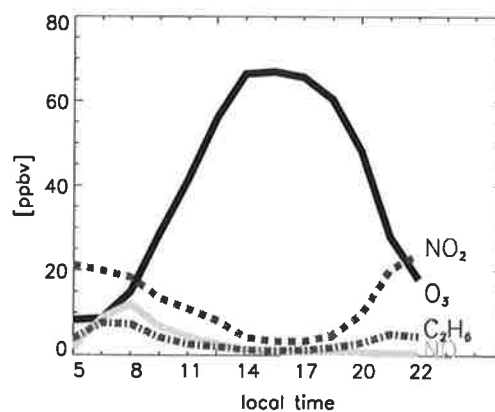
Figure 1.1: Diurnal variation of NO, NO_2, O_3 and C_2H_6 in Berlin on July 23, 1994.

trated in Fig. 1.1: In the early morning, high NO_2 concentrations occur which have accumulated during the night in the absence of photochemical transformation. The concentration of NO increases due to traffic emissions and reaches a maximum during the morning rush hour. The concentrations of hydrocarbon species also increase during the morning hours (e.g. ethane (C_2H_6)). Due to the fast conversion of NO to NO_2, and the conversion of NO_2 and the hydrocarbons to oxidant species, the precursor species, here NO_x and C_2H_6, decrease during the day. Oxidant (e.g. ozone) levels which are relatively low in the early morning increase significantly about noon due to photochemical transformation when the NO conversion is low and the concentrations of hydrocarbons starts to decrease. Ozone concentrations can also increase during the day due to transport processes, e.g vertical mixing. In the late afternoon hours ozone starts to decrease due to NO titration, deposition and mixing processes.

A simplified view of the complex radical cycle is presented in Fig. 1.2. The reaction sequence is initialized by photolysis of ozone and the subsequent reaction between atomic oxygen ($O(^1D)$) and water vapor (H_2O) which produces the hydroxyl radical (OH). This radical reacts with most trace species leading to their oxidation which enables their final removal from the atmosphere by dry and wet deposition. During day time OH is generated in a catalytic cycle including additional radicals. In presence of hydrocarbons (HC) or carbon monoxide (CO), peroxy radicals (RO_2) or the hydroperoxyl radical (HO_2) can be formed. Further reactions initiated by HO_2 or RO_2 radicals determine whether the OH cycle is closed by regeneration of OH under consumption of an ozone molecule. This situation prevails in the clean atmosphere. When significant quantities of NO are present, the preferred reaction path leads to the formation of ozone. This
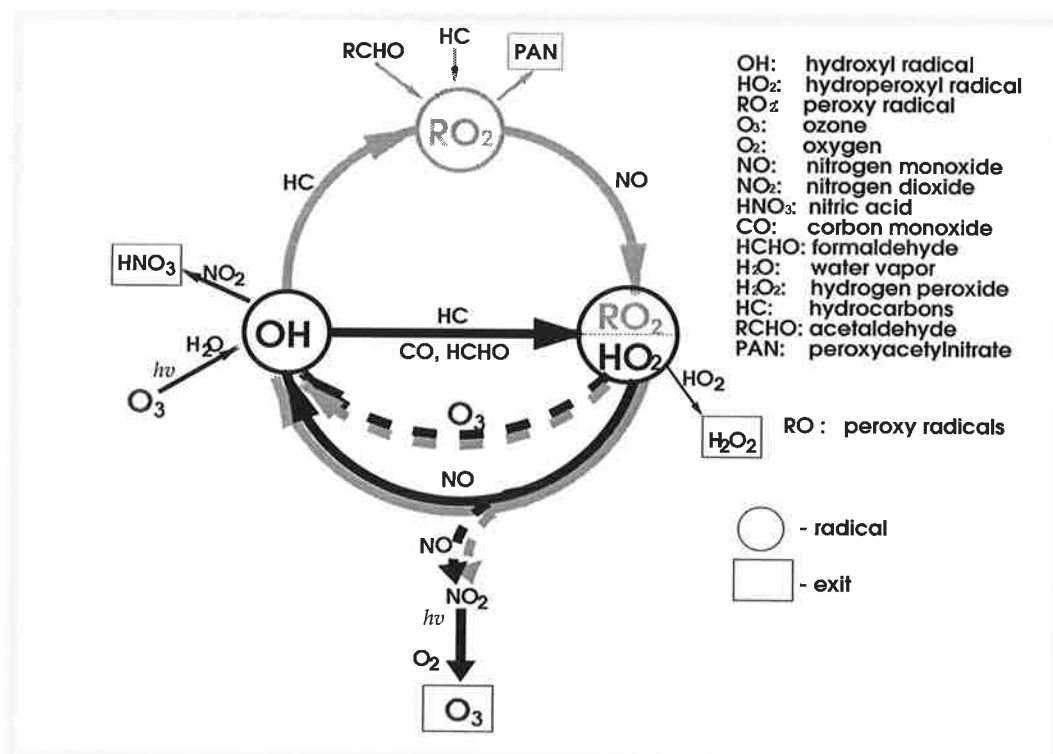
Figure 1.2: OH cycle

situation characterizes the polluted atmosphere. In general, the rate of ozone production is dependent on the HC/NO$_x$ ratio. When this ratio is low (i.e. the averaged urban mixing ratio of HC and NO$_x$ is approximately less then 5.5/1 (*Seinfeld and Pandis*, 1998)) OH reacts predominantly with NO$_2$, removing radicals and retarding ozone formation. Under these conditions a decrease in NO$_x$ concentrations favor ozone formation. At a sufficiently high HC/NO$_x$ ratio, a further decrease in NO$_x$ retard ozone formation. Thus, the relationship of ozone with HC and NO$_x$ is far from being linear and depends on the prevailing HC/NO$_x$ concentration ratio.

The OH radical cycle is active during daytime only because of the involved photochemical reactions. After sunset, nitrogen dioxide becomes the dominant sink for ozone. Due to this reaction the nitrate radical (NO$_3$) is formed which reacts with NO$_2$ to produce dinitrogen pentoxide (N$_2$O$_5$) which in turn is a source of NO$_2$ and NO$_3$.

1.2 Tools to Analyse Atmospheric Chemistry

The composition of the atmosphere is studied by observations and theoretical analysis to understand and potentially address serious environmental problems. Atmospheric trace gases are observed from satellites, aircraft and ground base measurements. Surface concentrations are monitored from ground stations, ships and buoys. Vertical profiles are observed by radiosonde and LIDAR (Light Detecting and Ranging). This large amount of measurements needs to be organized and managed. Different programs exist mostly coordinated under the World Meteorological Organization (WMO). For example global observations are managed by the Global Atmosphere Watch (GAW) program. The objective of GAW is to monitor the long-term evolution of the atmospheric composition on global and regional scales in order to assess the contribution to climate change and environmental issues. Several other organizations and global networks also contribute to the atmospheric observation of the chemical composition. On the regional scale, organizations like for example EMEP (European Monitoring and Evaluation Program) provide a cooperative program for the monitoring and evaluating the long term range air pollutants in Europe. Air quality is also studied by individual countries, e.g. in Germany by the 'Umweltbundesamt' or by environmental organizations of the German states ('Bundesländer'). An important source of observations at high temporal and spatial resolution is provided by field campaigns. These campaigns, however, focus on a specific scientific question during a limited period of time. The number of observed species differ strongly within the observation programs. Many organizations focus on ozone measurements only (total column, vertical profile and near surface concentrations). Other include the measurements of a wide range of trace gas concentrations including aerosols. Although many trace species measurements and a lot of coordinating programs exist, the quantity and quality of these data sets are not comparable to meteorological observations carried out operationally and assimilated by numerical models. Nevertheless, only observations monitor the real state and the composition of the atmosphere. Further understanding can be obtained by numerical model studies because models are tools that integrate our understanding of atmospheric processes and their interactions.

A wide variety of numerical models exists to study atmospheric processes, including statistical, Eulerian or Lagrangian models. The following brief model overview concentrates on three-dimensional Eulerian formulations. These models can be roughly categorized as global-, regional-, local- or micro- scale models, depending on the spatial scale they are designed for.

With increasing spatial and thus temporal resolution, the models resolve atmospheric processes with more details. Subgrid scale process parameterizations in larger scale low resolution models, e.g. convection, turbulence or non-hydrostatic effects, are more explicitly formulated in higher resolving models. Higher model resolutions as well as the very detailed parameterizations often lead to a restriction of the area covered by the model domains and the length of the simulation period limited by the available computer power. Global climate models, for example, are designed to simulate decades or centuries and reproducing the mean state of the atmosphere, while microscale models are applied only for a few hours but simulate atmospheric processes with considerable details. High resolution limited area models raise the question of suitable lateral boundary information when the model is applied to realistic atmospheric conditions. A solution to this problem is provided by the nesting of a limited area simulation in a coarser larger scale model simulation or by the constrain of the model by observational data sets.

Chemical processes included in three-dimensional models also depend an the temporal and spatial scale of the problem to be studies. 'Off-line' and 'on-line' atmosphere-chemistry models have been developed to study mainly chemical or combined meteorological and chemical aspects. Chemistry transport models (CTM) are operating in the 'off-line' mode. Thus meteorological information, e.g. wind or temperature fields, are calculated separately (or provided from meteorological analysis) and are provided externally at specified time intervals (e.g., every 6 hours) to the CTM. MOZART (*Brasseur et al.*, 1998; *Hauglustaine et al.*, 1998), for example, is a global CTM for ozone and related chemical tracers. On the regional scale many CTM's exist. One example is the EURAD (European Acid Deposition Model) (*Hass*, 1991) system which also includes nesting facilities to focus on smaller areas with a higher spatial resolution. In contrast to 'off-line' calculations 'on-line' models calculate meteorological and chemical processes simultaneously. High frequency dynamical processes, like turbulence or convection, and physical quantities are provided in much more detail for the calculation of transformation, transport and deposition of the chemical species. This advantage is especially of importance for high resolving models which include turbulent processes in detail. However, the major advantage of 'on-line' modelling is that chemical-physical interactions can be investigated. This is not possible when the meteorological and chemical processes are calculated separately. Scientific questions related to climate change, aerosol - radiation - cloud interactions and feedbacks can be analysed from 'on-line' model runs. Examples for 'on-line' modelling are the climate change studies performed by global GCM's, e.g. the ECHAM (*Roelofs and Lelieveld*, 1995), (*Roeckner et al.*, 1999) or the GISS GCM model (*Shindell et al.*, 2000) but including only a rather simple chemistry. Examples at the regional scale are the Canadian-regional climate model (CRM) (*Bouchet et al.*, 1999a,b) or at even higher resolution the non-hydrostatic atmosphere-chemistry model MESO-NH-C Model (*Tulet et al.*, 1999; *Crassier et al.*, 2000).

Although, many numerical models based on similar theoretical concepts exist, theses models often differ substantially due to differences in the complexity of chemical mechanism, emission modules, physical parameterizations or numerical solution techniques. The number of regional scale gas-phase chemical mechanisms used in CTMs is high, e.g. *Derwent* (1990) has compared 24 of them.

1.3 Approach and Emphasis of this Thesis

In this thesis, the polluted urban atmosphere in Berlin-Brandenburg is investigated. Berlin was chosen because it represents atmospheric conditions of a German city and thus differs substantially from other intensively investigated smog regions, e.g. Los Angeles, Athens or Mexico D.F. due to its climatic conditions and the composition of emissions. In Germany summer smog events occur episodically strongly dependent on the weather conditions. In comparison to the above mentioned megacities Berlin is not a 'smog-city'. Photochemical air pollution also occur in many other German cities (e.g. Munich, Rhine-Ruhr area). However, Berlin was chosen for this investigation because it is located in a rural environment. Therefore it is expected that the transport and transformation of urban air pollution caused by the city of Berlin can be easily analysed. The observational data sets used for this study are monitored during a summer smog field experiment. Thus the analysis of the observed quantities, which have been monitored by the measurement campaign (mostly ozone and nitrogen oxide), with the model studies enables the understanding of the complex interactions between multitudes of chemical species. Furthermore the interactions between emission, transformation, transport, and deposition processes are included in this analysis.

The emphasis of this thesis is to analyse a summer smog event in Berlin-Brandenburg with a complex atmosphere-chemistry model. Furthermore, the observations are used to validate the new model system. Validation is fundamental for all further model applications, e.g. forecast, hindcast, scenario or process oriented studies, because, through this process, the ability of the model to reproduce the real atmosphere is tested. As models become more and more complex, their ability to reproduce reality increases but, at the same time, the number of degrees of freedom increase together with the number of model parameters. A model validation has to be carried out before reliable model predictions or any other applications can be carried out.

The tool of this thesis is the new non-hydrostatic 'on-line' atmosphere-chemistry model GESIMA (Geesthachter Simulations Modell der Atmosphäre). This model is embedded through a one-way nesting in a coarser hydrostatic atmosphere-chemistry model simulation at the regional scale, the REMO model (Regional Modell) which inturn is embedded in another coarser resolution (Fig. 3.1). One-way nesting means that only information from the coarser model is transfered to the model operating at the smaller scale. Altogether, the models present an 'on-line' atmosphere-chemistry model chain covering the meso-α, β and γ scales. Horizontal gridpoint distances vary between 50 - 4 km and model domains between 3000 km$\times$3000 km to 200 km $\times$200 km, respectively. The gas-phase chemistry mechanism RADM II (Regional Acid Deposition Model) (*Stockwell et al.*, 1990) has been selected to be included in both models, REMO and GESIMA. RADM II is a state-of-the-art reaction mechanism designed to represent chemical processes in the clean and polluted atmosphere.

In this study the model is validated with the measurement data sets monitored during the FLU-MOB (Flugzeug und Boden Messungen von Ozon und Vorläuferstoffen zur Abschätzung der Wirksamkeit von emissionsmindernden Maßnahmen im Großraum Berlin-Brandenburg) (*Stark et al.*, 1995) field experiment, carried out in Berlin-Brandenburg in summer 1994. The aim of this measurement campaign was to measure the three-dimensional distribution of the concentrations of ozone and its precursors during a summer smog situation and to create a data sets

for the validation of photochemical models. The FLUMOB project also included model studies with the aim of studying emission control strategies for ozone reduction. FLUMOB was one of a series of investigations (*Bruckmann and Wichmann-Fiebig*, 1997) focusing on summer smog events to analyse proposed governmental ozone reduction strategies (*Bruckmann et al.*, 1997). The FLUMOB experiment was chosen as a validation case for the following reasons:

- The measurements monitored a distinct summer smog situation.

- Measurement data sets are available for a period of one week so that longer simulations, including several case studies, can be carried out, which increase the statistical significance of the validation.

- The data sets have been available for validation.

- Anthropogenic emission inventories have been determined to be adaptive to the domain and the time of the field experiment.

Earlier numerical experiments, which have been carried out in connection with the FLUMOB project in 1994 (*Mieth et al.*, 1995; *Rufeger and Mieth*, 1998), used the transport model REGO-ZON (*Heimann*, 1985) with the CBM-IV chemistry mechanism (*Gery et al.*, 1989). REGOZON is a simple three-layer model applied episodically for daytime hours and driven by external meteorological data sets. The model calculations in those studies were carried out with and without assumed short term reduction measures in the city of Berlin. The following main conclusions as discussed in *Mieth et al.* (1995); *Stark et al.* (1995); *Bruckmann and Wichmann-Fiebig* (1997) are drawn from the numerical experiments of the FLUMOB project:

- Large cities can show distinct ozone plumes in the downwind direction with an increase in ozone maximum concentrations of 15-40% above background ozone.

- Ozone maximum concentrations and the size and duration of the ozone plume can be reduced by short term abatement actions, but the effects depend on circumstances, for example, the background ozone level.

- An effective strategy to lower the ozone burden must combine extended (European scale) and regional action.

- Analysis of smog situations and reduction scenarios have to be carried out in nested simulations.

The results of these investigations are based on simple model studies. More complex experiments are therefore needed before final conclusions can be drawn. The study which will be presented in the following chapters differs substantial from the earlier model analysis. Some basic improvements have been included in one model formulation:

- A complex meteorological model is included.

- An advanced chemistry mechanism is used and included 'on-line'.

- The model simulations are meteorologically and chemically nested.

- The coarsest resolution captures the European scale.

- The modelling domain is resolved with high resolution in the horizontal and the vertical direction.

- Anthropogenic and biogenic emissions are considered in much more detail.

- A one week simulation is carried out through a continuous model integration.

The study emphasizes the following questions: Which results can be drawn from the FLUMOB field campaign when analysing the observations with a complex regional model system ? What is the model performance when validated against ambient observations ?

The new model system will be described in chapter 2 focussing on the description of the chemistry routines implemented in the non-hydrostatic model. The configuration of the model system and a description of the chosen nesting techniques is presented in chapter 3. A brief validation of the meteorological parameters is given in chapter 4. Here the main interest concentrates on the statistical evaluation. Chemistry is validated in detail in chapter 5. After a statistical analysis, the process of ozone formation is investigated in detail. The process of local ozone formation during one day is studied by analysing the HC/NO_x regimes and another day, at the end of the summer smog event, is chosen with photochemically aged air masses. The larger regional scale conditions and their impact on the GESIMA simulation are analysed in chapter 6. Long range transport is analysed and a sensitivity study investigates the influence of lateral boundary information of ozone on the model operating on the smallest scale. A further sensitivity study analyses the summer haze aerosol effect in chapter 7. Final conclusion and further studies are motivated in chapter 8.

2 Model Description

2.1 General Concept

The general concept behind this model approach is to create a three-dimensional Eulerian atmosphere-chemistry model on the meso-γ scale that is embedded in a coarser atmosphere-chemistry model simulation to ensure that the model results are not dominated by artificial information at the lateral model boundaries. Therefore, this work is part of the development of a mesoscale atmosphere-chemistry model chain where the smaller scale simulations are one-way nested in a coarser simulation. Ideally, the coarsest model should operate on the global scale. But for this study no global atmosphere-chemistry simulation reproducing the real weather condition including tropospheric chemistry was available, so that the nesting into a global simulation has to be a part of the future work. The meso-α and meso-β scale resolving typical horizontal length scales of about 250 - 2500 km and 25 - 250 km (*Wippermann*, 1981), respectively, are resolved by the hydrostatic atmosphere-chemistry model REMO. On the smaller meso-γ scale resolving length scales between 2.5 and 25 km the non-hydrostatic atmosphere-chemistry model GESIMA is applied.

Higher spatial and temporal resolution enables more detailed mathematical formulations of physical processes. In the dynamics this leads to the introduction of the non-hydrostatic formulation (*Pielke*, 1984). *Orlanski* (1981) showed that the hydrostatic approximation is not valid when the grid size is smaller than 8 km. Certainly, this grid size dependence is also influenced by the geographical situation and the meteorological conditions. In contrast to hydrostatic formulations the pressure and the vertical velocity are derived from the prognostic equations in an anelastic non-hydrostatic model (*Ogura and Phillips*, 1962). This is of fundamental importance for physical parameterizations because, for example, convection and turbulent fluxes are resolved in more detail by the non-hydrostatic model (*Tapp and White*, 1976; *Clark*, 1977; *Carpenter*, 1979; *Durran and Klemp*, 1983; *Golding*, 1990, 1992; *Kato*, 1997).

Thus the dynamical and physical parts of the REMO and the GESIMA model differ substantially. Both models include the same gasphase chemical mechanism RADM II. The gas-phase chemistry mechanism RADM II (Regional Acid Deposition Model) (*Stockwell et al.*, 1990) was selected for this model system because it includes a complex state of the art reaction system for the clean and polluted atmosphere and RADM II is a well tested mechanism used in many chemistry transport models. Additionally to the gas-phase chemistry, REMO determines chemical transformations in the aqueous phase which are not included in the GESIMA model. The denotation atmosphere-chemistry model indicates that the chemistry is included 'on-line' in the atmospheric models. The meteorological and chemical equations are solved simultaneously. When the chemical time step reaches the meteorological time step actual meteorological values such as pressure, temperature and humidity are used to calculate the reaction rates for chemical transformation. For advection, diffusion and dry deposition of the chemical species comprehensive turbulence information is available. Additionally, the 'on-line' technique offers the possibility to study interactions between the dynamics, physics and chemistry.

In chapter 2.2 and 2.3 the meso-γ scale atmosphere-chemistry model GESIMA is described in detail and a brief outline of the meso-α and meso-β atmosphere-chemistry model REMO is given in section 2.4.

2.2   Dynamics and Physics of the GESIMA Model

The GESIMA (Geesthacht Simulation Model of the Atmosphere) model includes various physical parameterization modules. For example the standard GESIMA version (*Kapitza*, 1999) includes two different soil schemes, three cloud (*Eppel et al.*, 1995; *Devantier and Raabe*, 1996) and two radiation schemes (*Eppel et al.*, 1995; *Rockel et al.*, 1991) of different complexity which can be selected according to the scientific question to be studied and to the amount of available computing time. Here only the physical parameterizations which are relevant for the adaption of the chemical parameterizations will be briefly described. A detailed description of the basic physical parameterizations included in GESIMA is given in *Eppel et al.* (1995) and in the model documentation manual (*Kapitza*, 1999).

Dynamics and Numerical Solution

GESIMA is a non-hydrostatic model whose detailed description of the dynamical part is given in *Kapitza and Eppel* (1992). This model is based on the anelastic equations (*Ogura and Phillips*, 1962) following the conservation laws for momentum, energy, and mass. For the numerical solution the thermodynamic variables are split into isentropic reference values which are assumed to be hydrostatic, and deviations. For the density the Boussinesq approximation is considered. The equations are transformed into terrain following coordinates in the vertical and the horizontal coordinates are orthogonal (*Anderson et al.*, 1984). For the discrete representation of the model variables a staggered grid (Arakawa-C) after *Mesinger and Arakawa* (1976) is used. Different numerical methods are used as the model equations contain parts (advection) which need explicit and other parts (Coriolis force, diffusion, etc.) which need implicit treatment. The prognostic equations are solved with a predictor / corrector scheme. The advection of the dynamical variables u, v, w and Θ is calculated with the MacCormack scheme (*Anderson et al.*, 1984). The Coriolis terms and the vertical diffusion are treated implicitly while the horizontal diffusion is calculated explicitly. The non-hydrostatic pressure is implicitly determined by the requirement that the flow field must fulfill the divergence equation. A conjugate gradient method is used to solve the Poisson equation for the non-hydrostatic pressure that appears when requiring the final-flux to be divergence-free (*Kapitza*, 1988; *Kapitza and Eppel*, 1987).

Transport of trace quantities

The scheme of *Smolarkiewicz* (1984) is used to calculate the transport of the trace quantities water vapor and the chemical species. This scheme uses a backward-difference approximation to preserve the positive-definiteness of the initial condition and an antidiffusion velocity to reduce numerical diffusion. The scheme is described in detail and tested for the GESIMA model in *Eppel et al.* (1995).

Turbulent Diffusion

The turbulent momentum fluxes are calculated using a first order closure scheme according to level 2.5 in the hierarchy of *Mellor and Yamada* (1974):

$$\tau_{ij} := -\langle u_i', u_j' \rangle = K_{ij} \left(\frac{\partial u_i}{\partial x_j} + \frac{\partial u_j}{\partial x_i} \right) \tag{2.1}$$

K_{ij} denotes the turbulent momentum exchange coefficient tensor, i and j are the index of the horizontal grid boxes, u_i' the deviation from the mean Cartesian velocity component, x_i the

coordinate direction. Mean values are used to parameterize the turbulent momentum flux in the first order scheme. Despite the deficits this approximation has, it is regarded appropriate to catch the essential features of a dynamical changing turbulent flow: advection of turbulence by shear, creation or destruction of turbulence by buoyancy, redistribution of turbulent energy by diffusion, and decay by dissipation. The complete diffusion scheme is given in *Eppel et al.* (1995).

Radiation

Two radiative transfer schemes of different complexity are implemented in GESIMA. The more simple scheme, 'Bakan scheme', is described in *Eppel et al.* (1995) and *Kapitza* (1999). This radiation scheme is used for the simulation of the entire FLUMOB episode which is discussed in chapter 4, 5 and 6. The more complex narrow band two stream radiation scheme (*Schmetz and Raschke*, 1979; *Schmetz*, 1984) with optical cloud properties after *Rockel et al.* (1991) is based on the two-stream method (*Kerschgens et al.*, 1978). This scheme is used in the aerosol sensitivity experiment (chapter 7). In this method the upward and downward radiation flux densities (M^+ and M^-) are calculated for a horizontally homogeneous plane-parallel geometry. For these fluxes two differential equations can be derived from the basic equation of radiative transfer (*Chandrasekhar*, 1960; *Zdunkowski et al.*, 1974). Assuming the cosines of the effective zenith angle, $\overline{\mu}^+$ for the upward flux and $\overline{\mu}^-$ for the downward diffuse flux to be equal, the differential equations are (*Schmetz and Raschke*, 1979):

$$\frac{\partial M^+(\delta)}{\partial \delta} = (1 - \tilde{\omega}(1-\beta))\frac{M^+(\delta)}{\overline{\mu}} - \tilde{\omega}\beta\frac{M^-(\delta)}{\overline{\mu}} - \tilde{\omega}\beta_0\mu_0 S_0 exp(-\delta/\mu_0) \qquad (2.2)$$

$$\frac{\partial M^-(\delta)}{\partial \delta} = \tilde{\omega}\beta\frac{M^+(\delta)}{\overline{\mu}} - (1 - \tilde{\omega}(1-\beta)\frac{M^-(\delta)}{\overline{\mu}} + \tilde{\omega}(1-\beta_0)\mu_0 S_0 exp(-\delta/\mu_0) \quad (2.3)$$

where $\tilde{\omega}$ stands for the single scattering albedo, δ for the vertical optical depth, μ_0 for the cosine of the solar zenith angle, S_0 for the solar constant, and β, β_0 for the fractions of backward scattering for the diffuse and direct beam radiation, respectively.

Surface and Soil Model

The calculation of fluxes at the surface is based on a bulk formulation (parameterizations for subgrid scale processes) in which latent heat fluxes are calculated by a simple force-restore method. The detailed surface and flux parameterizations are described in *Eppel et al.* (1995). Here, the 'Claussen surface scheme' is used (*Kapitza*, 1999). The soil layers are discretized in 4 levels with geometrically increasing thickness. The first layer is 1 cm deep and the lowest layer is about 1 m deep. GESIMA uses a total of 19 different surface classes. The classification is listed in Table 2.1 because of their relevance for the calculation of dry deposition and emission fluxes of the chemical species.

Table 2.1: Classification of land-use types

Type	Description	Type	Description
1	Water, e.g. open water (North Sea)	11	Agricultural area (sand, dry)
2	Water, e.g. coastal water (North Sea)	12	Sand-bank (usually dry)
3	Water, e.g. Baltic Sea	13	Sand-bank (flooded at high tide)
4	Water, e.g. lakes	14	Sandy mud-flats
5	Coniferous forest	15	Mud-flats
6	Mixed forest	16	Heather, bush-land, dwarf-pines
7	Deciduous forest	17	Peat swamp
8	Agricultural area (clay, marsh)	18	Urban areas
9	Agricultural area (sand, humid)	19	Central urban areas
10	Agricultural area (loam)		

2.2.1 Meteorological Information at the Model Boundaries

Limited area models have to receive information at the lateral and top boundaries of the model area. Different nudging techniques are provided by GESIMA. The appropriate technique to provide information at the lateral boundaries depends on the characteristics of the model domain, the nudged variables and the meteorological condition to be simulated. The following meteorological variables can potentially be nudged: potential temperature, specific humidity, horizontal wind components and pressure.

The following nudging formula is used implicitly:

$$f^{n+1} = f^n - \alpha \cdot \Delta t \cdot (f^{n+1} - b) \qquad (2.4)$$

so that the final expression for the new value of f is:

$$f^{n+1} = \frac{f^n + \alpha \cdot \Delta t \cdot b}{1 + \alpha \cdot \Delta t} \qquad (2.5)$$

where f^{n+1} is the variable to be nudged at the new time step and at the old time step f^n, respectively. Δt is the model time step, b is the respective background value and α is the nudging coefficient. The three dimensional form of the nudging coefficient controls the structure of nudging. If nesting conditions are chosen, that means background values influence the simulations only at the lateral boundaries. In this case α is set to zero in the interior of the domain and increases towards the boundary inbetween a predefined lateral boundary zones. If the nudged variable should influence the simulation also inside of the domain, α is chosen to be horizontally homogeneous and the vertical structure is set by:

$$\alpha = 2 \cdot \alpha_{const} \cdot \Delta t \cdot \left[1 + \frac{atan(k - k^*)}{\pi} \right] \qquad (2.6)$$

where α_{const} represents the reciprocal value of a typical time scale, k is the index of the vertical model level and k^* is a vertical reference level where the *tangent*-function has its inflection point. The use of a *tangent*-function as vertical definition of the nudging coefficient has the advantage that the influence of the background values decrease towards the lower levels of the model, so that locally induced effects are not influenced by background conditions. As the three dimensional structure of α determines where the nudging takes place, the value of α specifies how strong the nudging equation pushes the model value towards the prescribed background value. The pressure at the model top boundary is set equal to the prescribed background pressure. For other variables the model top layer is open for inflow and outflow to enable the model to simulate convergent and divergent meteorological situations as they appear in reality.

2.3 Parameterizations of Chemically Reactive Trace Species

The RADM II mechanism (*Stockwell et al.*, 1990), a dry deposition and an emission model have been included 'on-line' in the original GESIMA model and will be described in this section.

2.3.1 The Gas Phase Chemistry Mechanism

The RADM II species are listed in appendix A and the complete chemical reaction scheme is presented in appendix B. The mechanism allows transformation of 63 species in 161 reactions.

Reaction Rates

The 140 non-photolytic reaction rates are adjusted for temperature and pressure. Clear sky photolysis rates for the 21 photolytic reactions are precalculated for hourly angles between sunrise and sunset by a radiative transfer model based on the delta-Eddington technique (*Joseph et al.*, 1976; *Madronich*, 1987). This model assumes seasonally averaged ozone and aerosol distributions. It divides the region from the surface of the earth to the top of the atmosphere into more than 50 layers. The actinic flux is calculated for 130 spectral intervals over the atmospheric actinic region from 200 to 730 nm. The size of the individual spectral interval vary from 1 to 10 nm depending on the spectral absorption bands of the reactive species. The actinic fluxes are calculated and then integrated with the absorption cross section and the photo dissociation quantum yield to produce a table of clear sky photolysis rates that are used to drive the photolytical reactions. The following expression is used to calculate the photolysis reactions (j_i):

$$j_i = \int_\lambda \sigma_i(\lambda)\phi_i(\lambda) \int_\varphi \int_\theta I(\lambda, \varphi, \theta) \, sin \, \theta \, d\theta \, d\varphi \, d\lambda \tag{2.7}$$

where $\sigma_i(\lambda)$ and $\phi_i(\lambda)$ are the temperature- and/or pressure- dependent molecular absorption cross section and quantum yield for each photolysis reaction and $I(\lambda, \varphi, \theta)$ is the radiance at a particular atmospheric location. The integrals are over all wavelengths λ directions φ, θ. Every model time step during the simulation the stored data sets are linearly interpolated in time to update the photolysis rates.

Inorganic Species

The inorganic species are represented by 14 moderately reacting species, four highly reactive intermediates, and three abundant stable species (oxygen, nitrogen and water). A standard reaction scheme for the inorganic tropospheric chemistry is incorporated in the RADM II mechanism. Most of the inorganic reactions and rate constants are derived from *DeMore et al.* (1988). The chemistry of odd oxygen, odd hydrogen, odd nitrogen and sulfur species is relatively well known. The nighttime chemistry involving NO_3 and N_2O_5 is more complex and leads to heterogeneous formation of nitric acid.

Organic Species

The atmospheric organic chemistry is represented by 26 moderate reacting species and 16 highly reactive peroxy radicals. RADM II aggregates the hundreds of volatile organic components (VOC) into 26 classes of reactive organic species, where some are treated explicitly and others are represented as lumped species. A detailed description of organic compounds can be found in *Atkinson* (1990). A reactivity lumped molecular approach is used which combines the molecular concentrations of a gas mixture into surrogate species of similar reactivity and molecular weight. Organic mixtures with different reactivity towards the OH radical are grouped into different surrogates and multiplied with a reactivity factor.

The RADM II reactivity weighting is based on the assumption that the effect of VOC emissions on the model results is approximately proportional to the amount of the compound that reacts on a daily basis. Under this assumption an emitted compound can be represented by a model species which reacts at a different rate provided that a weighting factor is applied to the compound emissions. The factor is the ratio of the fraction, F, of the model species which reacts:

$$F = -\frac{1 - exp(-k_{OHEmit} \times \int [OH]dt)}{1 - exp(-k_{OHModel} \times \int [OH]dt)} \tag{2.8}$$

k_{OHEmit} is the rate constant for the reaction of OH with the individual compound, $k_{OHModel}$ is the rate constant for the reaction of OH with the RADM II model species, and the term $\int [OH]dt$ is the daily average integrated OH radical concentration. The reactivity weighting factor becomes unity if both, the emitted species and the model species are highly reactive.

Alkanes [methane, ethane and three higher lumped groups]
Under atmospheric conditions, the only important loss process for the alkanes is their reaction with OH radicals. However, alkanes react slowly with OH and thus can be transported over large distances. Methane and ethane are treated explicitly in the mechanism. All higher alkanes are aggregated according to their OH reaction rate constants into three additional model species.

Alkenes [ethene, terminal and internal alkenes, isoprene]
Alkenes are most reactive with OH and account to a large degree for the NO - NO_2 conversion. Atmospheric loss processes take place by reactions with OH, NO_3 radicals and O_3. Alkenes are important constituents of the polluted and the rural troposphere, because they represent a wide range of species which are emitted anthropogenically and biogenically. In the RADM II

mechanism alkenes are represented by two lumped species and explicitly by isoprene (because of its natural origin and high reactivity) and ethene (because of it's low reactivity). The two lumped groups represent internal double bound and terminal double bound alkenes.

Aromatics [toluene, xylene and cresol]

Aromatic chemistry is very important under polluted urban conditions. The complex aromatic chemistry is represented relatively simply by three classes. Cresol is treated explicitly and two aromatic groups are lumped. One group consists of less reactive compounds like toluene, benzene and other compounds with OH rate constants similar to the rate constant of the OH - toluene reaction. The other lumped group describes highly reactive aromatic species like xylene and mesitylene.

Carbonyls [aldehydes, ketones and dicarbonyls]

Aldehydes (formaldehyde and acetaldehyde) and ketones are formed as intermediate products during the atmospheric degradation reactions of a large number of organic compounds. In the atmosphere these carbonyls can photolyse and react with OH, NO_3 and HO_2 radicals. The mechanism treats formaldehyde explicitly and lumps the higher aldehydes into one class that reacts as acetaldehyde. Another class is formed by ketones. Dicarbonyls are represented by three additional groups.

Organic Nitrogen

The organic nitrates are represented by three groups: Peroxyacetylnitrate (PAN) and higher PAN's, $CHOCH{=}CH\ CO_3\ NO_2$ and other organic nitrates.

Organic Peroxides

Peroxy radical - peroxy radical reactions play an important role in atmospheric chemistry. Under rural and clean conditions, these highly reactive intermediates strongly affect photochemical transformations. A large number of peroxy radical - peroxy radical reactions and 16 classes of peroxy radical intermediates are included in the mechanism.

Organic Acids [formic and acetic acid]

The organic acids of interest in the polluted urban atmosphere are formic and acetic acids. These species are treated explicitly in the mechanism. They are formed as water soluble oxidation products from various organic components.

The Numerical Solution Technique

The quasi steady state approximation (QSSA) is used to solve the nonlinear set of 161 chemical kinetic differential equations. This simplification is necessary because a simple numerical solution technique would require a very small time step to maintain stability due to the stiffness of the equation system. The principle of the QSSA method is that very reactive species rapidly transform to their equilibrium values. For those species a steady state is assumed:

$$\frac{\partial C_j}{\partial t_{chem}} = 0 \qquad\qquad (2.9)$$

The remaining chemical rate equations are integrated with the equation:

$$\frac{\partial C_j}{\partial t_{chem}} = P_{chem}(C_i) - [\frac{C_j}{\tau_c(C_i)}]$$ (2.10)

where C_j is the concentration of species j and $P_{chem}(C_i)$ is the production rate and $\tau_c(C_i)$ is the characteristic loss time scale, both of which are explicitly dependent on other species concentrations C_i. If P_{chem} and τ_c are constant during a time step Δt_{chem} the solution of Eq. (2.10) is:

$$C^{t+\Delta t_{chem}} = P_{chem}\tau_c + (C^t - P_{chem}\tau_c)exp(-\Delta t_c/\tau_c)$$ (2.11)

where C^t and $C^{t+\Delta t_{chem}}$ are the concentration at time t and $t + \Delta t_{chem}$. The chemical time step in GESIMA varies between $0.01 sec < \Delta t_{chem} < \Delta t_{met}$ with Δt_{met} as meteorological time step. The complete solution technique is described in *Hesstvedt et al.* (1978).

2.3.2   Dry Deposition

Dry deposition, the transport of species from the atmosphere onto surfaces, is the ultimate path by which trace gas species are removed from the atmosphere. In GESIMA the parameterization of the dry deposition follows the surface resistance concept of *Wesely* (1989). The deposition velocity

$$v_d = (r_a + r_b + r_s)^{-1}$$ (2.12)

is inversely proportional to the sum of three resistance terms: an aerodynamic resistance, r_a, a quasi-laminar sub-layer resistance, r_b, and a surface resistance, r_s. The aerodynamic resistance is independent of the trace species properties. It is proportional to the turbulent mixing and is approximated as

$$r_a = ln(z/z_0) - \Psi_h/ku*$$ (2.13)

where k is the Karman constant (k=0.35), $u*$ the friction velocity (root mean covariance between the horizontal and the vertical velocity components), z_0 the roughness length (the effective level at which the horizontal wind speed approaches zero) and Ψ_h the Businger function (*Businger*, 1973) (an integral diabatic influence function related to the local atmospheric stability).

The quasi-laminar resistance, r_b, is defined as:

$$r_b = 2/ku * [\kappa/D_g]^{2/3}$$ (2.14)

where κ is the thermal diffusivity of air and D_g is the molecular diffusivity for a trace gas in air.

The surface resistance is dependent on the season of the year, the landuse classification and the trace species. It is parameterized as followed:

$$r_s = [1/(r_{su} + r_m) + 1/r_{lu} + 1/(r_{dc} + r_{cl}) + 1/(r_{ac} + r_{gs})]^{-1} \tag{2.15}$$

The surface resistance is dependent on the resistances for the leaf stomata (r_{su}), the leaf mesophyll (r_m), leaf citicles (r_{lu}), buoyant convection (r_{dc}), leaves in the lower canopy (r_{cl}), canopy height depending resistance (r_{ac}) and a soil resistance (r_{gs}). The detailed parameterizations of the single surface resistances are very complex. They are described in detail by *Wesely* (1989). Some of the resistances included in Eq. (2.15) needs to be calculated for all the individual gases separately because the chemical species differ in their molecular diffusivity, their Henry's Law constant (describing water solubility) and their reactivity. The species for which a deposition velocity is calculated as described in this section are listed in the Table 2.2. An exclusion is made for sulfuric acid. The particulate deposition velocity for sulfuric acid is assumed to be only dependent on turbulent values.

Table 2.2: Dry deposited species

Gaseous species	Symbol	Gaseous species	Symbol
Sulfur dioxide	SO_2	Acetaldehyde	R-CHO
Nitrigen dioxide	NO_2	Formaldehyde	H_2CO
Nitrigen oxide	NO	Methyl hydrogen peroxyde	CH_3O_2H
Nitrous acid	HNO_2	organic hydrogen peroxydes	$R-O_2H$
Ozone	O_3	Peroxyacetic acid	$CH_3CO\ OOH$
Nitric acid	HNO_3	Formic acid	HC OOH
Peroxyacetylnitrate	$CH_3CO_3NO_2$	Acetic acid	CH_3COOH
Hydrogen peroxide	H_2O_2	Ammonia	NH_3

2.3.3 Chemical Information at the Lateral Boundaries

All prognostic chemical species are transported across the lateral model boundaries. The explicit multi step advection scheme (*Smolarkiewicz*, 1983) where a first order upstream step is followed by two anti diffusive corrective steps is used. The upstream step does not cause reflections at the outflow boundaries, since only upstream information is used. The boundary conditions differ according to whether the flow is directed into or out of the domain. Under inflow conditions all transported chemical species are specified by interpolation of coarse grid model results along the nested grid boundaries. The outflow boundary conditions are specified by constant advection of the concentrations over the last two gridcell interfaces in order to eliminate reflections of outgoing waves. After *Pleim et al.* (1991) concentrations at the boundaries are specified as:

$$C_i = C_{i-1} - \frac{u_{i-1}}{u_i}(C_{i-2} - C_{i-1}) \tag{2.16}$$

where C_i is the concentration in grid cell i and the wind speed u is taken at the interface between cell $i-1$ and i. This method minimizes flux divergence at the boundary while allowing local concentrations to evolve its response to changing conditions.

2.3.4 Emission Rates

Biogenic Emission Rates

Many organic compounds are emitted by vegetation. Biogenic emissions are primarily alkenes and cycloalkenes. In GESIMA, the emission of isoprene and monoterpenes from forests are parameterized after *Guenther et al.* (1991, 1993). The temperature dependent monoterpene emissions are described by:

$$E = E_s[exp(\beta(T - T_s))] \tag{2.17}$$

where E is the monoterpene emission rate at temperature T and E_s the emission rate at a standard temperature, T_s. β is an empirical coefficient, (β=0.09). Taking into account the GESIMA landuse classification, monoterpens are emitted by coniferous forests and 50 % by mixed forests. In adaption to the RADM II mechanism, the parameterized monoterpene emissions are subdivided into terminal alkenes and internal alkenes. In contrast to monoterpene emissions, isoprene emissions are also dependent on the photosynthetic active radiation (PAR):

$$E_I = S_I LT \tag{2.18}$$

where E_I stands for the emission of isoprene, S_I is the isoprene emission rate at T_s and a standard radiation, L is the light correction factor, and T the temperature correction factor. The light depending correction factor L is defined after *Guenther et al.* (1991) as:

$$L = (x - \sqrt{x^2 - 4fIL_1})/2L_1 \tag{2.19}$$

where $x = fI + L_1 + L_2$, $f = 0.385$, fraction of light absorbed by chloroplasts, I is the irradiance, and $L_1 = 105.6$ and $L_2 = 6.12$ are empirical coefficients. The temperature dependence is described by:

$$T = [exp(T_1(T_L - T_S)/RT_LT_S)]/[1 + exp(T_2(T_L - T_3)/RT_LT_S)] \tag{2.20}$$

where T_L is the leaf temperature (e.g. surface temperature), and $T_S = 301\ K$, $T_1 = 95100\ J\ mol^{-1}$, $T_2 = 231000\ J\ mol^{-1}$, and $T_3 = 311.83\ K$ are empirical constants. R is the molar gas constant ($R = 8.314\ J\ mol^{-1}K^{-1}$). The chemical degradation of isoprene is explicitly included in the RADM II mechanism. Isoprene is emitted by deciduous forests and following the model description 50 % by mixed forests.

Anthropogenic Emission Inventories

Emission inventories are generated by emission models. These models take into account various emission factors to create high resolving data sets in space and time for hundreds of chemical species. Emission factors are an estimate of emissions of a species from a source based on source specific emission measurements as a function of activity level with regard to each source. Emission models uses statistical data that are connected to atmospheric anthropogenic emissions, for gaseous inorganic and organic species and aerosols. For example, the formulation for emission factors of traffic emissions depend on rather complex emission estimations (*UBA*, 1995; *Hassel et al.*, 1994, 1995) where the main factors are the specific distribution of motor vehicle age and type, the mean trip profiles, cold start exhaust, running losses as well as topographic and meteorological parameters. Additionally, laboratory vehicle testing is performed, which determines the exhaust emission of a vehicle (*Hassel et al.*, 1998). Traffic emission factors for NO_x and anthropogenic non-methane volatic organic compounds NMVOCs are rather well known compared to the NMVOC emissions produced by the dissolvent industry. The classical usage of organic dissolvents in the chemical industry is only a minor source to atmospheric NMVOC emissions because these industrial emissions are produced in self-contained technical facilities and only small amounts of emissions are released into the environment. The primary emission source for NMVOC are smaller firms and private households. The following disolvents are the major constituents to anthropogenic NMVOC emissions: paints, glues, detergents and solvents. The disolvent emission factors are estimated in consideration of many emission factors, for example industrial emission declarations, trade data sets, information of density and classification of population, settlement and employment, etc. Because of the influence of so many, partly highly unprecise, data sets the estimation of the emission errors is rather difficult. Error estimations (*Kühlwein et al.*, 1999) for total motor vehicle emissions shows errors between 15 - 35% and 30 - 50% for dissolvents. Additional to these errors are uncertainties in the spatial and temporal discretization, increasing the error dramatically, especially for the dissolvent emissions. An emission model calculates temporal and spatial gridded emission inventories for a wide range of chemical species. These emission inventories are used as model input as described below.

Anthropogenic Emission Rates

Anthropogenic emission inventories are extremely important external model information influencing substantially the model results when applying the model in industrialized areas. GESIMA receives the information of hourly emission rates of SO_2, sulfate, NO, NO_2, NH_3, CO and 14 classes of VOC's, divided into point and area emissions. The emission inventory is taken from data compilation by the IER (Institut für Energiewirtschaft und Rationelle Energieanwendung) of the University Stuttgart. All area sources are located in the lowest model layer. Point emissions take place in the model layer which corresponds to the chimney height and a plume rise formulation (*Briggs*, 1975). The emission information from the emission inventory are further aggregated into a smaller set of VOC classes which directly correspond to those in the chemistry mechanism following the aggregation method of *Middleton et al.* (1990).

2.4   Description of the REMO Model

The Regional Climate Modell REMO (*Jacob and Podzun*, 1997) is an 'on-line' hydrostatic three-dimensional atmosphere-chemistry model (*Langmann*, 2000) on the regional scale. The dynamical part is based on the regional weather forecast model system EM (Europa Modell)/ DM (Deutschland Modell) of the German Weather Service (*Majewski*, 1991). The physical parameterization scheme of the climate model ECHAM4 (*Roeckner et al.*, 1996) is included alternatively to enable longterm climate simulations. For the calculation of chemical transformations the RADM II gas-phase mechanism considering 161 reactions and aqueous chemistry processes according to *Walcek and Taylor* (1986) are included. For the transport of the chemical species the following processes are considered: Horizontal and vertical advection according to *Smolarkiewicz* (1984) or alternatively *Bott* (1989), vertical diffusion, dry (*Wesely*, 1989) and wet (*Walcek and Taylor*, 1986) deposition, convective up and downdraft (*Tiedtke*, 1989). Clear sky photolysis rates are precalculated by the climatological radiative transfer model after *Madronich* (1987), and in presence of clouds the photolysis rates are modified in REMO according to *Chang et al.* (1987). Biogenic emissions are parameterized after *Guenther et al.* (1993) and anthropogenic emissions are provided externally.

3 Field Experiment and Model Configuration

3.1 Field Experiment FLUMOB

The field experiment FLUMOB (Flugzeug und Boden Messungen von Ozon und Vorläufer-stoffen zur Abschätzung der Wirksamkeit von emissionsmindernden Maßnahmen im Großraum Berlin-Brandenburg - *Aircraft measurements of ozone and precursors for the estimation of emission reduction measures in Berlin-Brandenburg, Stark et al.* (1995)) took place in Berlin-Brandenburg from July 23 until July 27 in 1994 to measure the concentrations of ozone and its precursors during a distinct ozone episode. The field experiment covered an area of about 200×200 km^2 around the city of Berlin. The area of Berlin-Brandenburg was chosen for this field experiment because of its flat topography. Furthermore, the city of Berlin is characterized by high traffic and industrial emissions and a rural environment with low industrial emissions but frequently used highways. These conditions seemed to be optimal to investigate the production and transport of ozone and its precursors in polluted air masses. In addition to the routine measurements of the German Weather Service, ground based measurements, aircraft measurements and some radio-sonde soundings have been carried out to measure meteorological parameters and concentrations of some chemical species, mainly ozone and NO$_x$.

3.2 REMO Model Configuration
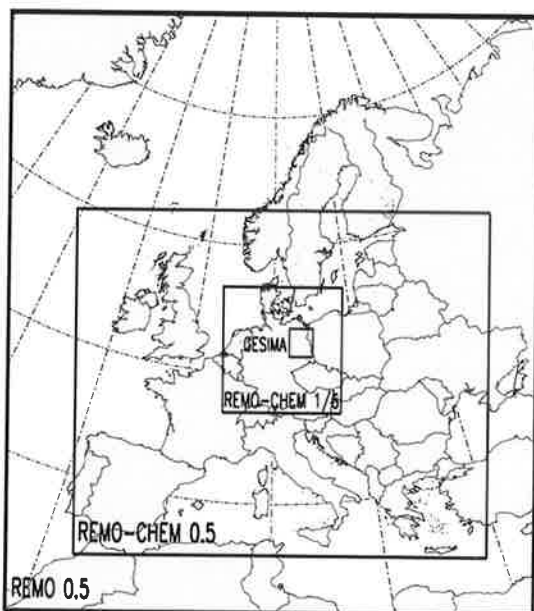
Figure 3.1: The boxes indicate the model domains of the REMO 0.5° meteorological simulation, the REMO 0.5° and REMO 1/6° chemistry simulation and the GESIMA simulation domain.

To address the scientific questions central to the FLUMOB measurement campaign the simulation domains of the models are chosen to focus down from the wider European domain to a narrower area of Germany and then to the even narrower area of Berlin-Brandenburg. The regional atmosphere-chemistry model REMO is applied with a horizontal grid point distance of 0.5° ($\approx$ 50 km) over Europe and with a 1/6° resolution ($\approx$ 18 km) covering Germany. The domains where tropospheric chemistry is calculated are smaller to save computer time and memory and marked by REMO-CHEM in Fig. 3.1. For the horizontal grid point representation a spherical rotated grid is used. REMO has 20 vertical layers with a terrain following hybrid pressure-sigma coordinate system extending up to 10 hPa height. REMO is applied with the physical parameterizations of the German Weather Service, because the chemistry is adapted to that

physical scheme. Analysis data from the German Weather Service are used for initialization and as lateral boundary information with a time resolution of 6 hours for both REMO 0.5° and REMO 1/6° model resolutions. The chemical concentrations of all prognostic species are set to constant values at the lateral boundaries of the REMO 0.5° simulation because no global chemistry simulation was available for the FLUMOB episode. These concentrations are estimates from measurements and climatological model simulations (references in *Chang et al.* (1987)). The results of the coarse REMO simulation are used to initialize the nested REMO 1/6° simulation and to provide concentrations at the lateral model boundaries. External data sets, like emissions, photolysis rates, and lateral boundary concentrations are prepared for every hour and a linear time interpolation adapts all external data sets to the model time step. The models are run in the forecast mode: Starting at 0 UTC every day a 30 hour forecast is calculated. The first six hours of every forecast are neglected to account for a spin up time. By starting the model again every day with analysis data, the model atmosphere stays close to the real weather condition. The chemistry is calculated continuously. The model is started on July 20, 1994 and is integrated until July 30 with a meteorological time step of five minutes for the REMO 0.5° simulation and two minutes for the REMO 1/6° simulation. The FLUMOB REMO simulation is described in *Langmann* (2000).

3.3 GESIMA Model Configuration

The GESIMA model domain covers the 200×200 km^2 area of the FLUMOB field experiment. Berlin is situated in the center of the model domain. In the southern direction the domain extends to 51.5°N. Cottbus and the industrial area of Bitterfeld are just covered by the model. In the eastern direction the model domain crosses the Polish border, and the Polish city of Stettin is situated in the north east corner of the GESIMA domain (53.4°N, 14.8°E). In the western direction the model domain ends at 11.9°E shortly before Magdeburg. A horizontal grid-point distance of 4 km is chosen on an orthogonal cartesian grid. In the vertical the model layers are represented by 25 terrain following z-levels. The lowest level reaches up to 20 m height above the earth's surface and the upper most level extends to an altitude of 11 km. The landuse
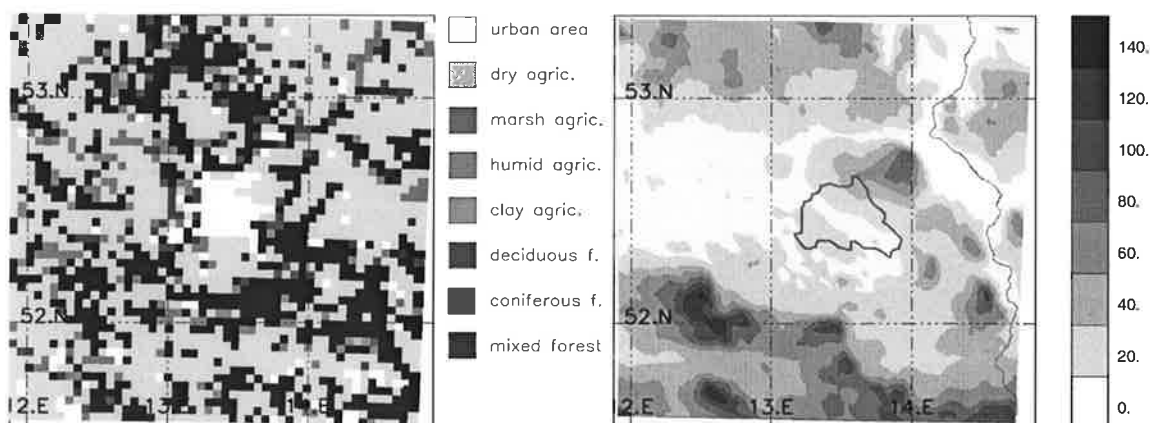
Figure 3.2: GESIMA surface characteristics: Landuse classifications (left panel) and topographic heights (right panel) in [m].
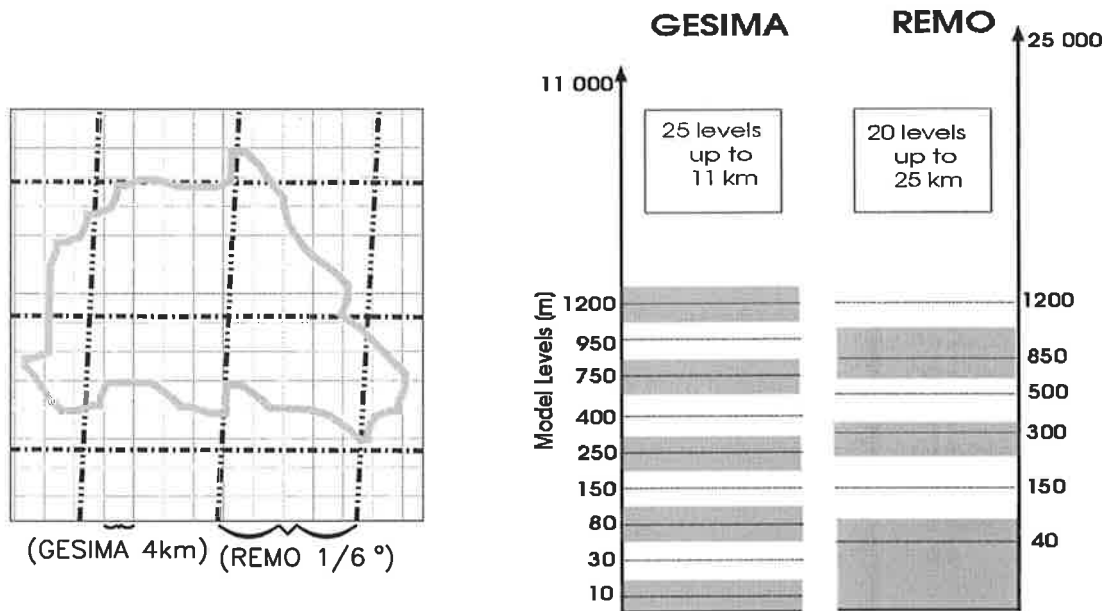
Figure 3.3: Geometry of the horizontal grid boxes (left panel) for the GESIMA (solid lines) and the REMO 1/6° (dashed line) simulation (shown exemplarily for the Berlin area). Vertical GESIMA and REMO model levels in z-coordinates (right panel). The height levels are marked at the center of the grid boxes. REMO levels are shown for standard atmosphere conditions.

classification and the topography of the GESIMA domain are shown in Figure 3.2. The area of Brandenburg is rather flat. The topography varies from only a few meters to 140 m height from the Odra valley to the Fläming hills. The landuse classification (Fig. 3.2, left panel) indicates the rural character of the area around Berlin. The largest fraction is covered by dry agricultural soils, followed by forest, which consists mainly of coniferous forest.

The GESIMA simulation is nested into a REMO model run. The following variables as determined by the REMO 1/6° simulation are interpolated to the grid of the GESIMA model: horizontal wind velocities, potential temperature, specific humidity, pressure, and concentrations of the 39 prognostic chemical species. The different horizontal representations of grid boxes by the two models is indicated in Fig. 3.3, (left panel). The horizontal resolution of GESIMA is about four times higher compared to the REMO 1/6° simulation. The variables are bilinear interpolated from the spherical rotated REMO grid to the cartesian GESIMA grid. In the vertical the variables are interpolated linearly from the hybrid pressure system of the REMO model to the z-coordinate system of GESIMA. To compare the different vertical resolutions and coordinate systems of the models REMO and GESIMA levels are shown together in Fig. 3.3, (right panel) by assuming standard atmosphere conditions (i.e. a surface pressure of 1013 hPa) for the REMO levels. In the lower troposphere GESIMA has a vertical resolution about two times higher, but with increasing height the depth of the model layers converge.

The three-dimensional distributions of all nested meteorological and chemical variables as determined by the REMO model are used for the initialization of the GESIMA simulation. Additionally, the atmospheric surface temperature and humidity of the REMO simulation are used for the initialization of the GESIMA surface and the four soil model layers. Here the variables

are not interpolated but set to the corresponding REMO values according to similar landuse classification.

3.3.1 Nesting Procedures for the GESIMA Model

For the realization of the nesting of meteorological and chemical variables different approaches are used. Common to all external time dependent data sets is that they are prepared with a time resolution of 1 h and adapted to the model time-step by linear interpolation.

- The nested chemical trace gas concentrations are transported by advection across the models lateral and top boundaries as described in section 2.3.3. Thus only trace gas concentrations close to an inflow boundary grid point are influenced by the nesting.

- The background (interpolated field of the REMO simulation) pressure is prescribed only at the top boundary level.

- The potential temperature and specific humidity background fields are nested to the 10 lateral grid points at all four lateral boundaries and at the 10 top boundary grid points. The nesting coefficient decreases linearly to zero in between this 10 grid point boundary zone and thus the background fields do not influence the GESIMA model parameters in the interior domain outside of the boundary zone.

- The background horizontal wind velocity fields are nested horizontally homogeneously to the GESIMA simulation but the nesting coefficient varies in the vertical direction. Fig. 3.4 shows the vertical shape of that nesting coefficient. The turning point of the nesting coefficient is placed at level 10, at a height of about 1500 m. Above that level the nesting of the GESIMA wind field towards the background field is strong and below that level the nesting is weaker but still influences the GESIMA results.

This nesting approach is one of many possible formulations. In general, the appropriate nesting technique depends on the nested variable, the topography of the model domain and the meteorological situation. In the case discussed here the meteorological situation and the topography of the model domain are very homogeneous so that no specific nesting methods need applied. The vertical dependent nesting method for the horizontal wind components is chosen because under homogeneous conditions the wind field is determined by the large scale weather con-

Figure 3.4: Vertical structure of the nesting coefficient of the horizontal wind components.

ditions. In the lower atmosphere the reduced nesting coefficient allows local influences. To exclude instabilities this nesting configuration was additionally tested under a dynamically complex situation. The GESIMA model was applied at the steep Norwegian coast. No instabilities at the lateral boundaries or in the interior of the domain occurred either in the Norwegian coast test

case or in the Berlin-Brandenburg simulation. Therefore the nesting method is deemed suitable for use in the following simulation.

The model is integrated for seven days starting on July 22, 1994. The meteorological time-step is set to 20 s. The computing time on a CRAY C90 is about 1CPU hour for 1 h model simulation.

3.3.2 Anthropogenic Emissions for the FLUMOB Episode

The GESIMA emission inventory for the FLUMOB episode is prepared by the IER (Institut für Energiewirtschaft und Rationelle Energieanwendung) in Stuttgart (*Wickert*, 1999). Each day was individually calculated. Examples for two classes of anthropogenic emissions are discussed in Figure 3.5 and 3.6. NO_x emissions, the sum of NO and NO_2, are shown in Figure. 3.5. The left panel presents the horizontal distribution of the NO_x emission exemplarily for July 25
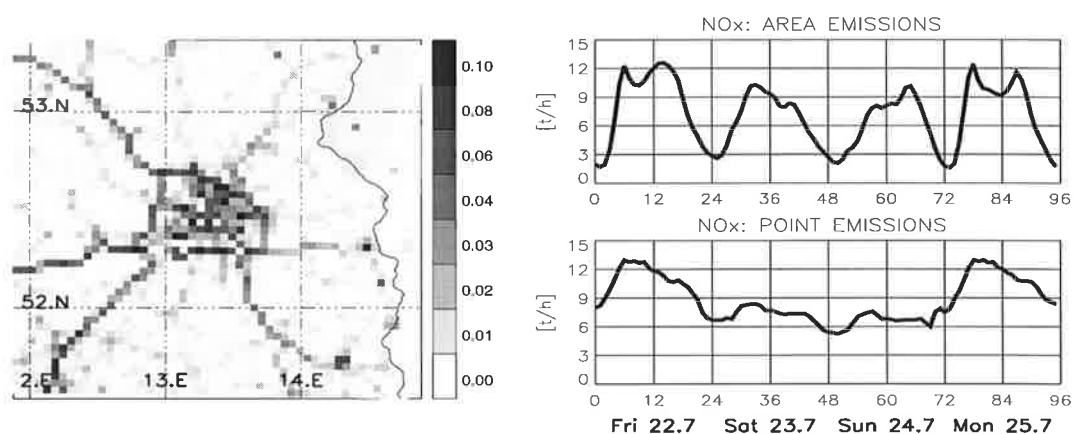
Figure 3.5: NO_x emission on July 25, 1994 at 6 UTC (left panel). Time series of NO_x emission for the sum of all area emission sources (right, upper panel) and point sources (right, lower panel) released into the domain between July 22 and 25. The emissions are in units of [t/h].
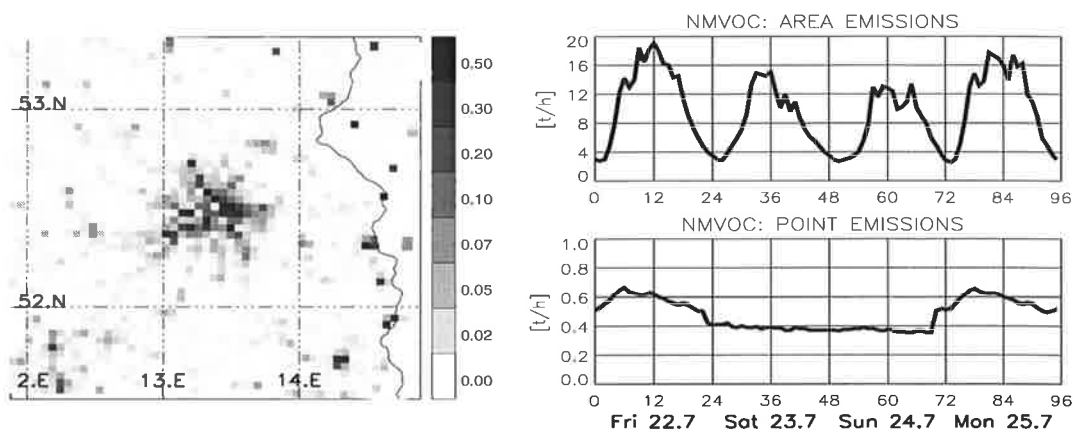
Figure 3.6: NMVOC emission on July 25 at 6 UTC (left panel). Time series of NMVOC emission for the sum of all area emission sources (right, upper panel) and point sources (right, lower panel) released into the domain between July 22 and 25. The emissions are in units of [t/h].

at 6 UTC. The major NO_x sources are traffic and industrial emissions. They are emitted predominantly in the city of Berlin and the frequently used highways. Even some smaller streets inbetween the highways can be detected. Behind the Polish border the emissions are distributed more homogeneously. This is the result of less detailed emission factor data sets for Poland. The curves in Figure 3.5 show the time evolution of the total area (upper panel) and point (lower panel) emissions for 4 days (Friday to Monday) of the FLUMOB episode. Different time evolution between a weekday and weekend emission are visible. The total amount of point and area emissions for NO_x is in about the same range. During weekdays the NO_x emissions show a daily double peak structure, indicating the morning and evening rush hours. All anthropogenic non-methane volatile organic compounds (NMVOC) are summed up and presented in Figure 3.6. The dominant NMVOC source is Berlin, followed by some other cities in Brandenburg, for example Cottbus (51.2°N, 14.19°E) and Frankfurt/Oder (52.2°N, 14.33°E). The total area NMVOC emissions (upper panel, Fig. 3.6) show much higher amounts compared to the point emissions (lower panel). The area NMVOC emissions show concentrations comparable to the NO_x emissions of about 10 t/h whereas the point NMVOC emission rates lie at about 0.5 t/h. During weekdays the NMVOC emissions are higher than in the weekend.

4 Validation of Meteorological Parameters

In this chapter a comparison between the real weather condition, the observation data sets and the simulations as calculated by the REMO and the GESIMA model will be carried out. First, the weather condition which occurred during the FLUMOB measurement campaign is introduced. Then, this large scale weather condition is compared with the REMO simulation. A validation and a statistical analysis between the observed and simulated time series of meteorological parameters is calculated with the results of the GESIMA simulation. A comparison between the REMO and the GESIMA simulation will not be discussed in detail because the blocking weather condition and the flat terrain of Berlin - Brandenburg did not produce locally pronounced mesoscale weather phenomena. Therefore, differences occurring between the weather conditions as calculated by the REMO and the GESIMA model are rather small and must be attributed mainly to the different resolutions of the models and less to the models dynamical and physical formulations. Thus, in this specific case a more detailed study is not required. The validation of meteorological parameters as carried out in this chapter is performed mainly to enable the evaluation of the chemical simulation.

4.1 Weather Condition during FLUMOB

The weather condition during the FLUMOB measurement campaign between July 23 and 28, 1994 were characterized by a quasi stationary high pressure system over central Europe and fast moving low pressure systems over the Northeast Atlantic (*Geb and Naujokat*, 1994). The European weather conditions for July 23, 25 and 27 at 00 UTC are presented in Figure 4.1 showing the mean sea-level pressure and the geopotential height field at 500 hPa as analysed by the 'Europa Model' of the German Weather Service (*Majewski*, 1991) in 0.5° resolution. The

Figure 4.1: Analysis data in 0.5° resolution from the Europa Model: Mean sea-level pressure (dashed lines) and the 500 hPa geopotential height field (solid lines) on July 23, 25 and 27, 1994 at 00 UTC. Contour lines every 2.5 hPa and 4 gpm, respectively.
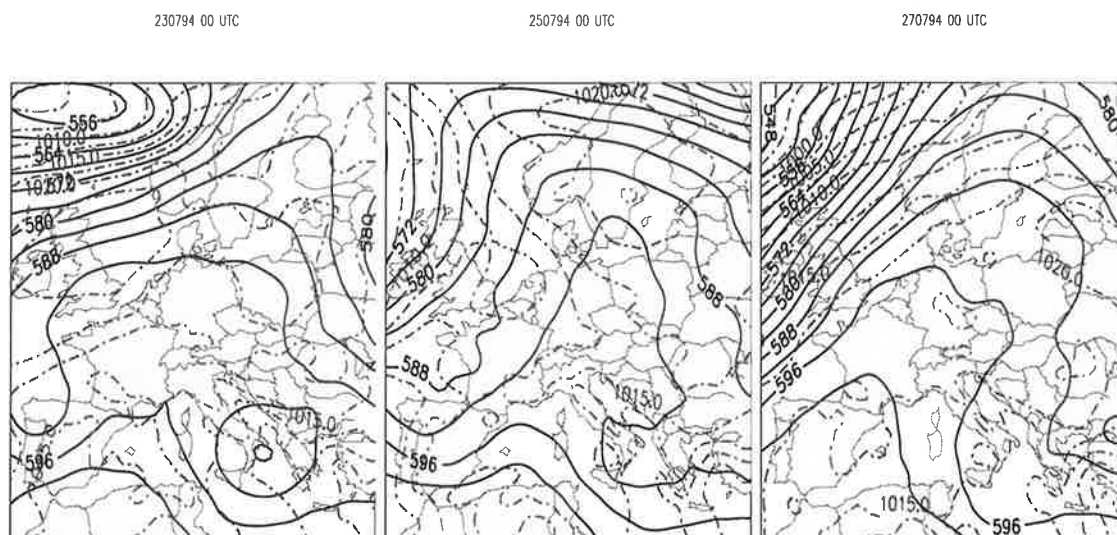
quasi stationary trough over Central Europe of the 500 hPa geopotential height field displays the blocking situation. During the first three days of this episode (July 23 to 25) the surface high pressure system was centered over the Baltic sea and Scandinavia; Central Europe was influenced by easterly winds connected with a transport of continental dry air masses. A weak low pressure system crossed Germany on July 26. Behind that flat low pressure trough a new high pressure system developed over Germany which lead to an influence by northern winds with humid air masses during the 26th and the 27th. The maximum temperatures surpassed 30°C in Germany for all days reaching the highest temperatures, above 34°C, in Berlin, Germany, on July 25.

4.2   Meteorological REMO Simulation

The meteorological simulation of the REMO 1/6° model resembles the observations (Fig. 4.1), showing realistically modelled mean sea-level pressure fields and horizontal wind components in 10 m height over Germany (Fig. 4.2). The minor deviations of the simulated mean sea-level pressure fields over the Alps can be ascribed to the different horizontal resolutions of the compared model and the analysis data sets and therefore to differences in the representation of topography. The good agreement between the observed and simulated meteorological parameters was expected because the REMO 0.5°, as well as the REMO 1/6°, simulations are initialized and driven directly by the analysis data sets as described in chapter 3.2.
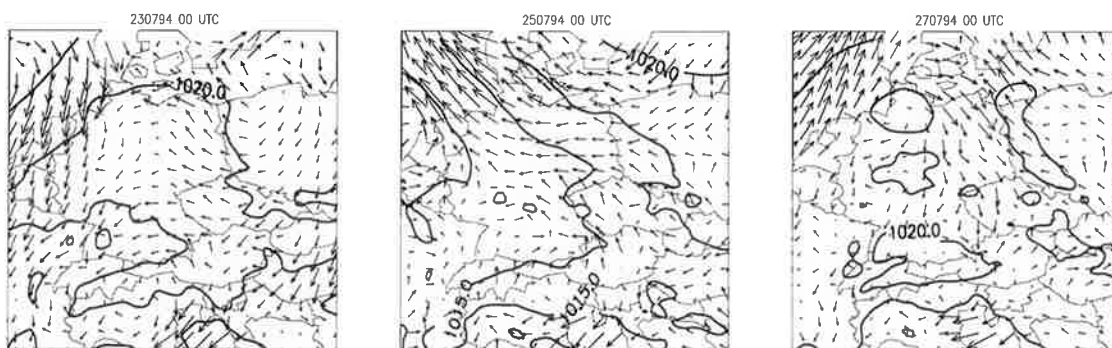
Figure 4.2: Mean sea-level pressure (solid lines) and horizontal wind components in 10 m height on July 23, 25 and 27 at 00 UTC as simulated by the REMO 1/6° model. Contour lines every 2.5 hPa.

A direct comparison of point measurements with the corresponding grid boxes of the REMO 1/6° simulation is presented in Fig. 4.3 for the wind velocity and direction at different levels for the time period of the whole FLUMOB episode. The wind profiler measurements are taken at the observation station Lindenberg. The variability of the wind velocity is slightly underpredicted by the REMO model but the general correspondence between the measured and simulated wind components is good. The simulation of the wind directions resembles the observed condition even better: This is the turning of the wind from south-easterly to northern directions in the two lower levels of 240 m and 1300 m, and the wind turning from northern to southern directions above the planetary boundary layer at 3250 m height.
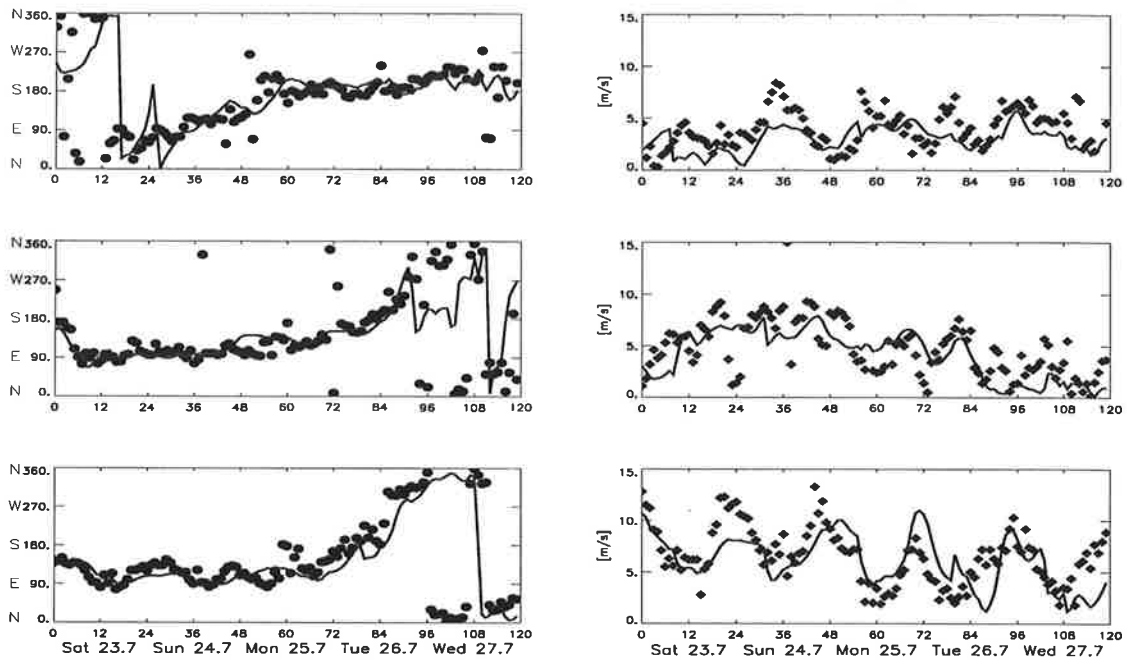
Figure 4.3: Wind direction [°] (left panel) and velocity [m/s] (right panel) in three height niveaus (240 m (lower panel), 1300 m (middle panel) and 3250 m (upper panel)) are compared between the REMO simulation (solid line) and measured wind profiler data sets (points) at station Lindenberg.

As an example of the temperature evolution in Berlin-Brandenburg during the time of the FLU-MOB period observed 2 m temperatures are compared with modelled values (Fig. 4.4). The time series comparison shows an average over all 17 stations located in Berlin-Brandenburg and the average over the corresponding model grid boxes. The modelled temperatures are diagnostically interpolated to the 2 m level. The observed daily maximum temperatures increased steadily during the first three days and reached about 33°C on the 25th. After that day the maximum temperatures decreased again. The daily minimum temperatures increased from day to day during the entire episode. These features, as well as the evolution of the daily temperature cycle, is well reproduced by the model. But the model tends to overestimate the daily minimum temperatures occurring during the night and in the early morning hours. The 2 m level is not explicitly resolved by the REMO model and therefore the development of the night time inversion layer can not be captured in detail. However, the model temperature is in reasonable agreement with the observations.
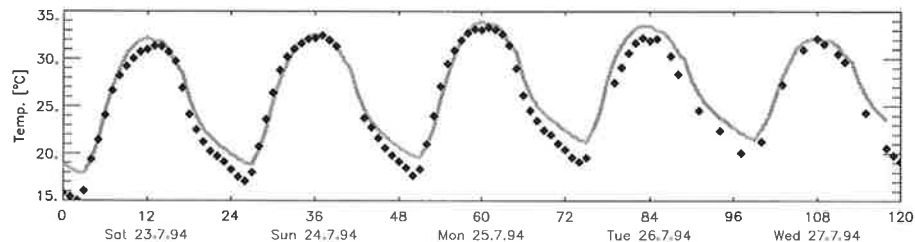
Figure 4.4: Time series of observed (points) and modelled (solid line) temperatures [°C] at 2 m height as averaged over the stations and the corresponding model grid boxes in the area of Berlin-Brandenburg.
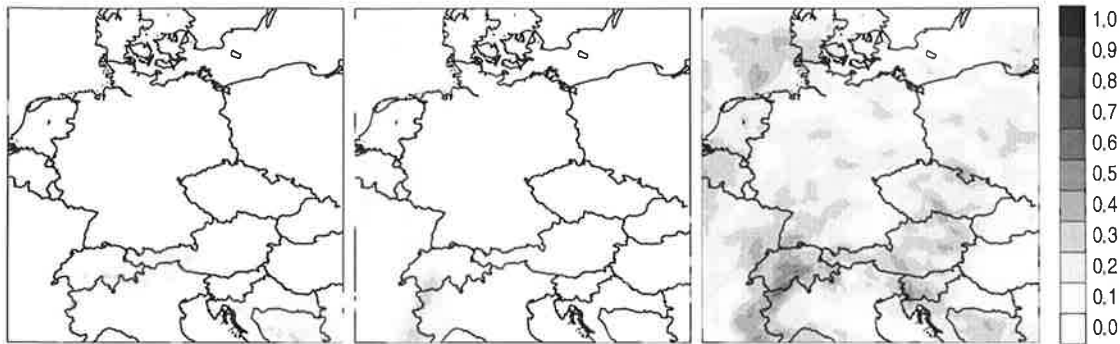
Figure 4.5: Cloud cover as simulated by the REMO 1/6° model. The cloud cover is averaged over the FLUMOB episode (July 23 until July 28) and separated into three levels: low level (left panel), medium level (middle), high level (right panel). Contours every 10% of cloud fraction.

The modelled cloud cover averaged over the FLUMOB period (July 23 until July 28) is presented in Fig. 4.5. To enable a cloud classification, the cloud coverage is separated into three levels: low level clouds appear below 800 hPa, middle level clouds between 800 and 400 hPa, and high level clouds above 400 hPa. Focusing on the area of the FLUMOB campaign, Berlin-Brandenburg, no low and medium level cloud activity is modelled. Only high level clouds and thus cirrus cloud activity (Fig. 4.5, right panel) is simulated by the model with cloud cover reaching 10 - 30%. The comparison of the simulated cloud cover with satellite pictures and weather observations showed that the FLUMOB episode was almost cloud free with only some high cirrus clouds occurred. But on the 26th some convective activity and weak thunderstorm activity appeared in Brandenburg. These events are underestimated by the model, which also explains the modelled temperature overestimation on the 26th. Apart from these events the modelled cloudiness corresponds to the observations. However, the observed cloud activity was rather weak and maybe of a too small scale to be covered by the regional model. Another reason for the underrepresentation of cloudiness in the model simulation might be an underestimation of the specific humidity in the lower troposphere.

4.3   Meteorological GESIMA Simulation
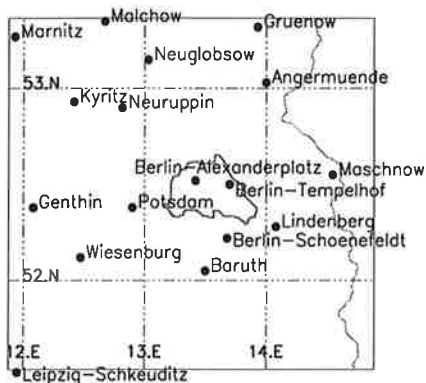
Figure 4.6: Locations of the weather observation stations in Berlin-Brandenburg.

As the REMO simulation was compared to the mean weather condition, the GESIMA simulation is analysed in more detail because the higher resolution of the GESIMA simulation enables a comparison of the model results to single station measurements. Figure 4.6 gives an overview about the geographical distribution of the observation stations of the German Weather Service in Berlin-Brandenburg used for the validation of meteorological parameters. A statistical evaluation is calculated for the time series of observed and model simulated parameters. The statistical parameters as introduced in appendix C are used here to evaluate the meteorological

simulation of near surface data:

Table 4.1: Statistics of Time Series of 2 m Temperatures*
* The terms n, b, r^2 and d are dimensionless, while the remaining terms have units of °C.
The statistical parameters are described in appendix C.

Station	n	$\overline{O}$	$\overline{M}$	δ_O	δ_M	b	a	E	E_S	E_U	r^2	d
Angermünde	138	24.82	27.34	6.29	6.79	0.75	4.09	5.63	5.07	2.43	0.96	0.94
Baruth	142	24.30	24.85	6.86	4.73	0.64	8.21	2.95	1.67	2.43	0.95	0.94
Berlin-Alexanderplatz	141	27.83	28.44	4.20	6.81	1.53	-15.68	3.21	2.13	2.40	0.97	0.92
Berlin-Schönefeld	138	25.31	27.56	5.76	6.69	0.83	2.36	5.25	4.82	2.09	0.95	0.93
Berlin-Tempelhof	138	26.72	27.46	4.82	6.57	1.25	-7.63	2.96	2.54	1.51	0.95	0.95
Genthin	136	24.38	27.64	7.21	6.46	0.51	10.23	7.12	5.97	3.88	0.91	0.89
Grünow	135	25.58	27.38	5.95	6.65	0.88	1.25	4.45	4.10	1.73	0.95	0.95
Kyritz	142	25.60	24.65	5.88	4.60	0.68	8.83	3.08	2.36	1.98	0.92	0.93
Leipzig-Schkeuditz	134	24.64	27.86	6.52	6.47	0.55	9.24	6.88	5.98	3.40	0.94	0.91
Lindenberg	138	26.43	24.68	4.42	4.72	0.75	7.78	3.90	3.51	1.70	0.96	0.94
Malchow	135	25.26	28.07	5.84	6.82	0.71	5.08	6.27	5.71	2.60	0.95	0.92
Marnitz	138	25.19	27.70	6.64	6.31	0.62	7.84	5.90	5.12	2.93	0.90	0.91
Maschnow	142	24.75	27.81	6.23	6.85	0.66	6.19	6.57	5.89	2.90	0.97	0.92
Neuglobsow	142	24.67	24.57	6.08	4.67	0.71	6.99	2.36	1.63	1.70	0.93	0.95
Neuruppin	138	25.15	24.42	4.92	4.63	0.85	4.18	2.14	1.92	0.93	0.95	0.97
Potsdam	142	25.39	27.70	5.29	6.69	0.86	1.54	5.45	5.02	2.12	0.96	0.92
Wiesenburg	142	25.17	24.81	5.19	4.35	0.77	5.98	2.06	1.68	1.20	0.93	0.95

Table 4.1 lists the evaluation statistics calculated for all weather stations that reported temperature measurements. Hourly data sets are used for the analysis. The measurements are taken at 2 m height. The modelled 2 m temperature are interpolated to the 2 m level including the temperature in 10 m and at the Earth's surface in consideration of a logarithmic vertical profile (*Sorbjan*, 1986). The statistical analysis shows that the modelled mean temperatures $\overline{M}$ are slightly overestimated by about 1 - 2 °C. The standard deviations δ_O, δ_M are of the same range and compare quite well. The slope b of the least-squares fit is in most cases lower than unity, and the intercept a is greater than zero. Only the two city stations Berlin-Tempelhof and Berlin-Alexanderplatz show inverse coherence. The systematic component of the RMS errors E_S makes up the main part of the total RMS error E. Therefore, the statistical parameters indicate that the model produces a good linear fit with the observed temperatures, with accurate simulation of the temperature swing and a weak overestimation of the mean temperatures caused by overprediction of the daily maximum temperatures. The high values of the index of agreement d summarize the good agreement between the observed and modelled temperatures.

Two temperature time series at different locations representing urban and rural conditions, respectively, are shown in Fig. 4.7. The entire 168 h calculation is presented for the stations Berlin-Tempelhof and Neuruppin. The modelled time series resembles the observations nearly perfectly at station Neuruppin. Even the minimum temperatures during the early morning hours, which are systematically overestimated in the REMO model, are almost exactly simulated by the GESIMA model. The high accuracy of the model calculation is also indicated in the scatter plot where modelled temperatures are plotted against observed temperatures. At the urban station Berlin-Tempelhof the 2 m temperature is also modelled in good agreement with the observations but the maximum temperatures are overestimated. During July 26 this overprediction can be explained by the missing clouds in the simulation. However, strong overprediction of daily maximum temperatures occurs only at the two urban stations located directly in Berlin, Berlin-
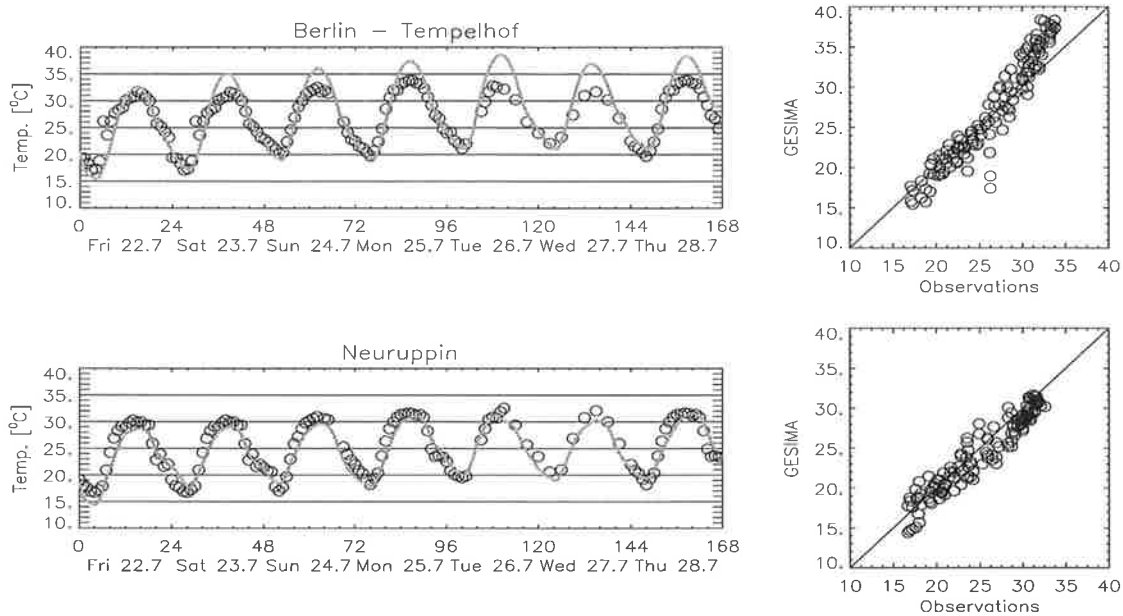
Figure 4.7: Modelled (solid line) and observed (circles) time series of temperatures at 2 m height in °C for Berlin-Alexanderplatz (upper left panel) and Neuruppin (lower left panel). Scatter plot of modelled vs observed temperatures for Berlin-Alexanderplatz (upper right panel) and Neuruppin (lower right panel). The thin black line represents perfect agreement.

Alexanderplatz and Berlin-Tempelhof. This overprediction is caused by overestimated surface temperatures at the urban model grid points. Additionally, near surface temperatures under heterogeneous city conditions are strongly influenced by the local conditions which inturn are subgridscale in the model.

Table 4.2: Statistics of Time Series of Wind Direction⋆

⋆ The terms n, b, r^2 and d are dimensionless, while the remaining terms have units of $°$.
The statistical parameters are described in appendix C.

Station	n	$\overline{O}$	$\overline{M}$	δ_O	δ_M	b	a	E	E_S	E_U	r^2	d
Angermünde	125	128	133	81	67	0.32	85	82	61	55	0.36	0.64
Baruth	130	128	118	55	62	0.54	63	60	54	25	0.52	0.73
Berlin- Alexanderplatz	140	140	129	55	68	0.31	99	76	66	37	0.29	0.59
Berlin-Schönefeld	139	118	120	65	64	0.47	61	66	56	34	0.47	0.71
Genthin	40	145	133	75	80	0.71	50	63	59	22	0.71	0.84
Grünow	133	130	136	64	63	0.51	60	62	53	31	0.55	0.74
Kyritz	130	121	146	71	70	0.48	50	74	64	38	0.69	0.80
Leipzig-Schkeuditz	84	145	136	74	74	0.05	136	101	74	69	0.07	0.52
Lindenberg	137	119	122	62	71	0.73	29	56	54	16	0.64	0.80
Malchow	116	130	164	77	55	0.25	88	84	61	58	0.68	0.74
Marnitz	101	147	164	68	68	0.62	45	61	54	27	0.72	0.83
Maschnow	116	130	164	77	55	0.25	88	84	61	58	0.68	0.74
Neuruppin	129	118	142	65	69	0.51	45	72	63	33	0.68	0.79
Neuglobsow	48	143	148	52	39	0.36	89	47	34	32	0.50	0.70
Potsdam	138	127	124	69	67	0.41	75	72	60	40	0.52	0.69
Wiesenburg	140	126	129	63	63	0.47	65	64	55	33	0.48	0.72
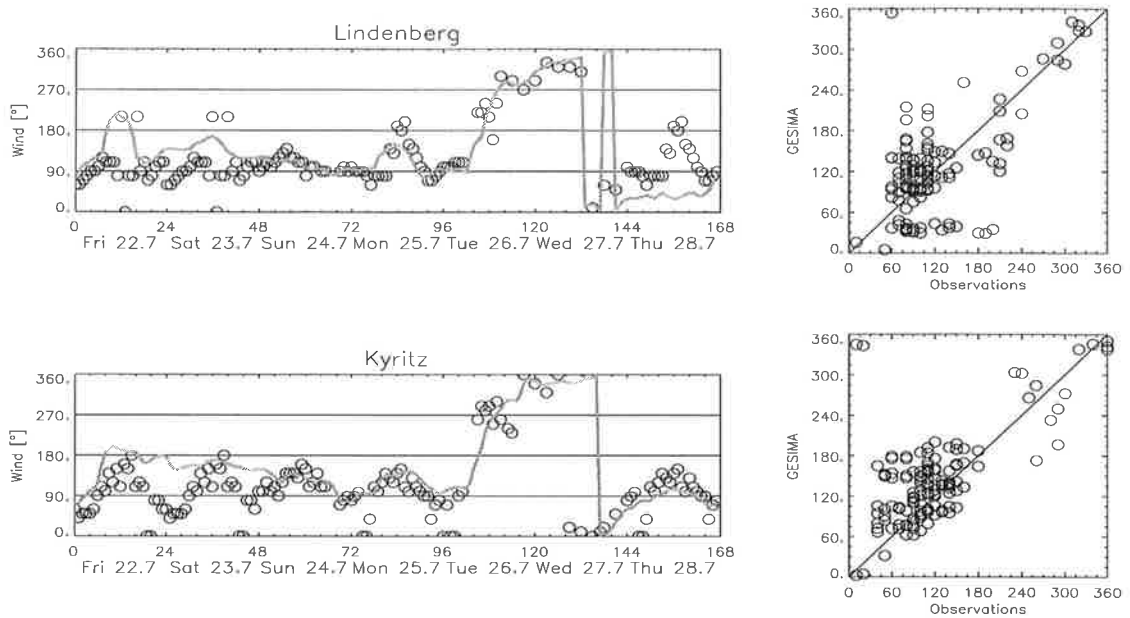
Figure 4.8: Modelled (solid line) and observed (circles) time series of wind direction in [°] for Lindenberg (upper panel) and Kyritz (lower panel). The observations are taken at 10 m height. Scatter plot of modelled vs observed wind speed for Lindenberg (upper right panel) and Kyritz (lower right panel). The thin black line represents perfect agreement.

The validation of the modelled wind field is separated into wind direction and speed. Table 4.2 shows the wind direction statistics. The index of agreement varies from a rather poor result of 0.52 for the station Leipzig-Schkeuditz, situated at the boundary grid point of the model domain, and reaches the agreement value 0.84 for Genthin, but generally is significantly greater then 0.5. The comparison of the mean observed and modelled values shows that the simulated wind directions are slightly clockwise rotated. The standard deviations show comparable variability and the systematic error dominates the total error. Time series of the wind direction at station Lindenberg, situated in the south-east of Berlin, and station Kyritz in the north-west of Brandenburg are presented in Fig. 4.8. The digital structures in the wind observations (Fig. 4.8 and 4.9) are caused by the coarse resolution of the FLUMOB data set. The observed wind directions show quite similar evolution which demonstrate the homogeneous conditions in Brandenburg during the FLUMOB episode. During the first four days the dominating wind direction was around east (90°) at station Lindenberg. At Kyritz a daily cycle is observed where the wind turns during the day to 180° and back to 90° during the night. In the morning of the 26th a large scale wind

Table 4.3: Statistics of Time Series of Wind Velocity*

* The terms n, b, r^2 and d are dimensionless, while the remaining terms have units of $[m/s]$.
The statistical parameters are described in appendix C.

Station	n	$\overline{O}$	$\overline{M}$	δ_O	δ_M	b	a	E	E_S	E_U	r^2	d
Berlin-Tempelhof	138	2.50	2.36	0.85	0.49	-0.006	2.5	1.16	0.71	0.92	0.1	0.36
Leipzig-Schkeuditz	83	1.8	2.0	0.76	0.6	0.01	1.77	0.99	0.65	0.75	0.2	0.45
Lindenberg	137	2.55	1.88	0.87	0.64	-0.14	2.83	1.35	0.91	1.00	0.48	0.45
Marnitz	100	2.26	2.05	1.11	0.56	-0.05	2.36	1.31	0.59	1.16	0.1	0.3
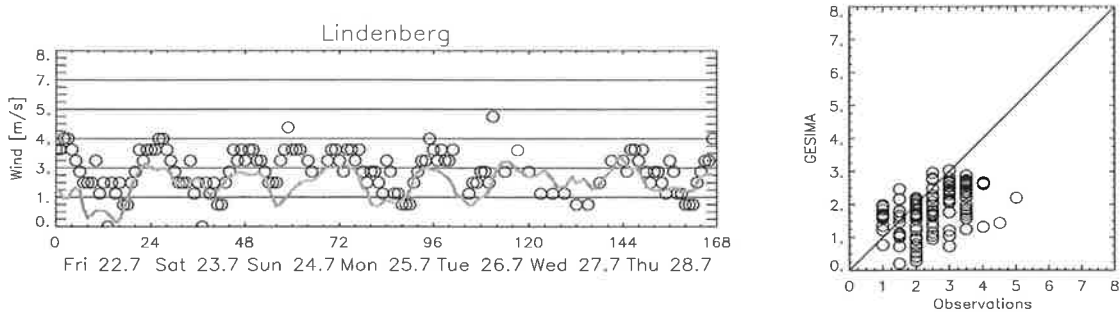
Figure 4.9: Modelled (solid line) and observed (circles) time series of wind speed in [m/s] for Lindenberg. The observations are taken at 10 m height. Scatter plot of modelled vs observed wind speeds. The thin black line represents perfect agreement.

turning begins. The described general characteristics of the wind field are reproduced by the model with some minor discrepancies.

A statistical validation of the simulated wind velocities is difficult because of the low wind speeds. Some statistical examples are given in Table 4.3. The observations and the model results show low and comparable wind velocities, but the weak amplitude of the variability leads to low indexes of agreement. However, the model resembles the observations reasonably. The time series at station Lindenberg (Fig. 4.9) indicates the weak wind velocities of about 2 m/s with a minimum of about 1 m/s in the afternoon and a maximum of about 4 m/s around midnight.

During the first days, the FLUMOB episode was characterized by very dry air masses. On the 26th more humid air masses were advected into the area of interest, Berlin-Brandenburg. Figure 4.10 shows a comparison between vertical profiles of radio-sondes data for relative humidity and the corresponding model results at station Lindenberg twice daily for three different days. The profiles show that humidity increases near the earth's surface from about 20% at noon on the 23rd up to 40% at the 27th (Fig. 4.10, lower panel) and from 40% to 60% at midnight (upper panel). The comparison demonstrates that the GESIMA simulation captures the increasing humidity, the night time inversion layer and the vertical gradient in the lowest 1500 m. In higher levels more deviations occur. One reason is a too low planetary boundary height in the model. For example on the 23rd (Fig. 4.10, left column) the planetary boundary height is about 200 m too low at noon.

Figure 4.10: Radio-sondes profiles (dashed line) and GESIMA profiles (solid line) for the relative humidity [%] between 0 to 3500 m height at Lindenberg on July 23, 25 and 27 at 00 UTC (upper panel) and 12 UTC (lower panel).

Table 4.4: Observed Maximum Heights of the Mixing Layer in [m]

	23.7	24.7	25.7	26.7	27.7
Lindenberg	2800	2900	3800	2800	2300
Kremmen	3200	3000	3300	-	2300

Table 4.4 summarizes observed maximum mixing heights at station Lindenberg and Kremmen as analysed by *Stark et al.* (1995). Before the 23rd the planetary boundary height extended to a height of approximately 3000 m. Between the 23rd and the 26th the maximum observed planetary boundary height increased up to 3300 m, and locally up to 3800 m. After the 26th the maximum mixing height decreased again reaching up to 2000 - 2300 m altitude. GESIMA simulates daily maximum mixing height between 2000 and 3000 m and REMO between 2000 and 2500 m, with higher mixing heights during the first days and lower mixing heights after the 26th. The planetary boundary height is generally underestimated in both models. The reason for this can be an underprediction of the turbulent fluxes during these hot weather conditions.

4.4 Discussion

The analysis of the meteorological simulation of the REMO model shows very satisfying results. The largest discrepancy was the nearly cloud free troposphere whereas weak cloudiness appeared in reality. This deviation leads to some overprediction in temperature and demonstrates the underprediction of humidity in the middle troposphere. However, the cloud free REMO simulation enables a better comparability between the REMO and the GESIMA simulations because all GESIMA simulations are calculated without physical and chemical cloud parameterizations. The results of the detailed quantitative error analysis of the 2 m temperature and wind simulation shows that GESIMA simulates the meteorological condition with reasonably good precision for the seven days of the simulation period. A realistic simulation of the wind field is of great importance for the chemical simulation because small deviations in the wind field influence the transport, and therefore the distribution, of the chemical species. The vertical profiles show deviations between the observed and modelled planetary boundary height. The model tends to underpredict the planetary boundary height which also influences trace gas concentrations strongly. The main deviations between the REMO and the GESIMA model occur in the planetary boundary layer. The reason for this is the higher horizontal and vertical resolution of the GESIMA model which redundantize a detailed comparison between the REMO and the GESIMA simulation. The homogeneous weather condition and the flat topography in the area of Brandenburg lead to no small-scale meteorological phenomenon during the FLUMOB episode. Even the observations show nearly no small-scale features, so that GESIMA represented the observed case and did not underpredict the horizontal variability. Therefore, this case was not very demanding for the dynamical and physical part of the non-hydrostatic meso-scale model. It is important to note that in this investigation the chemical condition is the main interest and the simple meteorological condition is therefore very useful because it simplifies the analysis of the chemical simulation.

5 Validation of Simulated Trace Gas Concentrations

The weather condition during the FLUMOB measurement episode was optimal for the photolyt-ical production of ozone and other photooxidants because of high temperatures and strong solar irradiation. Due to the meteorological conditions the FLUMOB period can roughly be divided into two episodes. The first episode from July 22 until July 25, was characterized by advected air masses coming from the south-east. Strong vertical mixing raised the planetary boundary layer height up to 3000 meters. During the following days the FLUMOB area was influenced by sub-tropical air masses coming from southern directions. In addition to high ozone concentra-tions high amounts of precursor gases were transported to the Berlin - Brandenburg area during the second episode. In the following the period from July 22 to July 25, 1994 will be denoted as *episode I* and the period between July 25 until the end of the measurement campaign, July 28, will be named *episode II*.

5.1 Trace Species Observations during FLUMOB

Throughout the FLUMOB measurement campaign chemical trace gas concentrations were measured at several stations in Berlin and Brandenburg. The geographical distribution of the stations is indicated in Fig. 5.11 (left panel) for the area of Berlin-Brandenburg. The monitoring stations in Berlin are presented in Fig. 5.11 (right panel) separately because of the high density of urban stations. Stations take measurements 3.5 meters above ground. Only two elevated stations are included: Turm Frohnau where the trace gases are sampled at 324 meters and Grunewald where measurements are taken at the standard level and additionally at 25 meters. At these stations concentrations of ozone, nitrogen oxide, nitrogen dioxide, sulfur dioxide and carbon monoxide were observed, but only the measurements of ozone and nitrogen dioxide were reported completely. Therefore, only ozone and nitrogen dioxide observation are used here for the validation of model results. However, it would have been beneficial to have more
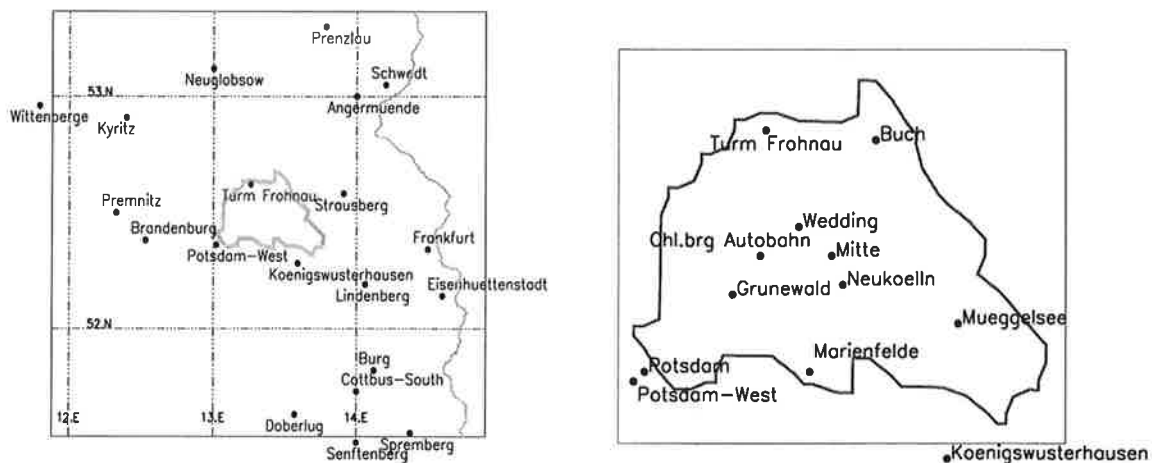
Figure 5.11: Map of the area Berlin-Brandenburg (left panel) including the locations of the monitoring stations. Expanded view of the locations of the monitoring stations in Berlin (right panel).

monitoring sites located in the south-west in the domain so that the surface observations would cover the whole model area. Besides these stationary observations, aircraft measurements were carried out several times every day in the planetary boundary layer. Two different airplanes took part: The motor gliders S10VC from MetAIR (*Neininger and Bäumle*, 1994) and ASK-16 from the Free University of Berlin (*Stark et al.*, 1995). Ozone concentrations above the planetary boundary layer were observed by three ozone radio soundings only.

5.2   Time Series Statistics

The GESIMA model simulation is validated by using time series of half hourly observed surface concentrations. The statistical measures are introduced in appendix C. The statistics are calculated individually for each observing station. No station is neglected independent of the stations representativity compared to the volume of a model grid boxes. The calculated performance statistics for each station highlights systematic errors in the simulation caused by local effects, as shown below.

The performance statistics for ozone simulations at all stations are listed in Table 5.5. The model performs well for all stations, with indices of agreement, d, ranging from 0.53 to 0.93. The

Table 5.5: Near Surface Ozone Time Series Statistics

The terms n, b, r^2 and d are dimensionless, while the remaining terms have units of [ppb$_v$].

The statistical parameters are described in appendix C.

Station	n	$\overline{O}$	$\overline{M}$	δ_O	δ_M	b	a	E	E_S	E_U	r^2	d
Angermünde	316	51.5	41.8	21.7	20.1	0.51	30.1	22.0	18.7	11.7	0.88	0.88
Berlin-Buch	333	50.7	40.9	22.0	22.6	0.58	26.8	22.9	20.2	10.7	0.87	0.87
Berlin-Char. Autobahn	325	21.0	31.0	17.1	24.1	0.43	7.6	26.8	24.6	10.6	0.65	0.71
Berlin-Grunewald	168	43.5	24.3	30.4	22.8	0.17	39.3	38.6	29.1	25.3	0.85	0.77
Berlin-Marienfelde	334	54.6	39.3	22.1	24.4	0.33	41.5	31.4	27.3	15.5	0.89	0.82
Berlin-Mitte	333	43.5	42.1	20.2	23.1	1.00	1.1	11.0	10.9	1.3	0.88	0.93
Berlin-Müggelsee	335	54.1	44.3	22.8	23.1	0.57	28.4	23.4	20.5	11.1	0.85	0.87
Berlin-Neukölln	335	50.0	40.1	20.7	23.2	0.61	25.1	23.0	20.7	10.0	0.88	0.88
Berlin-Wedding	333	43.7	41.2	22.2	23.6	0.87	7.6	13.8	13.3	3.5	0.84	0.91
Brandenburg	329	51.1	38.9	20.4	22.7	0.42	34.5	26.9	23.7	12.8	0.84	0.82
Burg	281	45.8	48.9	16.2	21.6	0.76	8.5	18.3	17.7	4.5	0.62	0.75
Cottbus-Süd	276	50.6	48.9	18.0	21.9	0.84	9.2	16.0	15.7	3.1	0.70	0.82
Doberlug	314	44.7	49.1	23.2	19.6	0.55	17.5	18.5	15.2	10.6	0.72	0.83
Eisenüttenstadt	276	42.4	50.8	16.7	18.3	0.41	21.0	21.2	18.5	10.3	0.72	0.77
Frankfurt a.O.	279	55.9	47.8	18.5	20.5	0.53	30.3	21.4	19.2	9.6	0.75	0.81
Königswusterhausen	328	50.7	29.8	25.6	25.1	0.08	48.3	40.1	32.5	23.5	0.82	0.72
Kyritz	320	54.0	40.3	20.9	21.5	0.26	43.2	29.2	24.5	15.7	0.78	0.77
Lindenberg	334	68.0	46.6	16.7	19.5	-0.25	79.7	35.4	28.0	21.5	0.83	0.53
Neuglobsow	327	55.3	43.6	18.9	17.9	0.26	43.7	25.0	20.5	14.2	0.80	0.78
Potsdam	145	51.2	41.2	24.3	27.0	0.70	22.1	24.1	21.9	10.0	0.89	0.90
Potsdam-Observatorium	239	54.8	40.8	20.0	26.4	0.33	41.0	31.9	28.7	14.0	0.75	0.75
Postdam-West	202	54.4	28.5	25.9	27.9	-0.05	55.9	46.2	38.0	26.3	0.86	0.66
Premnitz	329	62.7	40.6	19.8	20.7	-0.16	69.6	38.0	29.9	24.4	0.84	0.59
Prenzlau	330	62.6	49.5	25.4	21.1	0.33	45.8	28.7	22.8	17.3	0.83	0.82
Schwedt	330	57.7	45.5	22.4	21.5	0.40	39.3	26.6	22.5	14.2	0.85	0.83
Spremberg	281	50.0	60.3	16.5	16.6	0.16	40.1	23.7	19.2	13.9	0.61	0.67
Strausberg	197	50.8	42.5	18.4	21.2	0.61	24.9	21.0	19.1	8.7	0.81	0.85

Table 5.6: Near Surface NO_2 Time Series Statistics

The terms n, b, r^2 and d are dimensionless, while the remaining terms have units of $[ppb_v]$.
The statistical parameters are described in appendix C.

Station	n	O	M	δ_O	δ_M	b	a	E	E_S	E_U	r^2	d
Angermünde	299	7.6	7.1	6.6	4.4	0.30	5.3	6.0	3.9	4.6	0.47	0.64
Berlin-Buch	306	8.1	15.6	6.7	9.8	-0.30	12.9	15.0	11.9	9.0	0.37	0.30
Berlin-Chl.brg Autobahn	279	53.6	27.9	22.0	14.5	-0.54	68.9	43.4	22.9	36.8	0.10	0.12
Berlin-Grunewald	165	18.1	32.5	15.8	16.7	-0.10	21.5	28.1	21.9	17.5	0.60	0.55
Berlin-Marienfelde	333	10.4	17.9	7.5	11.8	0.02	10.0	15.8	14.0	7.3	0.65	0.59
Berlin-Mitte	332	23.2	15.2	12.3	10.0	-0.01	23.5	17.9	12.8	12.5	0.49	0.55
Berlin-Müggelsee	242	7.4	12.9	5.0	7.6	-0.36	12.2	11.5	8.9	7.2	0.26	0.27
Berlin-Neukölln	333	16.1	17.1	9.5	10.8	0.55	6.6	10.4	9.5	4.3	0.50	0.70
Berlin-Wedding	328	18.9	15.8	13.4	10.4	0.32	13.8	13.4	9.9	9.1	0.50	0.67
Brandenburg	328	13.1	11.9	6.2	11.6	0.71	4.6	10.9	10.7	1.9	0.41	0.56
Burg	261	5.0	4.0	4.5	2.8	0.11	4.5	4.9	2.9	4.0	0.25	0.47
Cottbus-South	270	9.9	5.3	7.9	4.6	-0.23	11.1	11.6	6.1	9.8	0.03	0.22
Doberlug	274	6.4	4.2	3.9	2.6	-0.00	6.4	5.2	3.4	4.0	0.41	0.50
Eisenhuettenstadt	277	10.8	5.2	11.4	3.3	-0.07	11.2	13.8	6.42	12.2	0.49	0.29
Frankfurt a.O.	280	8.6	7.8	7.6	5.8	0.12	7.6	8.8	5.78	6.6	0.18	0.43
Königswusterhausen	328	10.5	25.6	9.3	15.2	-0.49	23.3	25.1	19.5	15.8	0.50	0.22
Kyritz	248	7.0	9.1	5.0	6.1	0.10	6.0	7.9	6.4	4.5	0.24	0.45
Lindenberg	255	3.9	5.9	2.4	3.8	-0.01	4.0	4.9	4.2	2.4	0.40	0.48
Neuglobsow	213	2.7	4.5	0.9	4.0	-0.85	6.5	4.6	4.0	2.3	0.06	0.0
Potsdam	118	14.7	17.3	8.5	13.6	1.00	-2.7	10.8	10.5	2.5	0.74	0.79
Potsdam-Observatorium	239	11.8	19.4	7.1	16.6	0.23	7.2	18.9	18.0	5.7	0.69	0.56
Schwedt	329	5.5	8.1	4.0	5.0	0.10	4.7	6.6	5.6	3.6	0.44	0.56
Spremberg	281	8.2	3.1	5.3	1.9	-0.40	9.5	9.0	4.4	7.8	0.32	0.05
Strausberg	186	3.3	4.3	2.1	2.1	-0.25	4.4	3.5	2.2	2.7	0.07	0.23

good accuracy of the model is indicated by smaller unsystematic error values, E_U, compared to the systematic error, E_S. The differences between the model results and the observations is almost linear. This is indicated by similar standard deviations for the observations and the simulated concentrations. The relatively large values of the linear regression intercept, a, and the low values of the slope, b, indicate that the model has some difficulties in producing very high ozone concentrations. The comparison of the mean modelled and observed ozone values shows that the model underpredicts the observed ozone concentrations except at five stations. Four of these stations, Burg, Eisenhüttenstadt, Spremberg and Doberlug, are located close to the lateral boundaries of the model domain in the predominant inflow direction indicating deficiencies in the surface layer caused by nesting of two models with different vertical resolution. These stations are strongly influenced by advected air masses from outside the model domain. High ozone concentrations are advected over the night into the lowest level of the GESIMA model area. This is due to the coarser vertical resolution of the REMO model. The lowest model layer of the REMO model extends to approximately 80 m height above ground whereas in the GESIMA model the lowest box is only 20 m high. Overnight, close to the earth's surface a stable cold air layer develops in which ozone is removed by reaction with nitric oxide and dry deposition. This leads to the development of a steep vertical ozone gradient in the near surface layers during the night which is not resolved by the REMO simulation. Therefore, overestimated ozone concentrations are advected overnight into the GESIMA domain and influence the first lateral gridpoints at the inflow boundary close to

the surface as demonstrated at the four stations discussed. The fifth station where the mean ozone concentration is overestimated is 'Berlin-Charlottenburg Stadtautobahn'. Because of its special location directly at the city motorway this station is strongly influenced by extreme local traffic emissions, causing low ozone concentrations, which can not be resolved in detail by the model. However, also other stations are each more or less locally influenced. For example, the Potsdam, Potsdam-Observatorium and Potsdam-West stations are located close to each other but obviously different ozone concentrations are observed. Nevertheless, from this first comparison it can be summarized that the model captures the characteristics of the observations except for the total amount of ozone which is systematically underpredicted .

The statistics for the nitrogen dioxide simulations are listed in Table 5.6. The indices of agreement vary strongly between the single stations. The mean simulated and observed NO_2 mixing ratios are comparable and overprediction and underprediction occur with similar frequency. At some stations, there is no correlation at all between the modelled and observed NO_2 mixing ratios. NO_2 is a highly reactive substance with a short lifetime under sunny weather conditions and at some stations the concentrations are extremely low. However, the quality of the simulated near surface NO_2 concentrations is of satisfying precision.

Table 5.7: O_3 Time Series Statistics

Station	n	$\overline{O}$	$\overline{M}$	δ_O	δ_M	b	a	E	E_S	E_U	r^2	d
Grunewald 25 m	165	52.5	38.2	25.2	20.5	0.24	43.0	30.7	23.9	19.2	0.80	0.77
Turm Frohnau 324m	333	71.9	64.9	12.8	12.5	0.31	51.4	16.1	13.3	9.0	0.74	0.76

Table 5.8: NO_2 Time Series Statistics

Station	n	$\overline{O}$	$\overline{M}$	δ_O	δ_M	b	a	E	E_S	E_U	r^2	d
Grunewald 25 m	165	16.56	20.46	15.3	13.9	0.41	8.0	15.7	12.8	9.0	0.56	0.71
Turm Frohnau 324m	249	3.49	3.59	4.8	3.3	0.18	2.8	5.0	3.2	3.9	0.26	0.46

Table. 5.7 and Table 5.8 show the statistics for the two elevated stations Grunewald and Turm Frohnau. The locations have an ozone index of agreement of 0.77 and 0.76, respectively. Additionally, the standard deviations show similar variability. For the point measurement at Turm Frohnau this is a particularly good result. As discussed before, at Turm Frohnau total ozone is slightly underestimated as well, but only by about 5 ppb$_v$.

5.3 Single Station Analysis

The time series of half hourly ozone and NO_2 mixing ratios for the entire FLUMOB episode will be discussed exemplary at three different stations. The stations have been carefully selected to represent different characteristics of trace gas distributions in the model domain. Urban conditions are represented by Berlin-Mitte (Fig. 5.12) which is located in the center of Berlin. Observations from Neuglobsow (Fig. 5.13) represent rural conditions in the predominant downwind direction of Berlin and Cottbus-South (Fig. 5.14) shows ozone and NO_2 mixing ratios in the dominant upwind direction of Berlin in the south-east corner of the domain.

The ozone time series at Berlin-Mitte show that the model simulates urban ozone mixing ratios with high accuracy. The simulation of the NO_2 concentrations is less precise but the mean concentrations and variability match the observations. At Berlin-Mitte the NO_2 concentrations
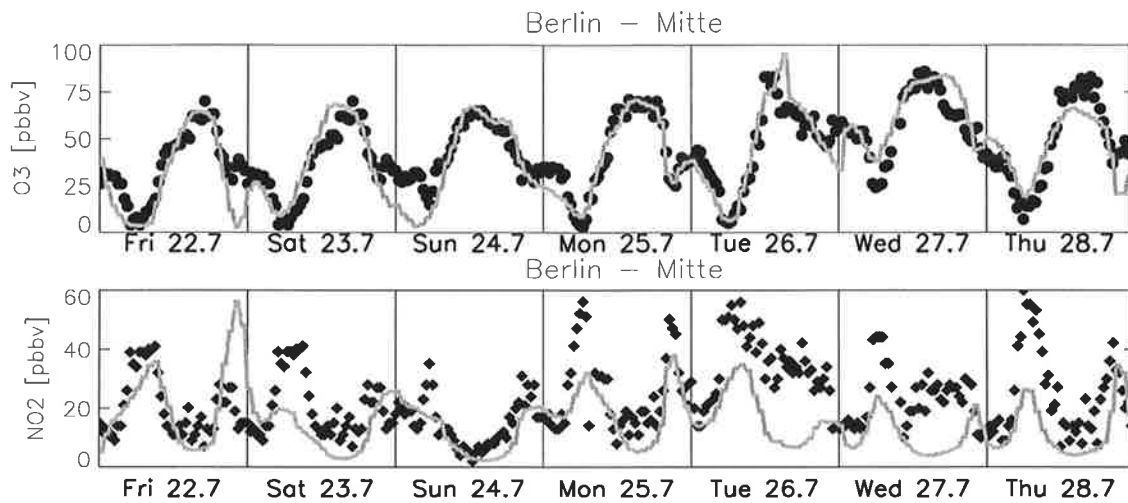
Figure 5.12: Berlin-Mitte time series of modelled (grey line) and observed (black circles) mixing ratios for ozone (upper panel) and nitrogen dioxide (lower panel). The mixing ratios are given in ppb$_v$.

vary between 10 and 60 ppb$_v$. The diurnal cycle shows a double peak structure with maximum values in the early morning and in the evening hours corresponding to the traffic rush hours. During *episode II* (July 25 until 28) higher NO_2 concentrations are observed compared to *episode I* (July 22 until 25). This feature is not reproduced by the model and will be explained in section 5.5.3. The steady increase of measured ozone and NO_2 concentrations indicates an enhanced ozone production capacity. Generally, the ozone concentrations exhibit a diurnal cycle with a minimum in the early morning hours before dawn and a maximum in the afternoon.
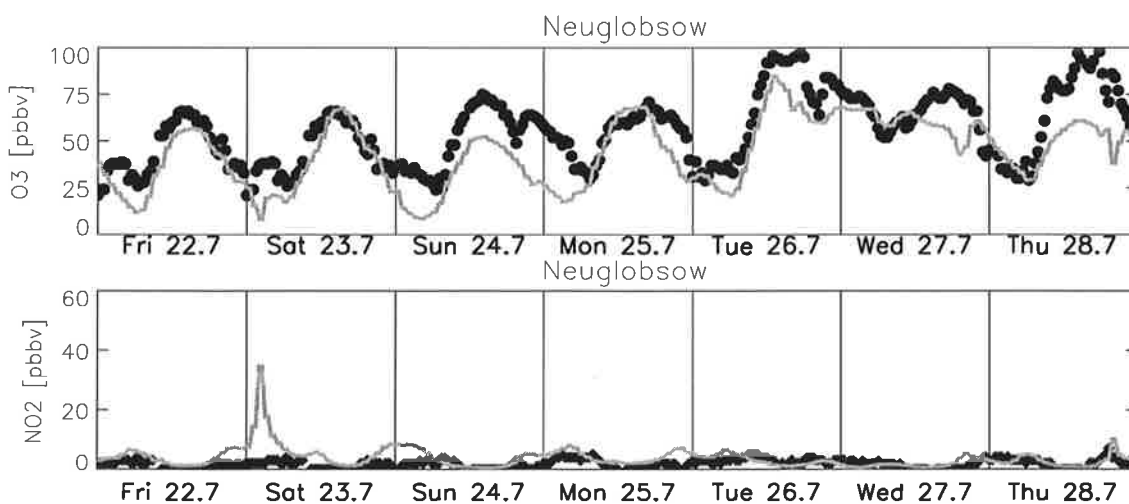
Figure 5.13: Neuglobsow time series of modelled (grey line) and observed (black circles) mixing ratios for ozone (upper panel) and nitrogen dioxide (lower panel). The mixing ratios are given in ppb$_v$.

This pattern results from the daytime photochemical production and is intensified at days by the downward transport of ozone enriched air from the residual layer. Ozone loss throughout the day occurs by dry deposition and reaction with nitric oxide. At night, when photochemical production ceases, the vertical transport is inhibited by an inversion layer. At the urban station, Berlin-Mitte, the local NO emissions are strong enough to cause complete nighttime ozone depletion.

The rural nature of the Neuglobsow station is evidenced by the extremely low NO_2 concentrations around 3 ppb$_v$ as shown in Figure. 5.13. Therefore, ozone observed at Neuglobsow is not produced by local emissions. Rather it must have been transported to this rural station by horizontal advection and downward vertical mixing. The predominant wind direction, except during the July 26 - 27 period was south-east, so that Neuglobsow was influenced by the Berlin city plume. Ozone concentrations at Neuglobsow reach the same daily maximum values during *episode I* as observed at Berlin-Mitte, but during *episode II* even higher ozone concentrations appear at the rural station. Ozone maximum concentrations increase by about 30 ppb$_v$ from *episode I* to *episode II*. In contrast to the urban station, the nocturnal ozone depletion does not destroy ozone completely due to the absence of NO in this rural area. In general, the model captures the features of the station but underestimates the ozone mixing ratio.

Cottbus-South is located in the south-east of Brandenburg. The NO_2 mixing ratio measurements (Fig 5.14) show low concentrations during *episode I* and enhanced concentrations during *episode II*. It should be noted that the measurements on Friday the 22th are missing and the two following days are weekend days where emissions are generally smaller. However, ozone concentrations increase day by day. On July 27, Cottbus was influenced by the Berlin city plume due to wind direction turning. On all other days Cottbus was upstream of Berlin.

The scatter plots for the ozone concentrations for the three monitoring stations discussed above and given in Fig. 5.15 summarize the quality of the model simulation at these sites. The best result are at the rural station Berlin-Mitte. This highlights that local ozone production close to the anthropogenic emission sources is well captured by the model. These results reflect
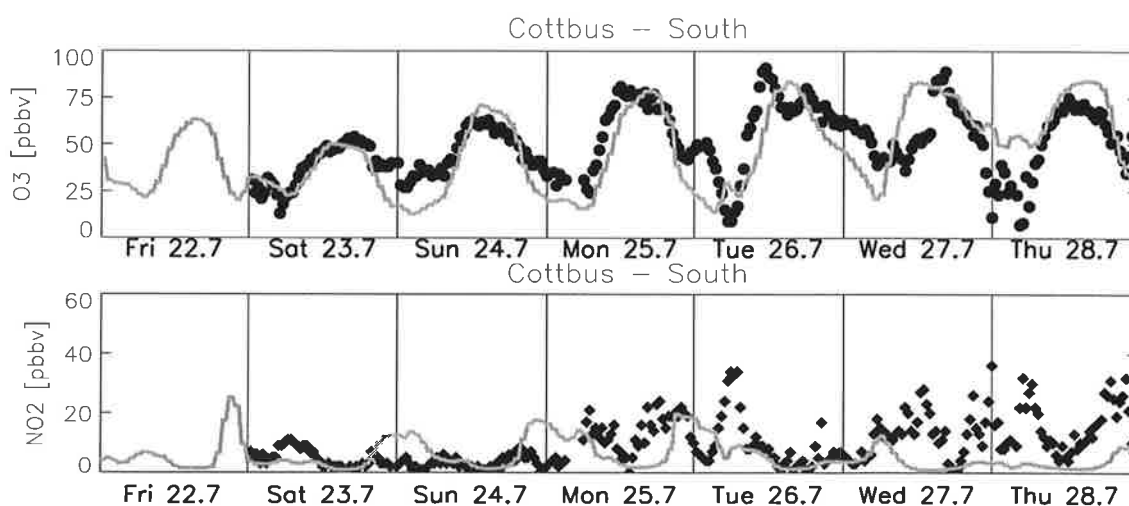
Figure 5.14: Cottbus-South time series of modelled (grey line) and observed (black circles) mixing ratios for ozone (upper panel) and nitrogen dioxide (lower panel). The mixing ratios are given in ppb$_v$.
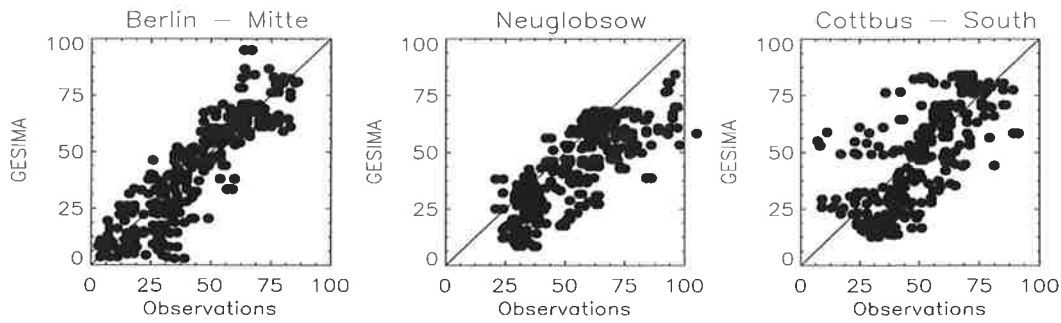
Figure 5.15: Scatter plot of modelled vs observed ozone mixing ratios in ppb_v for Berlin-Mitte (left panel), Neuglobsow (middle panel) and Cottbus-South (right panel). The solid line indicate perfect agreement.

the high quality of the anthropogenic emission data sets. At the Neuglobsow and Cottbus-South stations ozone is generally underpredicted. At Cottbus-South this effect is somehow masked by the overprediced ozone during night between the 27th and the 28th (Fig.5.14). However, we can conclude that surface ozone is slightly underpredicted in the rural environment.

The Grunewald station, located in a forest of Berlin, provides the daily cycle of the vertical ozone gradient (Fig. 5.16, upper panel), because measurements are taken in 3.5 m and 25 m above the ground. These values are compared with simulated ozone concentrations in the first and the second model layer (Fig. 5.16, lower panel) representing the conditions at 10 m and 30 m, respectively. The comparison shows that the ozone concentrations are quite similar
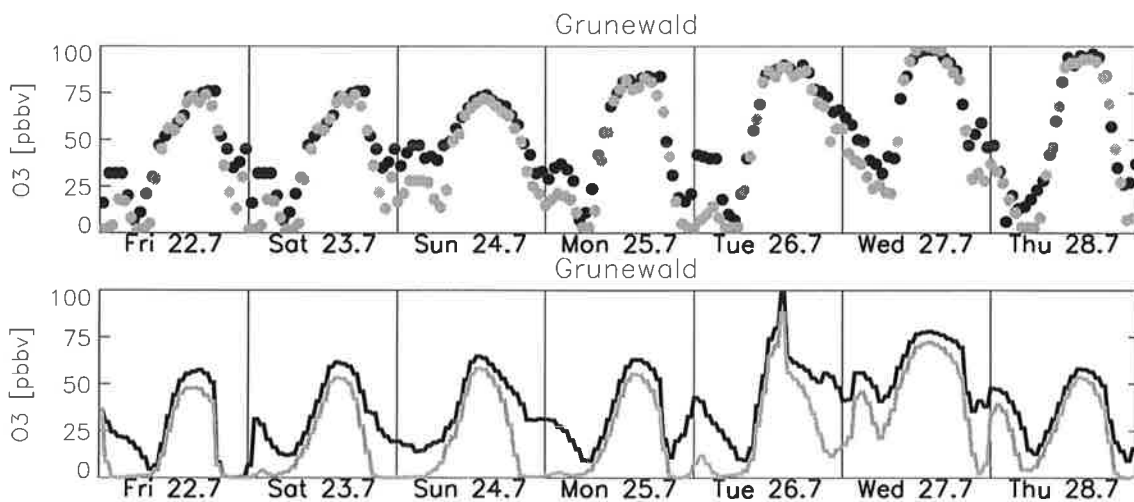
Figure 5.16: Grunewald time series of observed ozone concentrations (upper panel) at two different heights. The measurements are taken in 3.5 m height (grey dots) and 25 m height (black dots). The modelled ozone concentrations (lower panel) are given for the first model layer representing concentrations at 10 m (grey line) and the second model layer (black line) representing concentrations at 30 m. All mixing ratios are given in ppb_v.
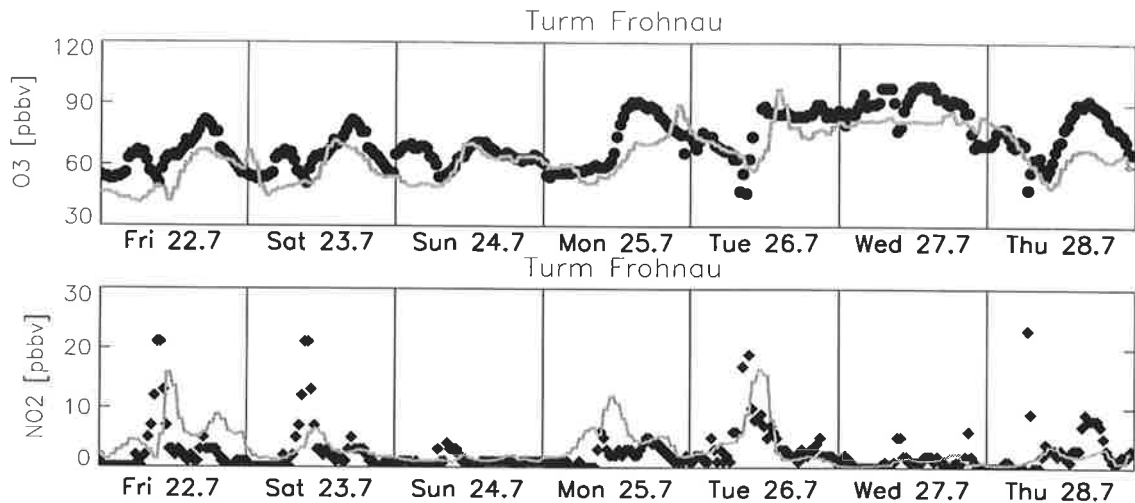
Figure 5.17: Turm Frohnau time series of modelled (grey line) and observed (black circles) mixing ratios for ozone (upper panel) and nitrogen dioxide (lower panel) in 324 m height. The mixing ratios are given in ppb$_v$.

Figure 5.18: Scatter plot of modelled vs observed ozone mixing ratios in ppb$_v$ for Turm-Frohnau. The solid line indicates the perfect agreement.

during the daytime, but the nocturnal ozone depletion is stronger in the near surface level. This vertical feature is well simulated by the model. But at this grid point the near surface ozone concentrations are underestimated because the model resolution is still too coarse to resolve the city forest, thus background city conditions are assumed in the model. However, these measurements demonstrate the importance of high vertical resolution to enable the comparison between simulated ozone concentrations and ground based measured ozone concentrations.

Further insight into ozone concentrations in a higher atmospheric layer is given by measurement at Turm Frohnau. This tower is located in the north of Berlin and the measurements are taken at 324 m height. Figure 5.17 shows the time series of modelled and observed ozone and NO$_2$ concentrations. At night the tower measurements represent the concentrations of the reservoir layer above the ground inversion. During the day, the monitoring point at 324 m height is located in the mixing layer. At this level the ozone concentrations show a weak diurnal cycle. The comparison between observed and simulated NO$_2$ concentrations at this elevated level shows that the model is able to simulate the NO$_2$ peaks which indicate convective events when NO$_2$ is vertically mixed within the boundary layer. Enhanced ozone concentrations on July 25 are caused by the local ozone production over Berlin because this day the tower was influenced by the city plume. But after the 25th, the tower was again independent of city pollutants, so that background ozone concentrations were measured. Again, the differences are clearly visible with Ozone concentrations increasing about by 20 - 30 ppb$_v$ between *episode I* and *II*. The ozone scatter plot (Fig. 5.18) shows that ozone is still reasonably simulated at this elevated station. As analysed already at the rural stations a slightly underprediction of ozone occurs.

To get a more detailed three-dimensional picture of photochemical air pollution and to study the reason from the rural ozone underprediction, two days of this summer smog event will be studied in detail. Saturday July 23 will be analysed as an example of a day during *episode I* and Tuesday, the 26th will be studied for *episode II*. These days are reasonably representative as documented in Table. 5.9 where the quantitative error statistics are calculated for every day including all surface based monitoring stations. The index of agreement, d, varies between 0.71 and 0.87.

Table 5.9: Surface Ozone Time Series Statistics (day by day)

Day		n	$\overline{O}$	$\overline{M}$	δ_O	δ_M	b	a	E	E_S	E_U	r^2	d
Friday	22-07-94	438	41.0	30.0	22.5	22.6	0.38	29.4	25.2	21.7	12.8	0.82	0.81
Saturday	23-07-94	547	42.3	32.8	20.4	19.9	0.35	30.6	25.2	21.7	12.8	0.75	0.77
Sunday	24-07-94	547	46.2	34.8	18.7	22.0	0.29	35.8	25.6	22.6	11.9	0.77	0.74
Monday	25-07-94	569	47.1	39.4	24.2	24.4	0.57	24.4	22.3	19.8	10.3	0.79	0.84
Tuesday	26-07-94	593	54.1	44.6	27.3	26.5	0.57	28.5	24.2	21.2	11.3	0.85	0.87
Wednesday	27-07-94	576	58.5	56.0	25.9	21.9	0.51	29.4	18.5	14.6	11.3	0.74	0.80
Thursday	28-07-94	546	52.5	46.6	27.8	21.2	0.35	36.1	24.0	17.0	16.8	0.66	0.71

5.4   Saturday July 23, 1994

5.4.1   Comparison of Horizontal Distributions

Saturday, July 23, was the first day of the measurement campaign and the second day of the model simulation. Figures 5.19 and 5.20 compare the observed and modelled horizontal distributions of near surface ozone and NO_2, respectively. The filled circles depict the observed concentrations. In Fig. 5.20 the simulated wind direction is also presented. The color bar scales can differ from one figure to another. The figures present the results for three different times of the day: At 5 UTC in the morning when the remaining concentrations from the night start to get mixed with the early morning emissions or freshly produced pollutants, around 14 UTC when ozone concentrations maximize, and 21 UTC for evening concentrations shortly before sunset when photochemical production ceases.

The predominant observed wind direction was south-east for this day. During the day the wind turned to south and back to south-east. The mean wind velocity was rather weak with observed velocities of about 1-3 m/s. The horizontal distribution of modelled NO_2 compares well with the observed concentrations (Fig. 5.19). Even the strong local gradient of the NO_2 concentrations in the city area of Berlin is simulated by the model. In the morning maximum NO_2 mixing ratios occur in the city of Berlin, above the motorways and a little bit further downwind of these strong emission sources. High NO_2 concentrations are modelled in the morning in the north-west of Berlin. This NO_2 partly originates from NO_x that was accumulated in Berlin over the night and advected to the north during the early morning. The south-easterly wind direction advected this residual of high NO_x concentrations directly over the motorway so that the concentrations are additionally enriched by freshly emitted NO_x. During the day (Fig. 5.19, middle panel) the NO_2 concentrations are very low due to the fast NO_x consumption by photochemical reactions. Only close to the emission sources does NO_2 appear with weak amounts of about 0 - 10 ppb$_v$. In

the evening (Fig. 5.19, right panel) the NO_2 mixing ratio increases due to the decreasing photo-chemical activity.

The comparison between the observed and simulated ozone concentrations is presented in Fig. 5.20. In the morning total ozone depletion occurs in the city and very low ozone concentrations are found close to the motorways. Highest ozone concentrations are visible in the rural areas between the motorways. The high concentrations at the inflow boundary are advected from outside into the model domain. This is caused by the discrepancy of the vertical resolution between GESIMA and REMO as has previously been discussed. In the afternoon maximum ozone concentrations occur in the downwind direction of Berlin. No isolated city plume develops on this day because the predominant wind direction advects the city ozone and ozone precursors over the motorway where there is a residual of NO concentrations thereby preventing the development of a simple structured city plume due to NO titration close to the motorway. The high ozone mixing ratios in the south-west of the domain are produced by locally emitted precursors and by advected pollutants and precursors coming from outside the domain from the area around Halle - Bitterfeld. In the evening the fastest ozone depletion occurs in the NO_x contaminated urban regions. In the rural environment ozone destruction is slower.

The comparison shows that ozone is well modelled in the urban area of Berlin. Even the local structures inside the city area can be reproduced by the model. For example the strong ozone depletion close to the big motorways in the western part of Berlin is well represented. How-
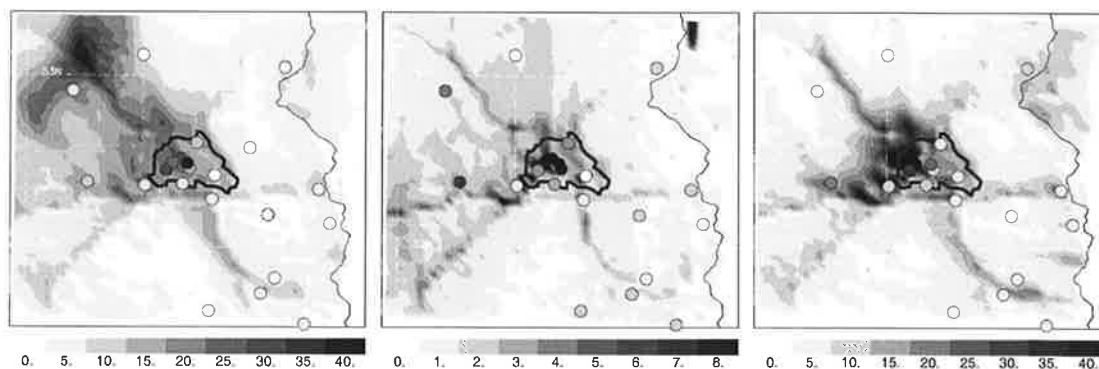
Figure 5.19: Near surface NO_2 concentrations in ppb_v at 5 UTC (left panel), 14 UTC (middle panel) and 21 UTC (right panel). Observations are overlayed by the circles.
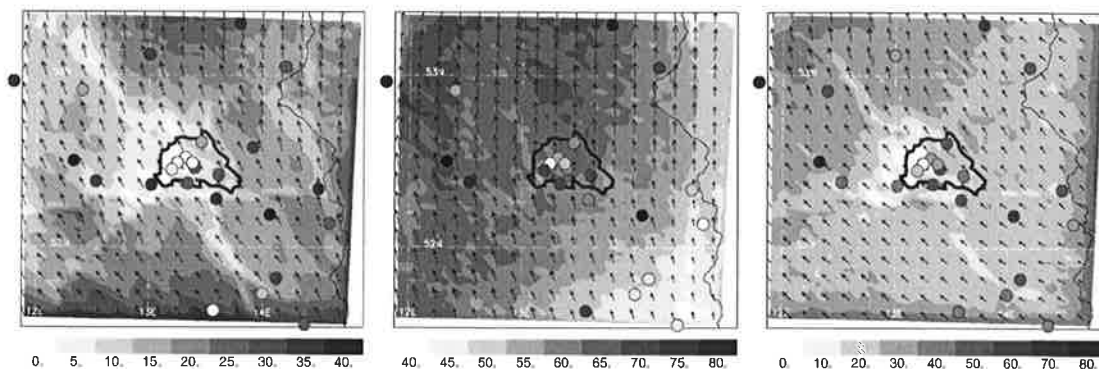
Figure 5.20: Near surface O_3 concentrations in ppb_v and wind directions at 5 UTC (left panel), 14 UTC (middle panel) and 21 UTC (right panel). Observations are overlayed by the circles.

ever, surface ozone is partly underpredicted in the rural environment, independent of whether the station is located upstream or downstream of Berlin.

5.4.2 Vertical Trace Gas Distributions on the 23rd

In the planetary boundary layer the distribution of atmospheric pollutants are measured by aircraft. Two different motor gliders participate in the FLUMOB campaign. One plane from the Free University of Berlin called ASK16 and another one from the MetAIR. During MetAIR flights ozone and NO_2 concentrations were monitored. During the ASK flights only ozone was measured. Table 5.10 shows all flight times for July 23. The simulated vertical ozone distributions at 6 MEZ, 15 MEZ and 22 MEZ (Fig. 5.21) illustrate the three dimensional structure of ozone distributions and facilitate the interpretation of the aircraft measurements. Figure 5.21 shows a vertical cut from west to east along the 52.5°N latitude. Berlin is situated in the center of the figures. In the morning and evening a vertical gradient of ozone concentrations occurs with minimum values at the surface and total ozone depletion close to and downwind of the city. In the afternoon hours the planetary boundary layer up to 2000 m is well mixed and maximum ozone concentrations of about 70 ppb$_v$ are visible downwind of Berlin.
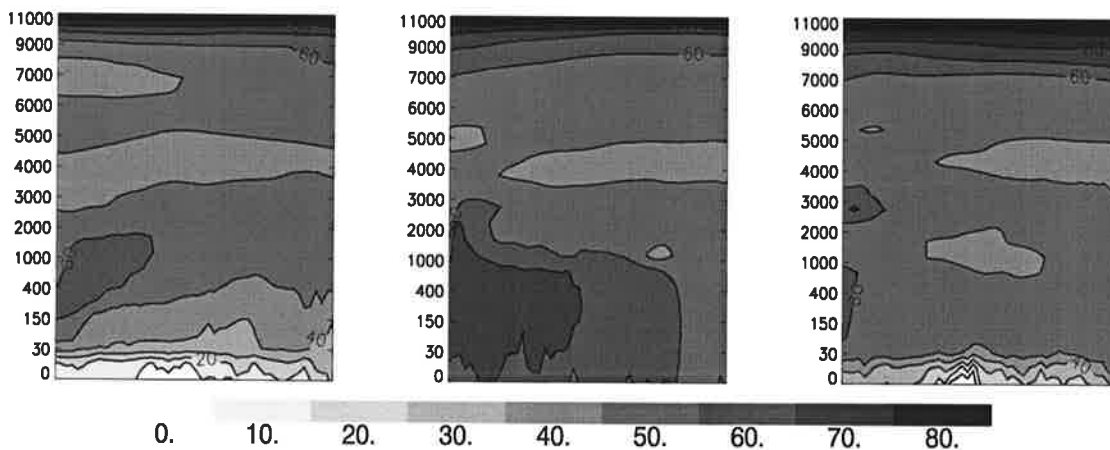
Figure 5.21: Vertical O_3 distribution in ppb$_v$ along 52.5°N latitude at 6 MEZ (left panel), 15 MEZ (middle panel) and 22 MEZ (left panel). The height niveaus are given in meters.

To compare aircraft measurements with model results the simulated concentrations are interpolated in space and time onto the flight pattern using a pointer technique (*Schaller and Wenzel*, 1999) as shown in Fig. 5.22 to Fig. 5.27. The measured concentrations are represented by the black dashed line. The grey solid line indicates the GESIMA simulation. The thin dashed line represents the concentrations as simulated by the REMO 1/6° model:

Table 5.10: Flight Times of MetAIR and ASK16 on July 23, 1994

5	6	7	8	9	10	11	12	13	14	15	16	17	18	19MEZ
				MetAir 1							MetAir 2			
	ASK 1						ASK 2				3	4		
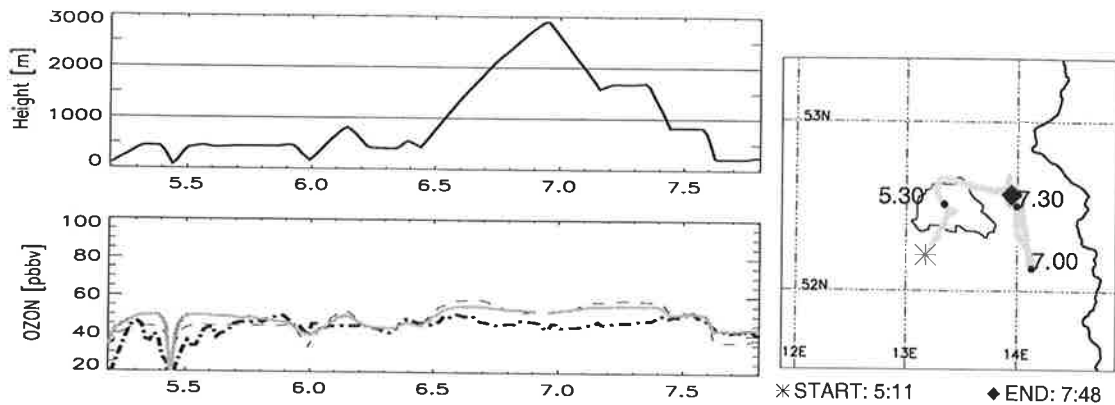
Figure 5.22: Flight ASK 1: Horizontal (right panel) and vertical (upper panel) flight pattern of flight ASK16 A on July 23. Time series of measured (black dashed line), GESIMA (grey solid line) and REMO (thin dashed line) modelled ozone concentrations (lower panel) in [ppb$_v$].

- ASK 1: Ozone was monitored in the morning hours. First the plane crossed Berlin at 500 m altitude (Fig. 5.22). Then a vertical profile was taken in the upwind direction of Berlin. Measured and simulated ozone shows quite similar concentrations of about 40 - 50 ppb$_v$. The measured concentrations almost remain constant up to 3000 m altitude during the vertical sounding. This shows that no residual layer with accumulated ozone concentrations was present this morning (see also Fig. 5.21).

- MetAIR 1: The flight started in the upwind direction of Berlin, circled and crossed the city at about 500 m altitude (Fig. 5.23). The simulated ozone concentrations show only small horizontal variability. In the upwind direction ozone is slightly underpredicted before 10 MEZ. After 10 MEZ ozone is underpredicted by about 20 ppb$_v$ over the city. The
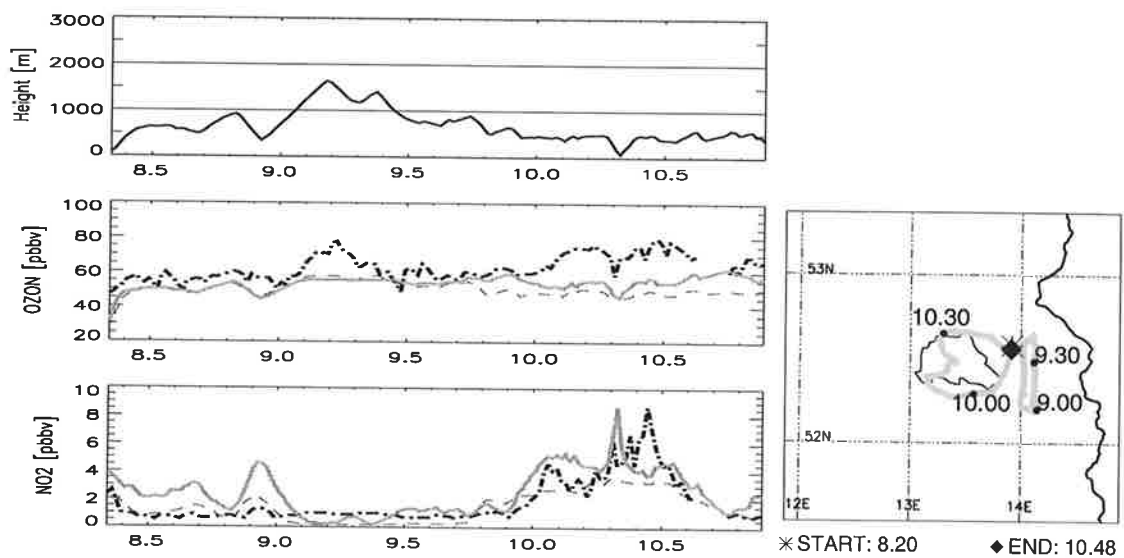
Figure 5.23: Flight MetAIR 1: Horizontal (right panel) and vertical (upper panel) flight pattern of flight MetAIR A on July 23. Time series of measured (black dashed line), GESIMA (grey solid line) and REMO (thin dashed line) modelled ozone (middle panel) and NO$_2$ (lower panel) concentrations in [ppb$_v$].
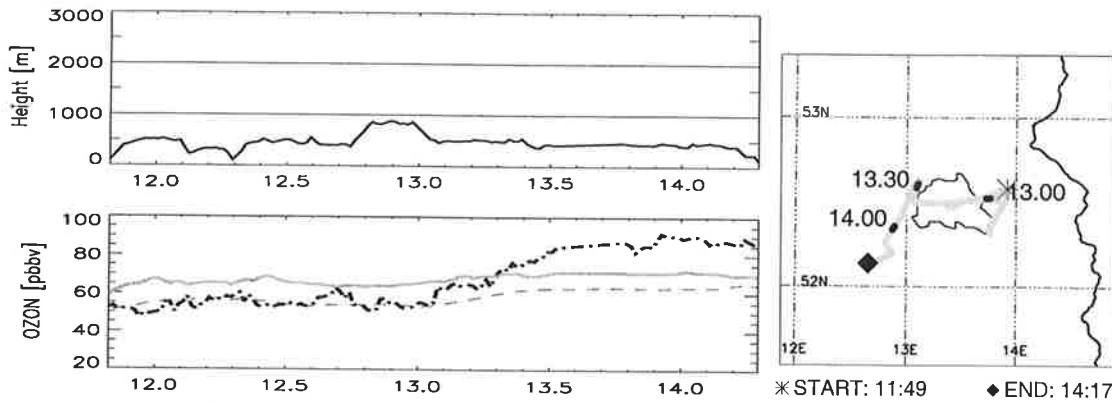
Figure 5.24: Flight ASK 2: As Fig. 5.22 but for the flight ASK16 B.

simulation of the NO_2 concentrations resembles the observations. Relatively small concentrations of NO_2 were measured and simulated in the upwind direction of Berlin. Only a small peak occurs around 9 MEZ. This peak most probably originates from emissions from Cottbus. A strong increase of NO_2 occurs in the measurement as well as in the simulation between 10 and 10.30 MEZ when crossing the city.

- ASK 2: This flight crossed Berlin in the early afternoon at about 500 m altitude (Fig. 5.24). The measured ozone concentrations increases from 50 to 90 ppb_v from the upwind to the downwind direction. The simulated concentrations only increase by about 10 ppb_v.

- MetAIR 2: The total flight period was three and a half hours (Fig. 5.25). During that time two other flights with the ASK16 plane were carried out for different flight paths. Two vertical profiles up to 2000 m altitude were measured. This altitude still was inside the planetary boundary layer as shown by the constant values of the measured ozone concentrations. The amount of measured ozone increased on the flight track from the upwind to the downwind direction. Measured and simulated concentrations are quite similar
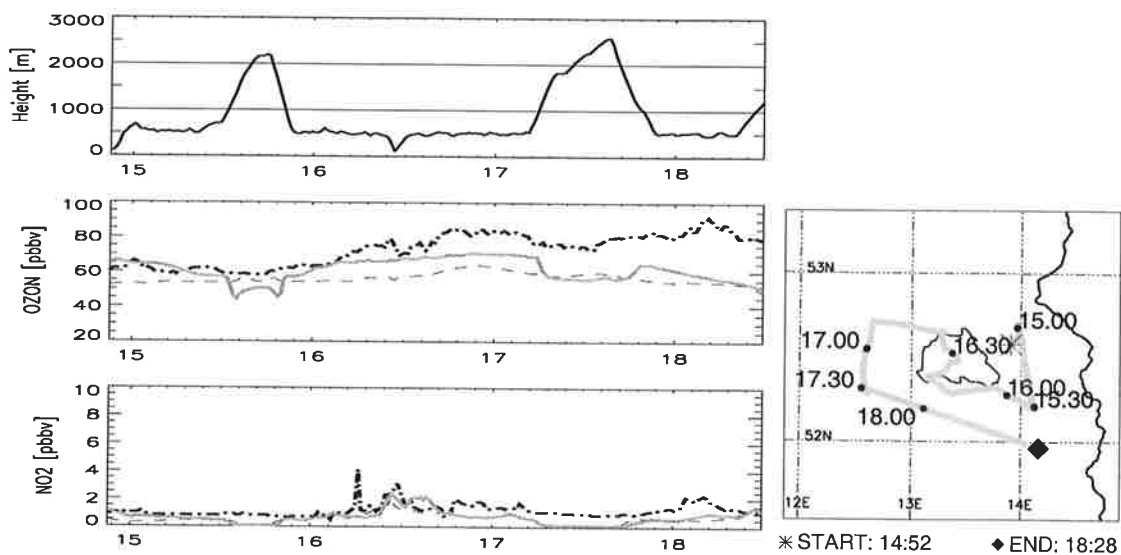
Figure 5.25: Flight MetAIR 2: As Fig. 5.23 but for the flight MetAIR B.
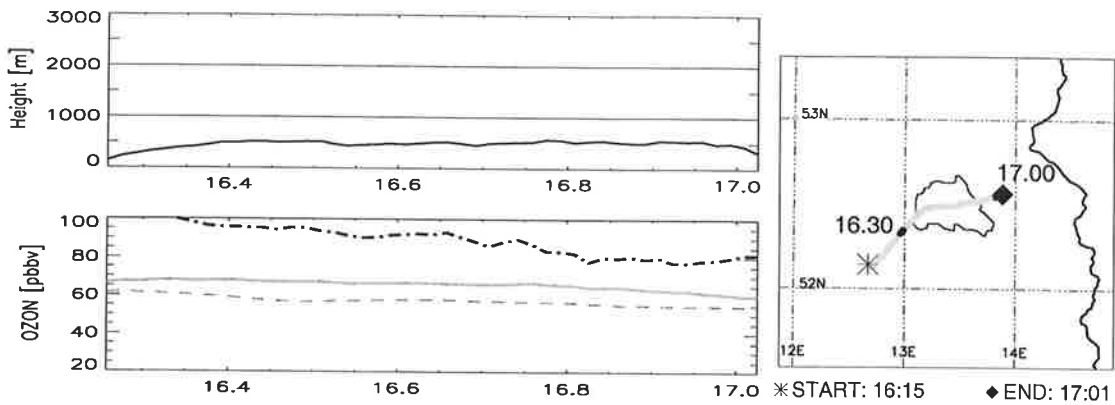
Figure 5.26: Flight ASK 3: As Fig. 5.22 but for the flight ASK16 C.

during the first two hours in the upwind direction. Modelled ozone is slightly underestimated above the city and dramatically underestimated in the south-west of the domain. Both measured and simulated NO_2 concentrations are low. Slightly elevated NO_2 concentrations occur over Berlin and when crossing the Berlin-Cottbus motorway at around 18 MEZ.

- ASK 3: The flight crossed over Berlin and measured decreasing ozone concentrations from more then about 100 to 80 ppb_v (Fig. 5.26). GESIMA shows constant concentrations of about 70 ppb_v.

- ASK 4: The measurements are taken in the upwind direction of Berlin and ozone mixing ratios of 80 - 90 ppb_v are observed (Fig. 5.27). GESIMA underestimates the measured concentrations by 20 - 30 ppb_v.

Quality assurance studies for the FLUMOB flight measurements are discussed in *Kanter et al.* (1995). For ozone an confidence level of $\pm$ 15 % ($\approx$ 2 ppb) and for NO_2 $\pm$ 25 % ($\approx$ 1 ppb) were estimated (*Stark et al.*, 1995). No direct comparison measurements were carried out, but before and after each flight the instruments were calibrated and met the proposed quality levels. Nonetheless, the comparison shows rather good agreement for the GESIMA simulation
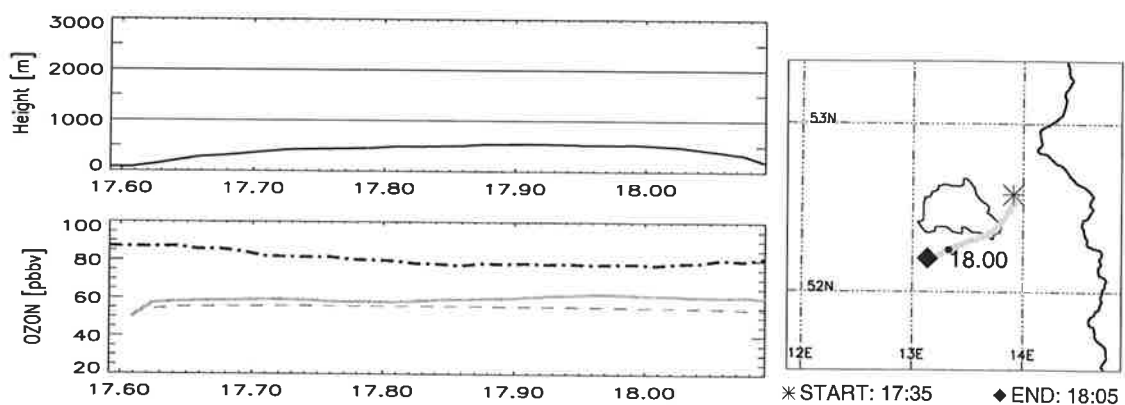
Figure 5.27: Flight ASK 4: As Fig. 5.22 but for the flight ASK16 D.

compared to the three flights which were carried out before 16 MEZ. During the following two hours, between 16 - 18 MEZ, ozone is underpredicted by the model. The strongest underestimation occurs in the south-east area of the domain. Due to the wind direction this area was strongly influenced by advected trace gases from outside of the domain during that day. Therefore, ozone underprediction is perhaps caused by underestimation of advected pollutants in the afternoon hours. After 18 MEZ there are no measurements. Nevertheless, the ozone concentrations as simulated by the GESIMA model mostly increase the simulation as carried out by the REMO model. The NO_2 concentrations, which were only observed during the two MetAIR flights are well reproduced by the GESIMA simulation.

5.4.3 Ozone Precursors

The comparison between the observed and modelled concentrations close to the surface and at the flight levels shows that ozone is well simulated in the urban areas but systematically underpredicted in the rural environment especially in the afternoon hours. However, the NO_2 concentrations seem to be in the right range. Ozone and NO_2 observations are insufficient to understand and reconstruct the process of ozone formation. Photochemical ozone formation strongly depends on the presence of volatile organic compounds (VOC's). Due to the absence of further useful measurements a theoretical study has been carried out. The basic O_3-VOC-NO_x chemical reactions will be summarized following the description of *Sillman* (1999), *Sillman et al.* (1990) and *Seinfeld and Pandis* (1998): Ozone production in the planetary boundary layer is initialized by photolysis of NO_2 (Eq. 5.1) followed by the rapid recombination of atomic oxygen (O) with molecular oxygen (O_2). Usually this reaction is counterbalanced by the reaction of NO with ozone (5.2).

$$NO_2 \xrightarrow{hv} NO + O \cdot \tag{5.1}$$

$$NO + O_3 \longrightarrow NO_2 + O_2 \tag{5.2}$$

But the NO_x-chemistry alone does not explain ozone production. The chemical process of ozone formation occurs via reaction sequences involving VOC and NO_x. Reactions transforming NO back to NO_2 without consuming ozone are important, so that NO_x acts as a catalyst (5.2). These reaction sequences are almost always initiated by reactions between hydrocarbons (RH) and OH:

$$RH + OH \cdot + O_2 \longrightarrow RO_2 \cdot + H_2O \tag{5.3}$$

$$RO_2 \cdot + NO \longrightarrow RO \cdot + NO_2 \tag{5.4}$$

$$HO_2 \cdot + NO \longrightarrow OH \cdot + NO_2 \tag{5.5}$$
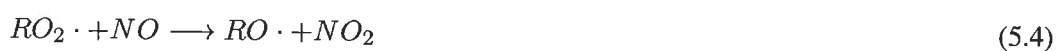
Reactions (5.4) and (5.5) convert NO back to NO_2 and result in the formation of ozone when followed by reaction (5.1). In urban or polluted atmospheres reaction (5.4) and (5.5) represent the dominant pathways for HO_2 and RO_2 radicals. In this case the rate of ozone production is controlled by the availability of odd hydrogen radicals (defined as the sum of OH, HO_2 and RO_2 after *Kleinman* (1986)). Odd hydrogen radicals are produced by photolysis of ozone, formaldehyde and other intermediate organics:

$$O_3 + H_2O \xrightarrow{h\upsilon} 2OH \cdot + O_2 \tag{5.6}$$

$$HCHO + 2O_2 \xrightarrow{h\upsilon} 2HO_2 \cdot + CO \tag{5.7}$$

They are removed by reactions that produce peroxide and nitric acid:

$$HO_2 \cdot + HO_2 \cdot \longrightarrow H_2O_2 + O_2 \tag{5.8}$$

$$RO_2 \cdot + HO_2 \cdot \longrightarrow ROOH + O_2 \tag{5.9}$$

$$OH \cdot + NO_2 \longrightarrow HNO_3 \tag{5.10}$$
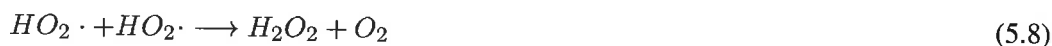
In order to better understand ozone production NO_x-sensitive and VOC-sensitive regimes are introduced. The split into these regimes is determined by the importance of the peroxide- and nitric-acid-formation reactions. When nitric acid represents the dominant sink of odd hydrogen, then the concentration of OH is determined by the equilibrium between reactions (5.6) and (5.10). In this case OH decreases with increasing NO_x and either remains constant or increases
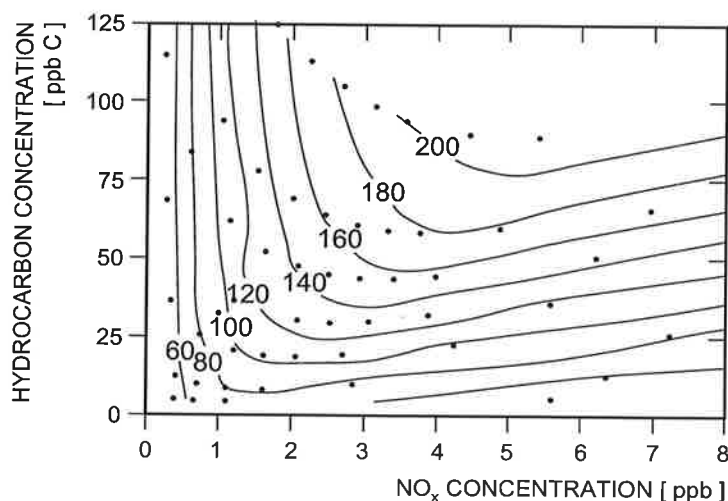
Figure 5.28: Ozone in ppb_v as function of the concentrations of NO_x and VOC after Sillman et al. (1990).

due to the impact of reaction (5.7) with increasing VOC. In the VOC-sensitive regime the rate of ozone formation is controlled by the hydrocarbon-OH reaction (5.3) and increases with increasing VOC and decreases with increasing NO_x. In the NO_x-sensitive regime peroxides represent the dominant sink for odd hydrogen, the sum $HO_2 + RO_2$ is relatively insensitive to changes in NO_x or VOC. The rate of ozone formation increases with increasing NO_x and is largely unaffected by VOC.

The relation between ozone, NO_x and VOC is presented in Fig. 5.28. This ozone isopleth plot shows ozone concentrations as a function of NO_x and VOC concentrations. The VOC concentrations are shown in parts per billion carbon $ppb_v C$. This unit is chosen to consider the reactivity of VOC species with respect to OH radicals rather than to the total amount of VOC. Highly reactive VOC consisting of at least ten carbon atoms, e.g. xylenes or isoprene, typically have relatively low ambient concentrations but high reactivity. The isopleth plot (Fig. 5.28) shows that ozone formation is a highly nonlinear process depending on the NO_x to VOC ratio as discussed in this section.
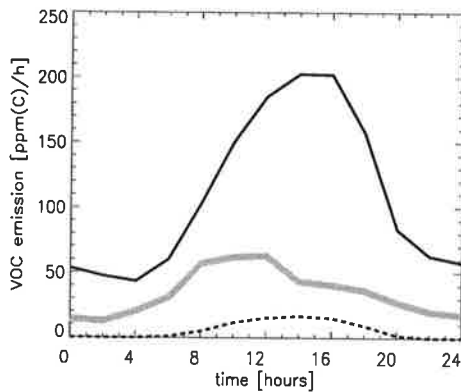
Figure 5.29: Anthropogenically (grey line) and biogenically (black line) emitted hydrocarbons as a function of time of the day (July 23, 1994). The isoprene emissions are plotted separately (black dashed line) but they are already included in the biogenic amounts. The emissions are sampled over the whole domain and shown in units of $ppbC$ per hour.

To characterize the composition of air masses in the area of Berlin-Brandenburg the emitted VOC's on July 23 are shown in Fig. 5.29 subdivided into their biogenic and anthropogenic origin. Biogenic hydrocarbon emissions significantly exceed the total emissions of anthropogenic hydrocarbons. The largest contribution to the biogenic hydrocarbons comes from monoterpenes. Monoterpenes are emitted by coniferous forests and are dependent on temperature. Isoprene emissions are rather small because of the small portion of deciduous forest in Brandenburg. Anthropogenically emitted hydrocarbons show a maximum between 8 and 12 UTC. This is a typical distribution for a Saturday where people work in the morning and rest in the afternoon. The horizontal distribution of anthropogenic and biogenic emission sources is presented in Fig. 5.30. The areal distribution of anthropogenic hydrocarbons shows maximum releases in Berlin. The distribution of the biogenic hydrocarbons shows the areas in Brandenburg covered by forests. The area as well as the total amount of biogenic emissions clearly exceeds the anthropogenically emitted hydrocarbons. To get a more detailed understanding about the O_3-VOC-NO_x regimes during this day in Brandenburg the VOC and NO_x emissions will be divided into three groups. One group (total) represents the conditions in the whole model domain. The second ground (city) represents urban conditions. These emission data sets are averaged over an area of 50×50 km^2 covering Berlin. Rural conditions are represented by the last group (rural) where the emission data sets are averaged over an area of 50×50 km^2 in the rural south-east of the domain. Figure 5.31 shows the diurnal emission cycle of these three groups scaled to the area of one grid box, e.g. 16 km^2. The total and the rural emitted VOC's show quite similar magnitude and diurnal cycle. The largest fraction of VOC is of biogenic origin. Therefore, a rural character dominates throughout the model area. The city emissions show an inverse pic-
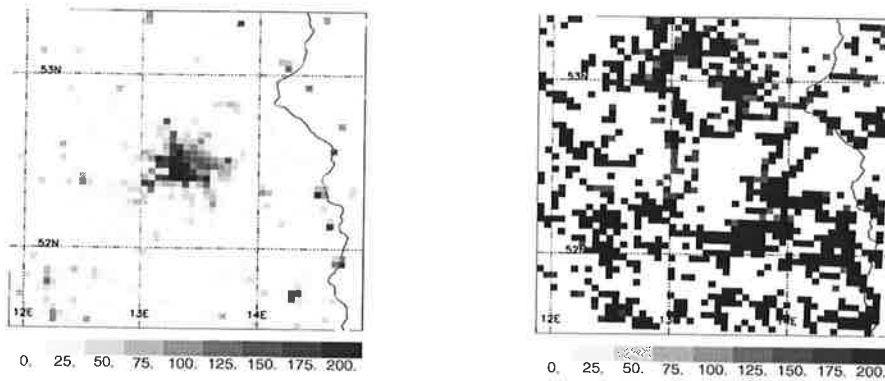
Figure 5.30: Anthropogenic VOC surface emissions (left panel) and biogenic VOC emissions (right panel) at 14 UTC on July 23 in ppb$_v$C per hour.

ture. Here the VOC's are dominated by anthropogenically emitted VOC's. The NO_x emissions of these three groups are shown in the lower right panel of Fig. 5.31. Maximum NO_x emissions are released in the city. The NO_x emissions in the total domain show a more rural character. The relation between the VOC and NO_x emissions of the total domain and their potential relation to ozone formation is illustrated in Fig. 5.32 (left panel). This plot shows the potential ozone production as a function of NO_x and VOC emission rates and is comparable to Fig. 5.28.
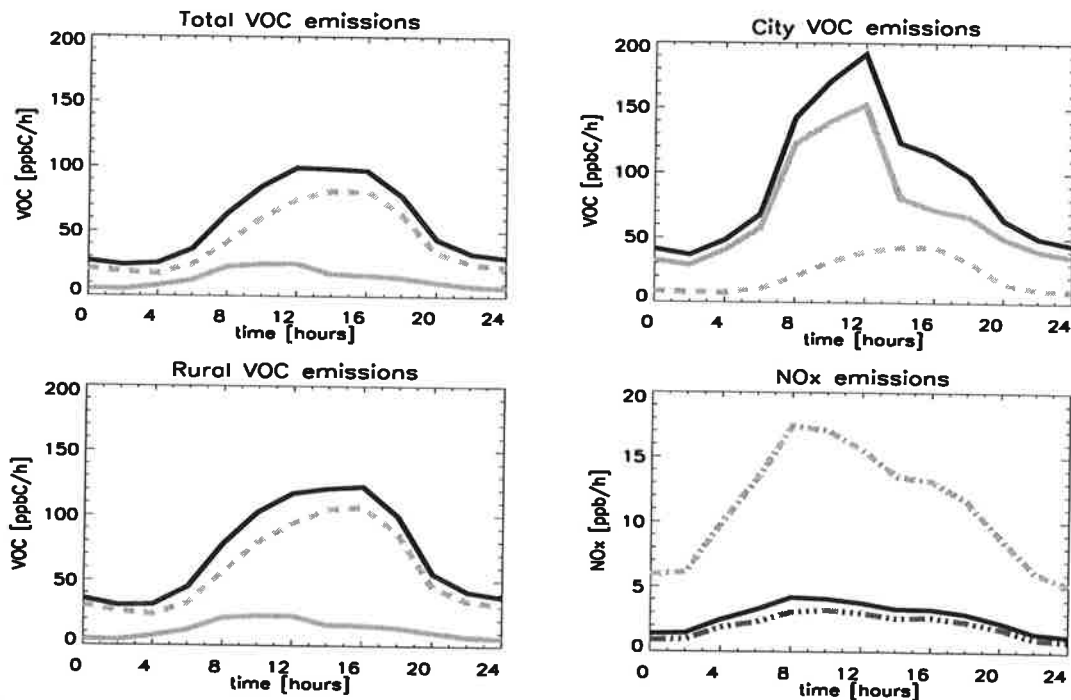
Figure 5.31: Surface emissions as released in Berlin-Brandenburg on July 23, 1994. Biogenically (grey dashed line), anthropogenically (grey solid line), and the sum of both (black solid line). The upper left panel shows the emissions in the whole model domain, the upper right panel for the city domain and the lower left panel for the rural area. NO_x emissions for the three groups total (black solid line), city (slash dot line), and rural (slash dot dot dot line) are shown in the lower right panel. The emissions are shown in ppb/h scaled to the size of one grid box, e.g 16 km^2
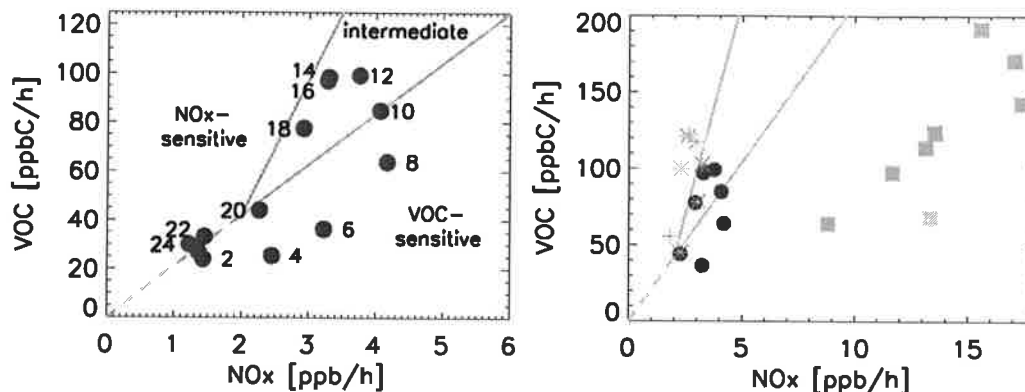
Figure 5.32: Total emissions of VOC versus NO$_x$ in ppb$_v$ per hour and grid box area. Emissions of the total domain (filled circles) are shown in the right and the left panel and marked by the time of the day. Grey squares represent the city conditions and the rural conditions are marked by the grey stars. The lines separate the VOC- and NO$_x$-sensitive areas.

In Fig. 5.32 the NO$_x$-sensitive and VOC-sensitive regimes are marked. The numbers represent the time of the day for the displayed data set. Note that the Berlin-Brandenburg area is NO$_x$-saturated. In the morning hours the area is definitely VOC-sensitive. At noon and during the afternoon hours the system is in an intermediate state where it is as well VOC-sensitive and NO$_x$-sensitive. A plot including all three groups of emission areas as discussed in this section is presented in the right panel of Fig. 5.32. Only data during day time, when photochemistry is active between 6 and 20 UTC, are included in that picture. The black bullets show the VOC - NO$_x$ correlation of the total domain, as presented in the left panel. The grey squares show the correlation of city emissions and the grey stars the VOC - NO$_x$ correlation of rural emissions. The city area is completely NO$_x$ saturated. Urban ozone formation is only dependent on the availability of VOC. The rural area is rather VOC-saturated. Increasing NO$_x$ as well as VOC concentrations will increase ozone formation in the rural environment.

However, the atmospheric composition is not exclusively characterized by directly emitted ozone precursors. Fig. 5.33 shows the VOC concentrations in the near surface layer of the GESIMA model at three different times on the 23rd: morning, afternoon, and evening. In the morning close to the main emission sources, i.e. Berlin and the forests, high VOC concentrations have accumulated. Downwind of these emission sources VOC is partly accumulated. This VOC was emitted over night and accumulated in the absence of photochemical transformation. Fig. 5.34 shows the fraction of anthropogenic VOC. It can be concluded that the high concentrations of VOC in the north-west of the domain originates from city emissions that are accumulated in the night and advected to this region. But generally the major part of VOC's in Brandenburg are of biogenic origin. In the afternoon VOC is quickly transformed into secondary pollutants so that hardly any VOC remains in the atmosphere. In the evening VOC begins to accumulate again. On this particular day maximum VOC concentrations occur in the areas where in the morning high amounts of ozone precursors exist (section 5.4.1). Aging polluted air masses are transported roughly on the same trajectory as the accumulated precursors in the night because of the nearly constant wind direction during the day. This leads to high amounts of ozone precursors in the overall downwind direction resulting in high ozone concentrations. Figure 5.33 and 5.34 indicate that hardly any VOC is advected into the model domain. This is a further reason for the
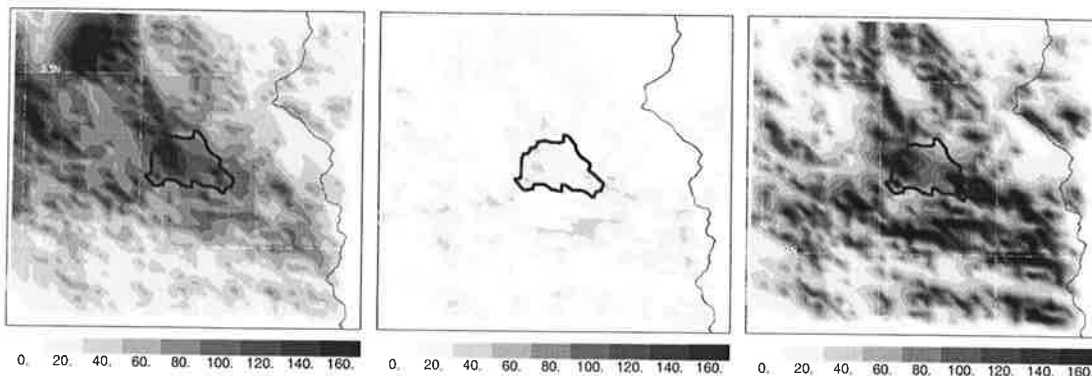
Figure 5.33: Total VOC surface concentrations in ppb$_v$C at 5 UTC (left panel), 14 UTC (middle panel) and 21 UTC (right panel), on July 23.
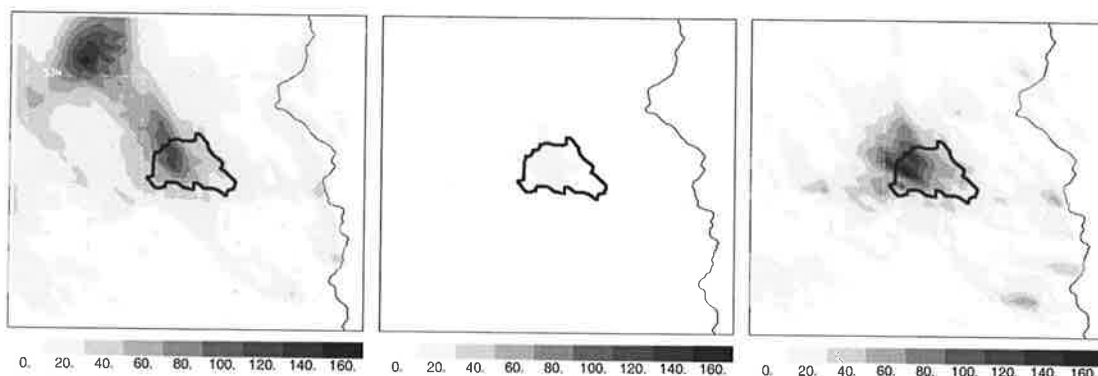
Figure 5.34: Anthropogenic VOC concentrations in ppb$_v$C at 5 UTC (left panel), 14 UTC (middle panel) and 21 UTC (right panel), on July 23.

underestimation of ozone in the southern part of the domain compared to the aircraft and surface measurements (section 5.4.2). The lack of surface monitoring stations in the south-western area of the domain is of great disadvantage in this case.

This theoretical study is carried out to analyse and explain the general underprediction of ozone. It can be summarized that ozone formation in Berlin-Brandenburg is VOC-sensitive. The major part of the VOC which are emitted in the domain is of biogenic origin. Therefore it is assumed that emissions of biogenical hydrocarbons, e.g. isoprene and monoterpene, are underestimated. This study shows the great importance of biogenic VOC measurements when analysing ozone formation. Unfortunately no useful VOC measurements exist for this period. Therefore all assumptions made in this section have to be regarded as scientific hypotheses. Their validity can only be established by comparison with direct measurements.

5.5   Tuesday July 26, 1994

5.5.1   Comparison of Horizontal Distributions

Tuesday, July 26, belongs to the *episode II* category. The atmosphere over Berlin-Brandenburg is more highly polluted than during *episode I* as discussed in section 5.2. The analysis of this particular day will start with a comparison of measured NO_2 and ozone surface concentrations. Fig. 5.35 presents near surface concentrations of NO_2 at three different times on July 26. The observed and the simulated concentrations show the same features: in the morning maximum concentrations close and downwind of the main emission sources, very small concentrations during the day, and increasing concentrations close to the city and the motorways in the evening. During the morning of the 26th enhanced NO_2 concentrations are found west of Berlin. These high concentrations are emitted in the city of Berlin, accumulated over night and transported during the early morning hours to the west. VOC concentrations shown in Figure 5.36 detail horizontal distributions of the other ozone precursors during that morning. The high VOC concentrations in the southern and western parts of the domain result from the mixing of freshly emitted and accumulated anthropogenic and biogenic VOC's. Altogether, a high level of ozone
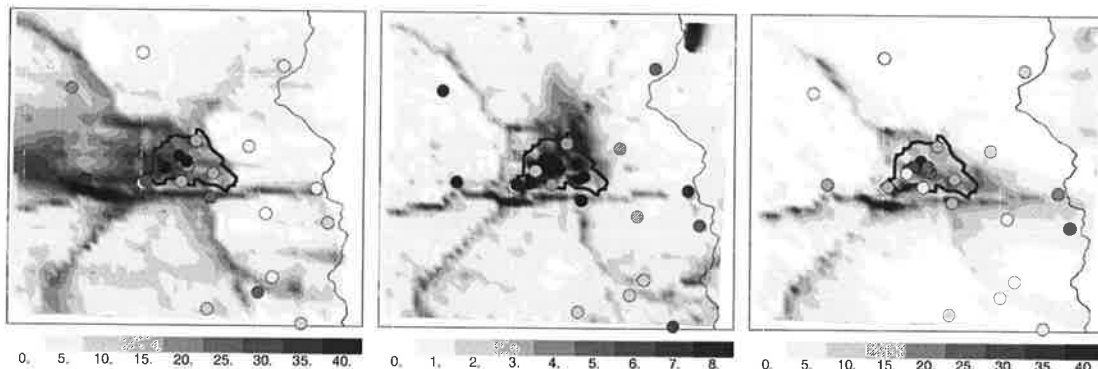
Figure 5.35: Observed (filled circles) and modelled near surface NO_2 concentrations in ppb$_v$ at 5 UTC (left panel), 14 UTC (middle) and 21 UTC (right), on July 26. Different colorbars are used.
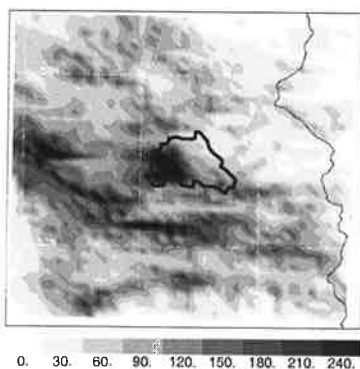
Figure 5.36: Near surface VOC concentrations in ppb$_v$C at 5 UTC, on July 26.

precursors exits in the morning in west Berlin. The diurnal development of modelled and observed near surface ozone concentrations is presented in Fig. 5.37-5.39. During that day the distributions of the pollutants is strongly influenced by the changing wind direction which occurred during that day. The predominant wind direction is easterly during the night. In the morning at 5 UTC (Fig. 5.37 (left panel)) ozone is completely destroyed close to and downwind of Berlin and the motorways. Again, the amount of advected ozone across the lateral inflow boundaries is overestimated. The modelled and the observed concentrations show quite similar results, excluding the east of the domain where ozone is underpredicted. Three hours later (Fig. 5.37 (right panel)) strong local gradients in ozone concentrations have developed. The
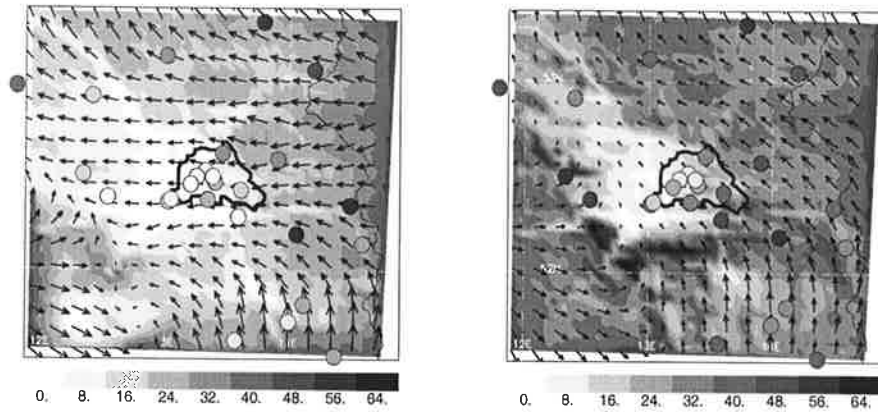
Figure 5.37: Ozone surface concentrations in ppb$_v$ and wind directions at 5 UTC (left panel) and 8 UTC (right panel) on July 26. Observations are overlayed by the filled circles. The colorbars differ between these and the following figures.
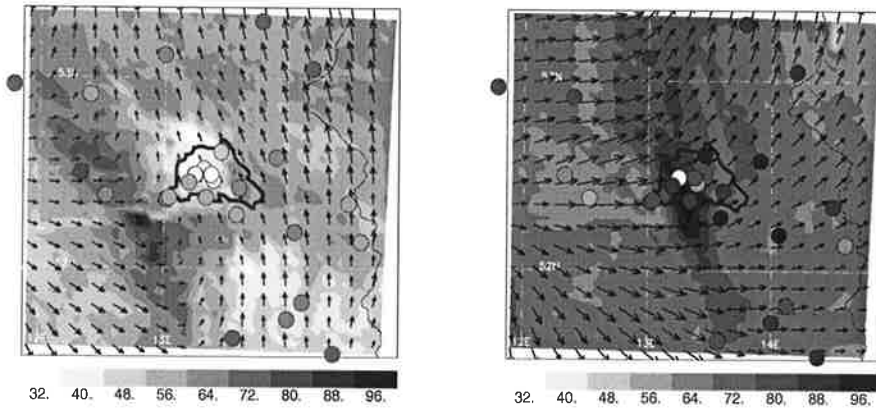
Figure 5.38: As Fig. 5.37 but at 10 UTC (left panel) and 14 UTC (right panel).
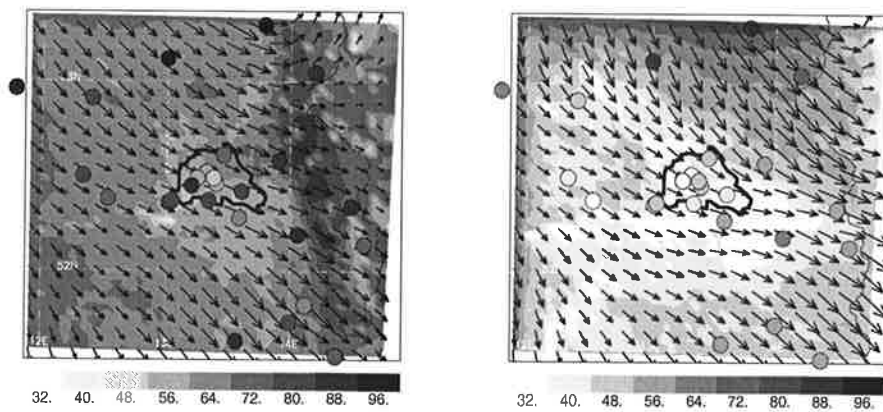
Figure 5.39: As Fig. 5.37 but at 18 UTC (left panel) and 21 UTC (right panel).

southerly component of the wind direction increases in the eastern part of the domain, while in the western part the wind comes from the western direction. In between this convergence zone high concentrations of ozone precursor occur initializing high ozone concentrations. A narrow band of high ozone concentrations is formed which is advected across Berlin during that day. At 10 UTC (Fig. 5.38 (left panel), notice changed colorbars) this band of enhanced ozone concentrations had strengthened. At 14 UTC ozone concentrations above 100 ppb$_v$ are reached and the ozone band crosses Berlin. Furthermore, the southerly wind has strengthened. At 18 UTC (Fig. 5.39 (left panel)) the ozone band reaches the Polish border and in the city ozone depletion due to NO titration starts. In the evening the wind turns to a north-westerly direction and while the ozone urban depletion is progressing ozone enriched air is advected across the northern lateral boundary into the model domain. This evening ozone flux is observed in the measurements. It is difficult to judge how well the simulation and observation compare because the structure of the ozone distribution is extremely complex during this day. The evolution of an ozone band is not explicitly observed by the point measurements. The formation of the ozone band results from the precursor distributions and the complex wind structure during that day. Small fluctuations in emissions, wind direction and velocity or the distribution of the other pollutants lead to changes in the ozone distribution. However, the main features of observed near surface ozone distributions during this day are matched but ozone is underestimated in the rural environment especially in the afternoon hours.

5.5.2   Vertical Trace Gas Distributions on the 26th

The vertical ozone distributions along the 52.5°N latitude at 6 MEZ, 15 MEZ and 22 MEZ are presented in Fig. 5.40. During the night from the 25th to the 26th an ozone enriched residual layer develops at altitudes from 100 to 2000 m. Concentrations up to 90 ppb$_v$ are simulated. The ozone concentrations in the residual layer decreases in the morning hours (Fig. 5.40 (left panel)) because ozone poor air masses are advected from the east into the model domain. In the afternoon urban ozone with a mixing ratio exceeding 100 ppb$_v$ is mixed homogeneously through the entire planetary boundary layer. In the evening a vertical ozone gradient develops
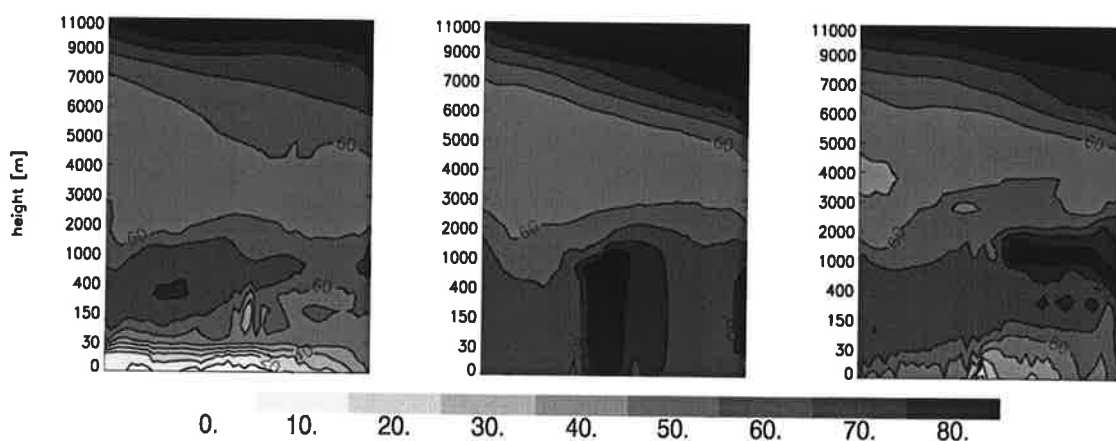
Figure 5.40: Vertical ozone distribution in ppb$_v$ at 52.5°N latitude at 6 MEZ (left panel), 15 MEZ (middle pane) and 22 MEZ (left panel) on July 26. The height niveaus are given in meters.

and an accumulation of ozone in the residual layer starts.

Aircraft observations cover times from 5.30 MEZ to 16.00 MEZ (Table 5.11). Simulated concentrations are interpolated in space and time to match the flight patterns as previously discussed in section 5.4.2. The measured concentrations are represented by the black dash dotted line. The grey solid line indicates the GESIMA simulations and the thin dashed line represents the concentrations as simulated by the REMO 1/6° model. The details of the individual flights together with a comparison of the measurements with the simulations are summarized in the following:

Table 5.11: Flight Times of MetAIR and ASK16 on July 26

5	6	7	8	9	10	11	12	13	14	15	16	17	18	19MEZ
				MetAir 1						M 2				
	ASK 1							ASK 2						

- ASK 1: This three hour long flight (Fig. 5.41) observed ozone concentrations increasing from 20 to 60 ppb$_v$ at 500 m. GESIMA maintained almost constant values around 70 ppb$_v$, which is an overestimation of observed ozone concentrations during this morning. The simulated ozone concentrations at 500 m altitude were still effected by the residual layer which had formed the night before.

- MetAIR 1: The flight took place before noon and lasted three and a half hours. The flight pattern in Fig. 5.42 shows that the aircraft circled twice around Berlin. The peaks of high NO_2 concentrations indicate the downwind directions of Berlin. GESIMA simulates peaks of high NO_2 concentrations as well, but some minutes before they were measured. This is an indication of deviations in the wind direction in the 500 m height level. Ozone is underpredicted by 20 to 30 ppb$_v$.

- ASK 2: This flight took place in the early afternoon hours. After Berlin was crossed at about 500 m altitude a vertical profile was flown in the west of the domain (Fig. 5.43). Above Berlin the observed and the simulated ozone concentrations are about 80 ppb$_v$. The vertical distribution between 500 and 3000 m height shows that ozone was well mixed up
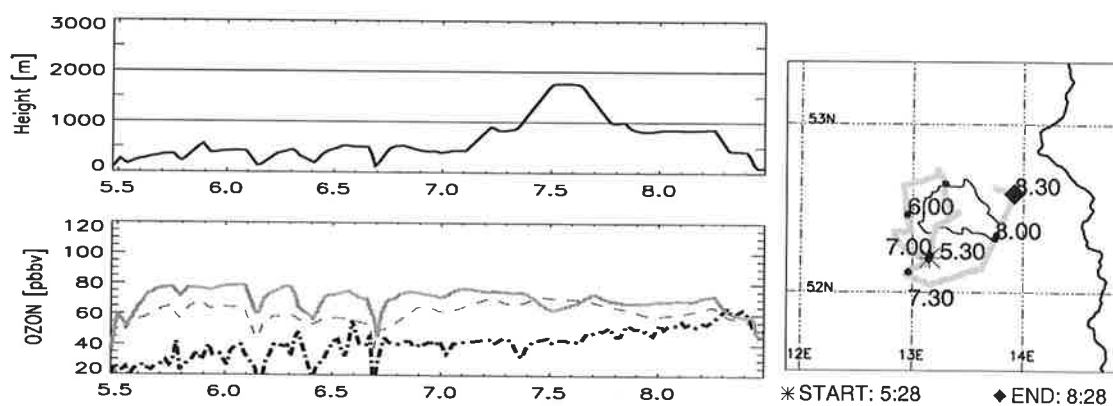
Figure 5.41: Flight ASK 1: Horizontal (right panel) and vertical (upper panel) flight pattern of flight ASK16 A on July 26. Time series of measured (black dash dotted line), GESIMA (grey solid line) and REMO (thin dashed line) modelled ozone concentrations (lower panel) in [ppb$_v$].

to 2000 m height and then decreased. GESIMA underpredicts ozone in this western part
of the domain between all levels from 1000 - 3000 m.

- MetAIR 2: This flight was rather short and Berlin was crossed at 500 m altitude
  (Fig. 5.44). Ozone and NO_2 is dramatically underpredicted by GESIMA.

The comparison between the aircraft observations and the GESIMA simulation shows much
poorer agreement compared to the results of July 23 as discussed in section 5.4. However, ozone
was already underestimated on the 23rd but on the 26th the underestimation increased. Also
deviations in the horizontal ozone distribution occur because of deviations in the wind direction.
The measurements at Turm Frohnau (Fig. 5.17) showed that there was a sudden jump in the
ozone concentrations from 60 to 90 ppb$_v$ at 324 m height around 12 UTC. This is an indication
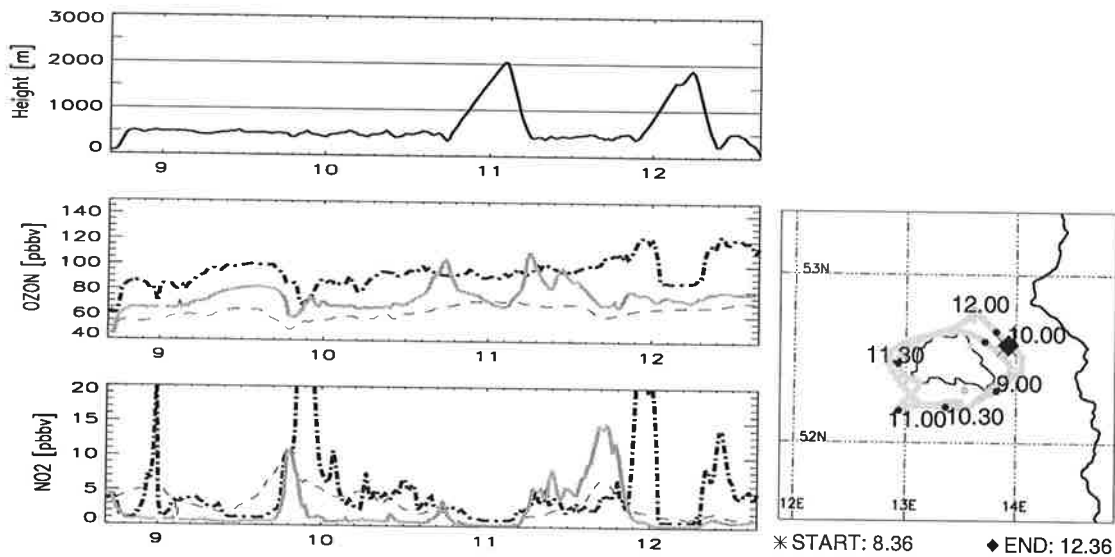
Figure 5.42: Flight MetAIR 1: Horizontal (right panel) and vertical (upper panel) flight pattern of flight
MetAIR A on July 26. Time series of measured (black dash dotted line), GESIMA (grey solid line)
and REMO (thin dashed line) modelled ozone (middle panel) and NO_2 (lower panel) concentrations in
[ppb$_v$].
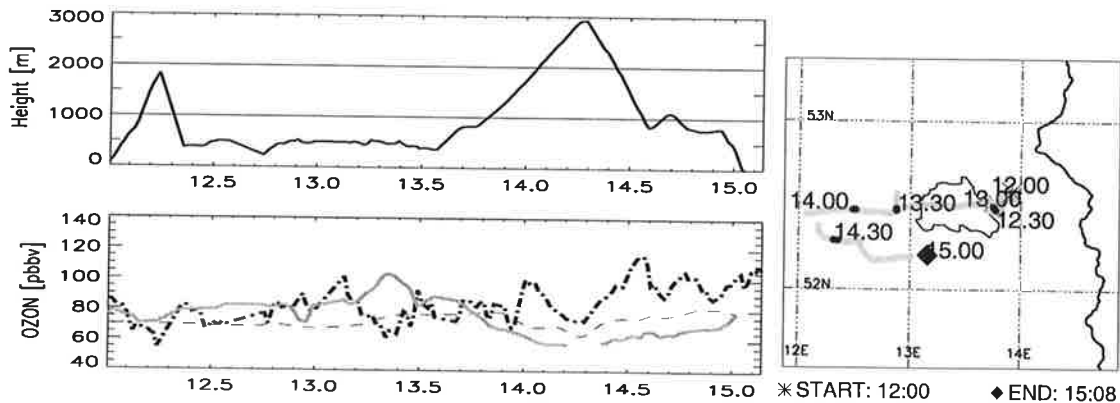
Figure 5.43: Flight ASK 2: As Fig. 5.41 but for flight ASK 16 B
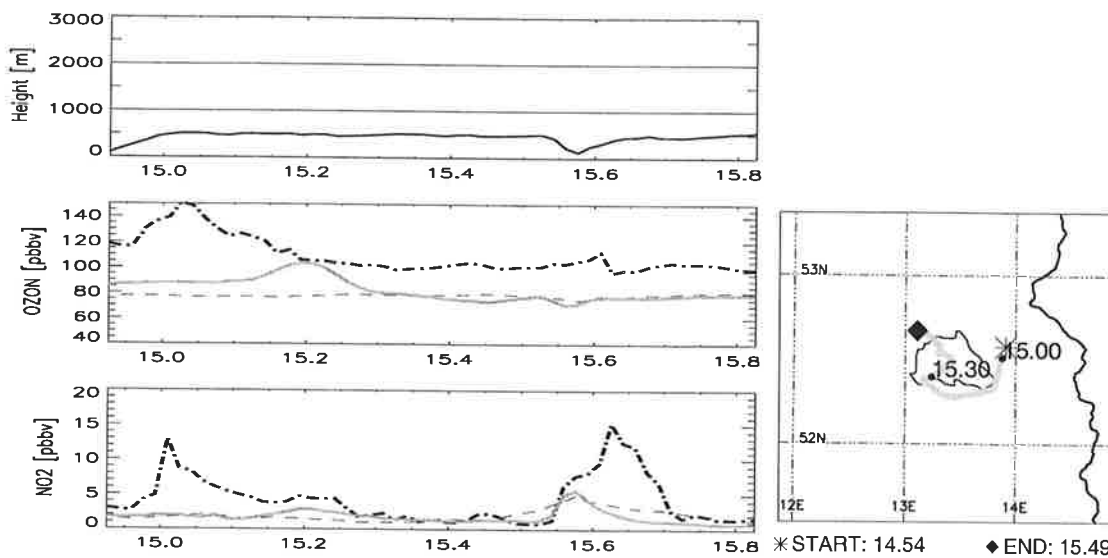
Figure 5.44: Flight MetAIR 2: As Fig. 5.42 but for flight MetAIR B

of changes in the background ozone and therefore that the characteristics of the advected air masses may have changed.

5.5.3   Characteristics of Air Masses

The amount of total NO_y in the troposphere is an important measure of the total oxidized nitrogen content and is closer to an conserved quantity than any of its constituents (*Roberts*, 1995). Reactive nitrogen, denoted NO_y, is defined as the sum of the two oxides of nitrogen, ($NO_x = NO + NO_2$) and all compounds that are products of the atmospheric oxidation of NO_x. These include in adaption to the RADMII scheme nitric acid (HNO_3), nitrous acid (HONO), the nitrate radical (NO_3), dinitrogen pentoxide (N_2O_5), peroxynitric acid (HNO_4), peroxyacetyl nitrate (PAN) and alkyl nitrates ($RONO_2$). In urban areas NO_x is the dominant constituent of NO_y, The ratio of NO_x to NO_y reflects the chemical processes which occur in an air mass after the initial introduction of NO_x. Thus, this quantity is indicative of the oxidation that has taken
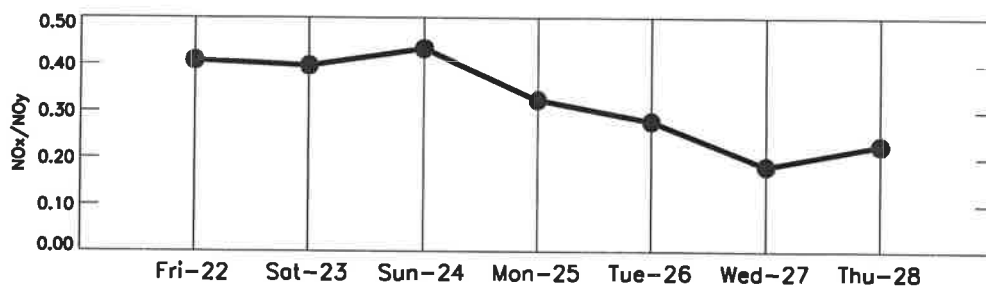
Figure 5.45: NO_x/NO_y ratio averaged over the lower 3000 m of the model domain for midnight at all days.

place in the air mass. Because NO_y enters the atmosphere as NO_x, the decrease in the ratio NO_x to NO_y can be understood in terms of the increasing chemical conversation of NO_x to organic nitrates (principally PAN) and to inorganic nitrates (principally HNO_3).

Figure 5.45 shows the NO_x/NO_y ratio for all simulated days at midnight as average over the lower 3000 m of the troposphere in the model domain. The concentrations at midnight are chosen because photolytical activity rests and the NO_x/NO_y ratio maximizes. The figure indicates that the NO_x/NO_y ratio decreases during the FLUMOB episode because NO_y increases from day to day while the NO_x concentrations remain more or less constant. The increasing NO_y concentration indicates the chemical aging of the air masses and the increasing air pollution during the FLUMOB episode. The weak increase in NO_x/NO_y ratio on the 28th indicates the end of this summer smog episode where cleaner air was advected to Germany by a passing frontal system. A number of studies have shown that ozone formation is correlated with the NO_y/NO_x ratio (*Trainer et al.*, 1991, 1993; *Kleinman et al.*, 1994).
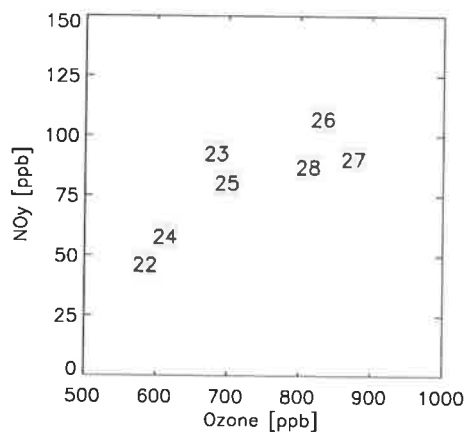
Figure 5.46: Correlation between ozone and NO_y, both in ppb$_v$ and as mean over the lower 3000 m of the model domain for midnight, all days.

Figure 5.46 shows the correlation between total ozone and NO_y in the lower troposphere (lowest 3000 m) in the GESIMA domain. The numbers in Fig. 5.46 denote the days in July 1994. Increasing ozone concentrations go ahead with increasing NO_y. On July 26 the NO_y concentrations is highest indicating aged polluted air masses reaching Berlin-Brandenburg. Therefore Tuesday the 26th was strongly influenced by the history of the aged air masses prevailing and reaching Brandenburg. This means, that on this particular day the quality of the GESIMA simulation depends on the quality of the simulation of the previous days and the quality of the coarser REMO simulation. Systematic model errors affect the quality of the simulation in a specific way on this day and thus also during *episode II*. However the quality of the REMO simulation is of great importance.

Figure 5.47 shows the near surface ozone concentrations and wind directions at 12 UTC on the 26th as simulated by the REMO 1/6° model run. Ozone polluted air masses with concentrations about 70 - 80 ppb$_v$ are advected from southern Germany to Brandenburg. These air masses are marked by the complete devolution of the summer smog event because they originate in polluted regions. But not primary the surface conditions influence the results of the GESIMA simulation. The conditions in the free troposphere are only observed by a ozone balloon sounding. The comparison of this single ozone profile, carried out on the 26th in Lindenberg at 16 UTC, to the ozone profiles as simulated by REMO 1/6° and GESIMA are presented in Fig. 5.46 (left panel). This comparison shows the dramatic underprediction of ozone by the REMO model in the entire troposphere. Close to the surface REMO shows ozone concentrations of a bout 80 ppb$_v$ and higher above roughly 50 ppb$_v$. The measurements show about 80 ppb$_v$ of ozone near the earth's surface and an increase up to 110 ppb$_v$ at 700 m altitude and above a mixing ratio of about 100 ppb$_v$. GESIMA improves the simulation in the lowest 500 m. In the upper half of the mixing layer the ozone concentrations starts to decline toward the REMO concentrations.
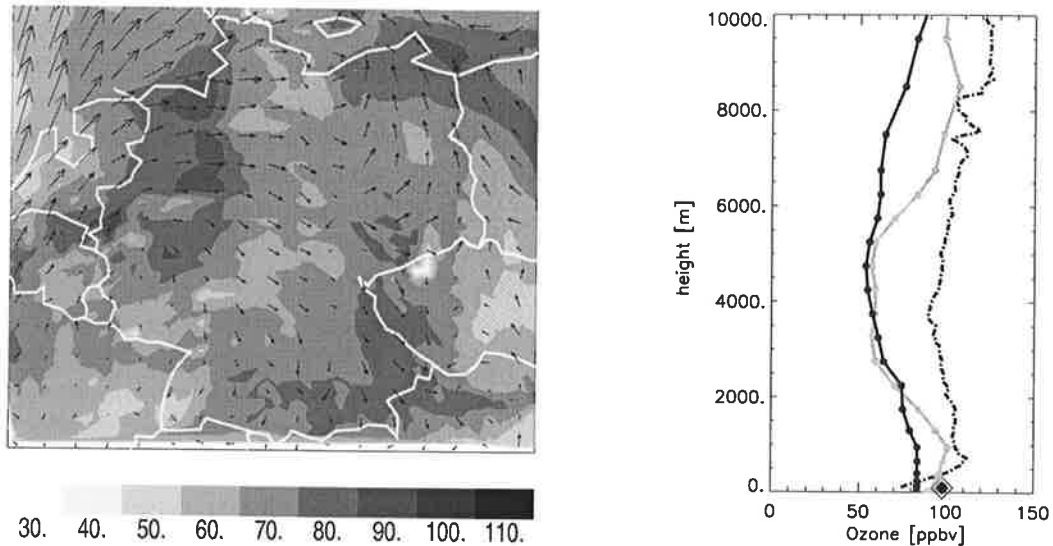
Figure 5.47: Surface ozone in ppb$_v$ and wind directions at 12 UTC on July 26 as modelled by the REMO 1/6° simulation (right panel). Vertical profiles of ozone mixing ratios in ppb$_v$ at Lindenberg (left panel). The measurements (black dashed line) are compared to the REMO (black line) and the GESIMA (grey line) profiles on Tuesday the 26th at 16 UTC.

This comparison shows the serious underprediction of ozone throughout the entire troposphere. This discrepancy needs further investigation and will be discussed in the next chapter where the history of ozone formation in the REMO model will be analysed and a sensitivity experiment will show how the GESIMA simulation is influenced by the ozone concentrations given at its lateral boundaries.

5.6 Discussion

In chapter 5 the observed and simulated ozone and NO_2 concentrations are evaluated. The most important results of this evaluation can be summarized as follows:

- The quantitative error analysis of the time series of near surface concentrations (section 5.2) shows that GESIMA simulates the photochemical situation with acceptable precision for the FLUMOB episode. The statistical analysis of surface data reveals that the model tends to underpredict ozone, but in general there was a high correlation between modelled and observed ozone.

- In particular, the comparison to urban stations shows the good performance of the model simulation. This is also an indication that the anthropogenic emission data sets are of high quality.

- The underprediction of surface ozone was especially pronounced in the rural environment. The character of the model domain as a whole can be classified as rural and the ozone formation regime was found to be VOC-sensitive. Therefore the underestimations of biogenic emissions is probably responsible for the underprediction of ozone.

- The FLUMOB period can roughly be divided in two episodes: During *episode I* Berlin-Brandenburg was influenced mainly by locally formed pollutants. Deviations between observed and modelled quantities have to be attributed mainly to improvements of the GESMIA model. *Episode II* was, in addition to local photochemical production, strongly influenced by advected pollutants (section 5.5.3) from outside of the domain. Therefore the boundary conditions have a large influence on the calculated trace gas concentration and their effects have to be included in the validation.

- The aircraft measurements demonstrate that especially during *episode II* ozone is dramatically underpredicted in the lower troposphere.

- The ozone balloon sounding showed that ozone is strongly underpredicted in the free troposphere by the REMO model and therefore by the GESIMA model as well.

In general, uncertainties of the model results are caused by several factors: meteorology, emission rates, chemistry and boundary conditions. Errors associated with meteorology, especially wind speed and direction, can lead to large underestimates or overestimates in trace species concentrations, with errors in the location of the ozone peak. This was, for example, demonstrated by the validation on Tuesday, July 26 where deviations of the location of the ozone peak were detected by aircraft measurements in the afternoon. The analysed high ozone event is associated with very low wind speeds. In this situation the uncertainty in wind speed has the same magnitude as the wind speed itself as demonstrated in section 4.3. This issue was also studied by *Kumar and Russell* (1996), *Sistla et al.* (1996) and *Al-Wali and Samson* (1996). Uncertainties in the boundary layer depth can also contribute to errors in the modelled ozone (*Marsik et al.*, 1995). Planetary boundary layer depth was observed by the meteorological balloon soundings and, as discussed in section 4.3, underestimated by GESIMA particularly during *episode I*. The large emissions arising from the urban core into the boundary layer and the daily mixing of the entire boundary layer have a high impact on the model's sensitivity to errors in the boundary layer calculation. Emission rates are probably the largest source of uncertainty. NO_x emissions are generally regarded as more accurate than VOC emissions (*Hassel et al.*, 1998). Since VOC emission controlled the ozone formation in Berlin Brandenburg during this distinct summer smog situation (section 5.4.3), measurements of VOCs are of great importance but, unfortunately, they have not been carried out during the FLUMOB field experiment. A large fraction of VOC in Germany is of biogenic origin and without measurements the biogenic emission model can not be evaluated. The chemistry mechanism itself is another source of uncertainty. The RADM II mechanism was analysed by *Gao et al.* (1996) and they found that uncertainties in reaction rates caused 20% uncertainty in calculated concentrations of ozone and of other species. Finally, meteorological and chemical information at the artificial lateral boundaries and the adopted initial conditions influence substantially the model results (*Brost*, 1988). A sensitivity study investigating the effects of lateral boundary conditions on the calculated ozone concentrations is presented in chapter 6.

6 Influence of Large Scale Conditions

6.1 Results of the REMO Simulation

The importance of trace species concentrations at the lateral boundaries of the GESIMA domain is analysed in this section. Especially longer living species like ozone are assumed to be sensitive to their horizontal and vertical distribution at the lateral boundaries (*Brost*, 1988). Tropospheric ozone has different life times in the planetary boundary layer and the free troposphere. In the planetary boundary layer ozone is transformed after some hours, in the free troposphere the life time of ozone is estimated to be roughly one week or even longer. During this time air masses can be advected over long distances. The vertical distribution of ozone is also of great importance. Most trace gas species show maximum concentrations close to the earth's
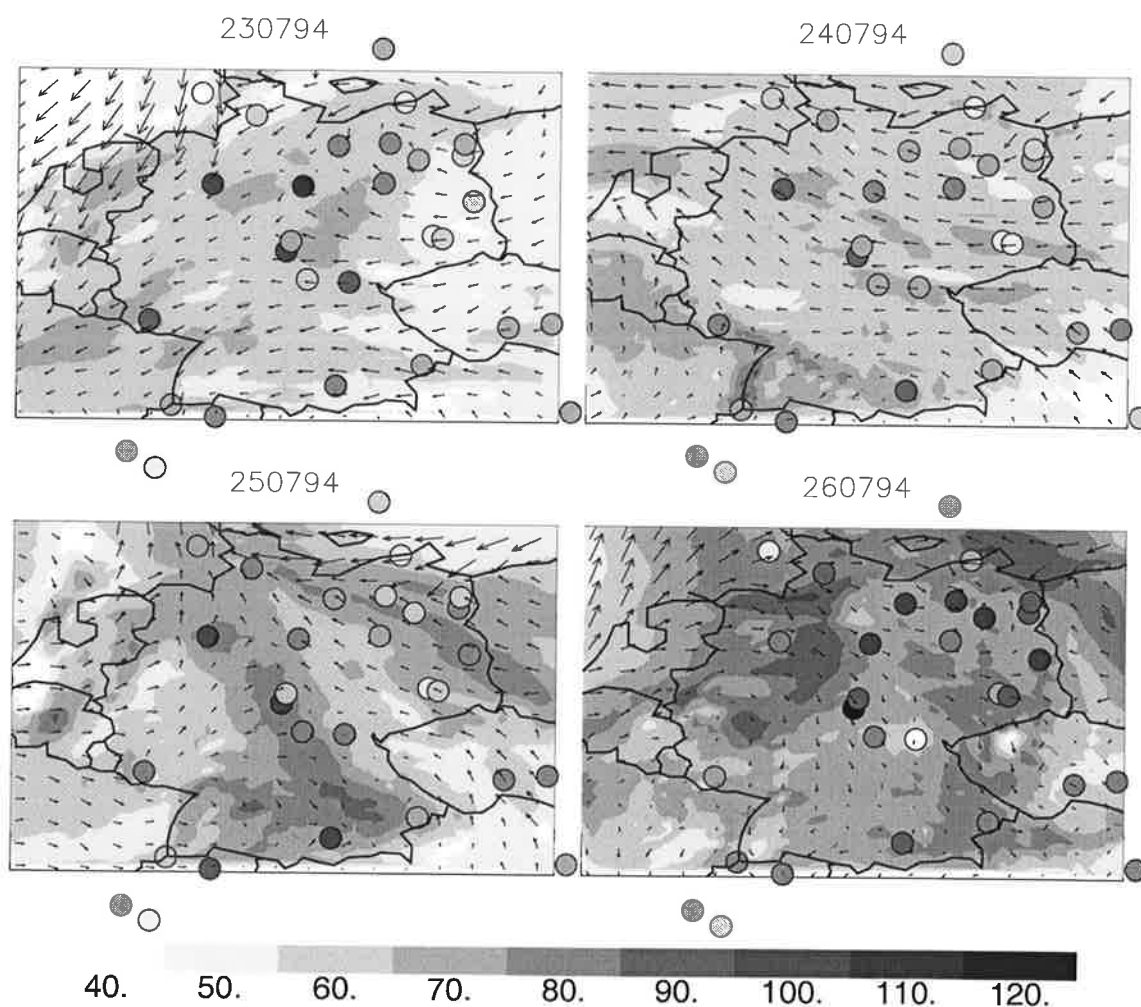
Figure 6.1: Near surface ozone concentrations in ppb$_v$ as simulated by the REMO 1/6° model for July 23 (upper left), 24 (upper right), 25 (lower left) and 26 (lower right panel) at 15 UTC, respectively. The circles show observations. The arrows indicate the wind direction at 10 m altitude.

surface and decrease rapidly with increasing height. Contrarily, ozone is present in the whole troposphere with relatively high mixing ratios and increasing concentrations with a maximum in the stratosphere at about 20-30 km height. Thus, the lifetime and distribution of ozone is also dependent on the larger scale conditions when investigating the processes of pollutant formation in Brandenburg.

Fig. 6.1 shows measured and modelled near surface ozone concentrations of the REMO 1/6° simulation at 15 UTC. During *episode I* (July 22 - 25) the air masses near the surface are advected mainly from the east to Germany and especially to Brandenburg. The near surface ozone concentrations increase from day to day. The comparison between simulated and observed concentrations reveals that during the first days, until the 24th, the observations show concentrations about 10 ppb$_v$ higher. On the 25th model simulation and observation show quite similar ozone concentrations, between 50 to 90 ppb$_v$, with some monitoring stations measuring mixing ratios of up to 100 ppb$_v$. Ozone is again underestimated by the REMO model on the 26th at some stations in Brandenburg by up to 40 ppb$_v$. The comparison made here is for afternoon concentrations at 15 UTC. At noon the model shows better reproduction of observed ozone concentrations. In the afternoon and evening hours ozone underprediction increases. Although ozone concentrations are slightly underpredicted the model performance is reasonable for the near surface concentrations.

Fig. 6.2 presents the simulated vertical ozone distribution along 52.22°N latitude on the 23rd and the 26th at 15 UTC. In the simulation ozone increases mostly in the planetary boundary layer, below 3000 m. In the free troposphere, between 3000 and 10000 m, ozone increases only slightly in the eastern model area and even decreases in the west.

On the 23rd, ozone poor air masses were advected from the east into the model domain, so that low ozone concentrations occur throughout the entire troposphere in the east of the domain.
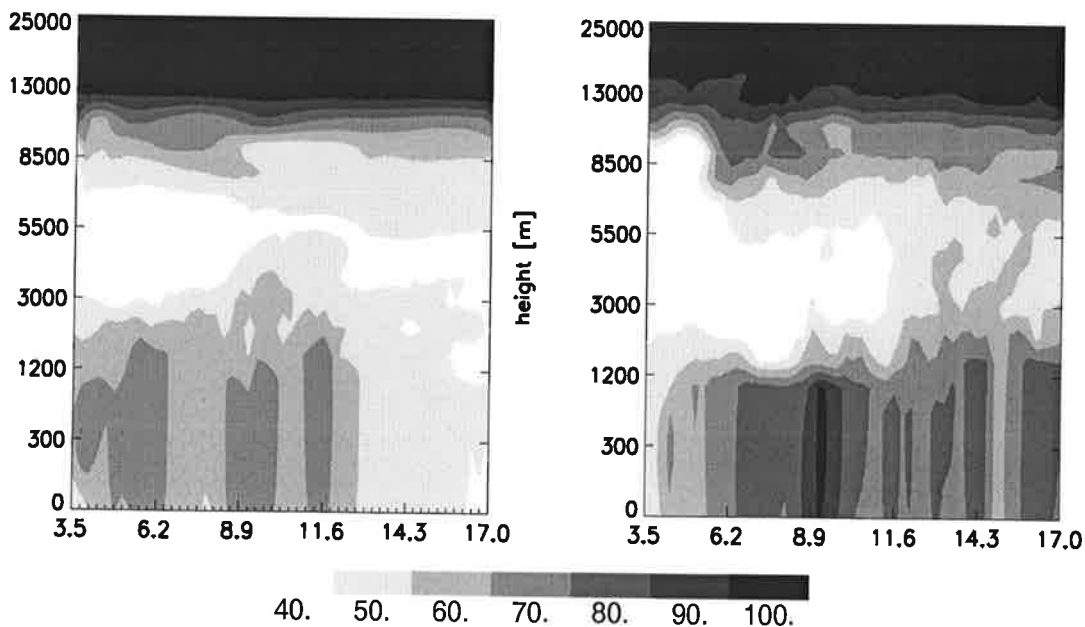
Figure 6.2: Vertical distribution of ozone along 52.22°N latitude at 15 UTC on July 23 (left panel) and July 26 (right panel). The numbers at the abscissa denote longitudes. The concentrations are shown in ppb$_v$.
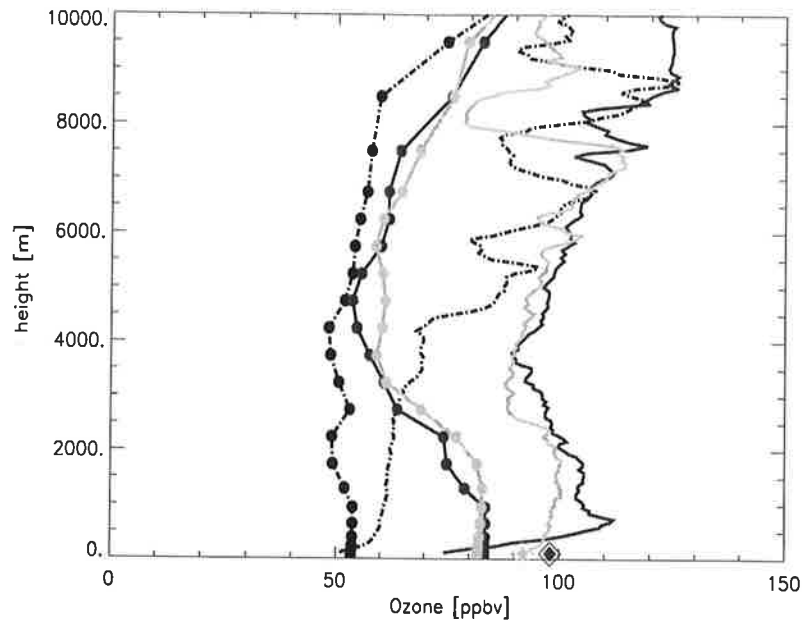
Figure 6.3: Vertical ozone profiles at station Lindenberg. The soundings are started at 16 UTC on July 23 (black dashed line) and July 26 (black solid line). On the 27th (grey line) the sonde is launched at 10 UTC. Ozone surface measurements are plotted as diamonds for the 26th (black) and the 27th (grey). The modelled concentrations are marked by solid circles. The concentrations are shown in ppb$_v$.

Towards the west ozone increases in the planetary boundary layer. The maximum ozone concentration at 6°E originates from the industrial area in the Netherlands. On the 26th, the maximum concentrations in the planetary boundary layer at 9°E originate from air masses which where advected during the day across the highly polluted regions of the Netherlands and the Rhine-Ruhr area. In the free troposphere ozone increases in the East by only 10 ppb$_v$.

Station Lindenberg is located at 52.22°N and 14.22°E. There, three ozone balloon soundings were carried out, on July 23 and 26 at 16 UTC and on July 27 at 10 UTC. The three measured profiles and the concentrations as simulated by the REMO 1/6° model are shown in Fig. 6.3. As has been discussed in the previous figure the modelled ozone concentrations only increase appreciably in the planetary boundary layer. In the free troposphere ozone increases by only 10 ppb$_v$. A different and quite unusual picture is presented by the observations. On the 23rd (Fig. 6.3 (black dashed line)) ozone reaches a mixing ratio of about 60 ppb$_v$ in the planetary boundary layer. However, this ozone does not seem to be primarily produced locally because on this day Lindenberg was situated upwind of Berlin.

To explain the observed high ozone concentrations in the free troposphere backward trajectories, calculated by the German Weather Service, are analysed. Backward trajectories give information about the pathway of air masses at different pressure levels. The trajectories for the air masses reaching Lindenberg on July 23 and July 26 are shown in Fig. 6.4 and Fig. 6.5.

On the 23rd the near surface air masses were advected from Scandinavia over Poland to Brandenburg. Along this trajectory the air masses are advected over large forested areas. The assumption (section 5.4.3) of an underestimation of biogenic emissions could explain the lack of ozone in the simulated lower troposphere. In the free troposphere the ozone balloon soundings (Fig. 6.3) measured ozone concentrations between 60 and 120 ppb$_v$ on the 23rd. The backward trajectories
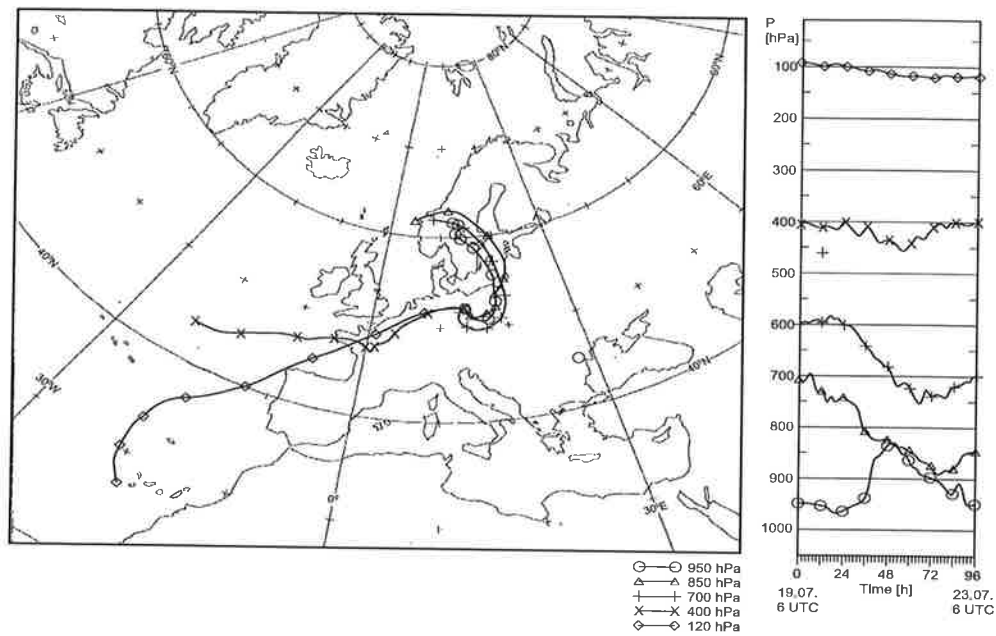
Figure 6.4: Backward trajectories calculated for air masses reaching Lindenberg on the 23rd.
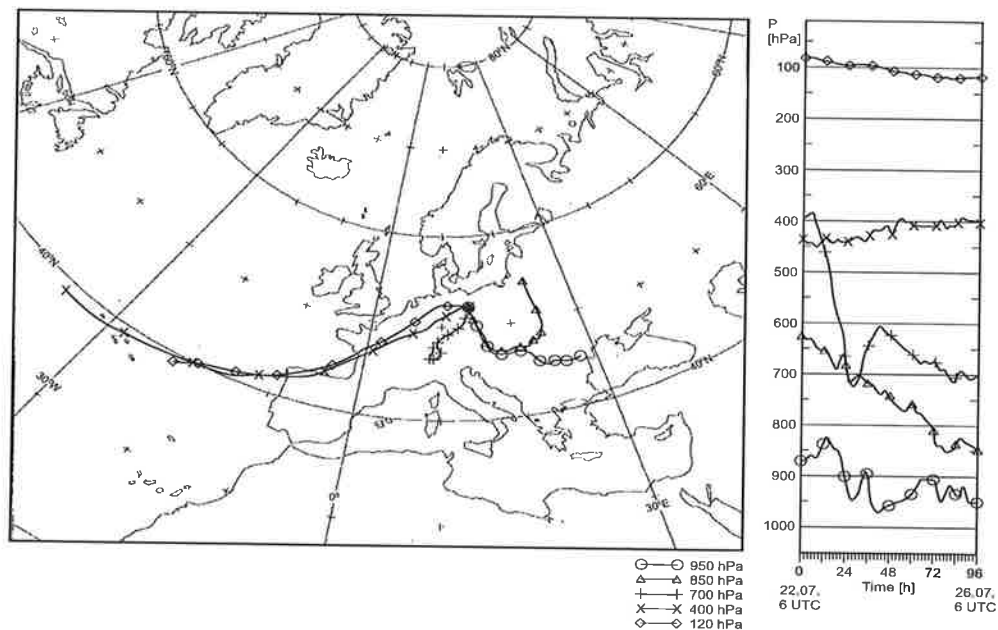
Figure 6.5: Backward trajectories calculated for air masses reaching Lindenberg on the 26th.

from the 23rd show that at higher levels the air masses may originate from the Atlantic ocean four days prior to their arrival in Lindenberg.

The measured profiles on the 26th and 27th show quite similar vertical distributions of ozone in the free troposphere. The differences in the planetary boundary layer are attributed mainly to the difference in the time of day. On the 26th the sounding is started at 16 UTC and shows

the daily maximum concentrations in the planetary boundary layer, whereas on the 27th the sonde is started at 10 UTC where the daily ozone formation is still in progress. Ozone surface measurements at station Lindenberg are plotted as diamonds in Fig. 6.4 for the 26th and 27th. On the 27th (grey line and diamond) the radio sonde measurement and the surface observation show similar concentrations but on the 26th (black line and diamond) the surface near ozone sounding and the surface measurement differ strongly, so that the steep ozone gradient measured below 700 m height by the radio sonde is not reliable. On the 26th and 27th, the vertical ozone distribution in the free troposphere shows a rather uniform vertical structure with ozone concentrations between 90 and 110 ppb_v. These high ozone concentrations in the lower troposphere are assumed to originate from European production. In the afternoon of the 26th the ozone in the lower boundary layer originates partly from local production, because during that afternoon Lindenberg is situated downwind from Berlin and, furthermore, the near surface ozone distribution is well simulated by the GESIMA run (Fig. 5.47). Apart from this local production, which is on a subgrid scale for the REMO simulation, there is still a lack of about 30 ppb_v of ozone in the planetary boundary layer. The backward trajectories calculated for the 26th show that at about 700 hPa air masses from south-west Germany are advected to Lindenberg. Following that trajectory the air masses pass highly polluted areas and ozone could have accumulated day by day in the lower troposphere. In the simulation ozone was also accumulated in the lower troposphere. Ozone increased from 50 to 80 ppb_v between the 23rd and the 26th. The total increase of ozone in the planetary boundary layer was only underestimated by 10 ppb_v. Above the planetary boundary layer the homogeneous vertical distribution of the observed ozone concentrations indicate that ozone is well mixed throughout the troposphere. It is assumed that the observed unusually high mixing ratios of about 100 ppb_v is the result of mixing of long range transported upper level ozone and upward transported ozone from the planetary boundary layer, formed and accumulated during the summer smog event.

Because of the lack of measurements it is difficult to evaluate the assumption that during this summer smog event Europe was additionally influenced by high amounts of long range transported ozone. However, it seems to be the most probable explanation for the large amounts of ozone in the free troposphere, especially during the 23rd. Other ozone balloon soundings, Brussels and Hohenpeißenberg, support this theory. The shape of the European wide ozone soundings exclude also stratospheric ozone intrusion (*Krüger* (2000)).

At the lateral inflow boundaries of the coarsest REMO simulation constant climatological conditions are assumed for the transported chemical species. For ozone a concentration of about 50 ppb_v is assumed in the free troposphere, increasing up to 100 ppb_v towards the tropopause. Fig. 6.2 and Fig. 6.3 demonstrate that these concentrations stay more or less constant during the simulation in the free troposphere. The analysis of the REMO simulation can be summarized in two points:

- The near surface ozone concentrations are slightly underpredicted especially in the afternoon hours. This underestimation may also be caused by an underestimation of the biogenic emissions as analysed by the GESIMA simulation. This finding is supported by a sensitivity study, carried out with the REMO model, were increased biogenic emissions result in an overall increase in near surface ozone concentrations. Additionally it should be noted that the REMO domains include some countries which deliver incomplete emission factors so that uncertainty in European wide anthropogenic emission inventories increase.

- Ozone is underestimated up to 50 ppb$_v$ in the free troposphere. This problem can only be solved with more frequent observations of the three dimensional structure of the chemical state of the atmosphere. This information is not only important as lateral boundary condition but also for model initialization.

The importance and the influence of the vertical ozone distribution in the GESIMA simulation will be studied in the sensitivity experiment which is described in the following section.

6.2   Sensitivity Experiment

The comparison of ozone profiles, as observed by radio sondes and as simulated by the REMO model, point out great discrepancies in the total amount and the vertical distribution of ozone. The way in which GESIMA is influenced by this poor lateral boundary information is investigated by a simple sensitivity experiment. Tuesday the 26th is chosen for the sensitivity study for several reasons: (1) On this day an ozone radio sonde measurement is available. (2) REMO strongly differs from the observations. (3) The GESIMA simulation delivers rather poor results compared to aircraft measurements as discussed in section 5.5.2.

To simplify the interpretation of the sensitivity experiment a time constant amount of ozone is added to the vertical ozone distributions of the REMO simulation. In the lowest three levels no ozone is added. Between 180 and 500 m the ozone profile increases up to a concentration of 40 ppb$_v$. This concentration remains constant between 500 m and the model top layer during the whole day. GESIMA was started on July 26 at 0 UTC with the meteorological and chemical restart files of the previous discussed GESIMA standard simulation. Additionally to these initial conditions the additional ozone profile was added to the three dimensional ozone concentrations. During the 24 hour simulation the increased ozone is added only at the lateral inflow boundaries. All other transported trace gas species interpolated to the boundaries of GESIMA remain unchanged compared to the standard experiment. The additional ozone amount of 40 ppb$_v$ roughly fills the ozone gap in the free troposphere (Fig. 6.3) but possibly overestimates the lacking ozone in the planetary boundary layer. However, since no further information about the vertical distribution of ozone and its daily cycle exists it is important to keep the structure of the sensitivity experiment simple.

6.2.1   Results of the Sensitivity Experiment

The problem of reduced ozone in the simulated free troposphere was detected by a single radio sonde in the GESIMA domain. Fig. 6.6 shows this measurement together with the REMO profile, and the result of the GESIMA standard and the sensitivity experiment. The sensitivity run shows that the additional ozone given to the lateral boundaries reaches Lindenberg in the free troposphere between 2000 - 6000 m more or less undisturbed. In this altitude region the REMO and GESIMA standard simulation differ only slightly. Ozone concentrations in this altitude region depend mainly on the horizontal advection and in case of GESIMA on the lateral inflow boundary concentrations. Above 6000 m GESIMA is influenced by the ozone concentrations given at the top boundary due to subsidence processes. Compared to the standard experiment
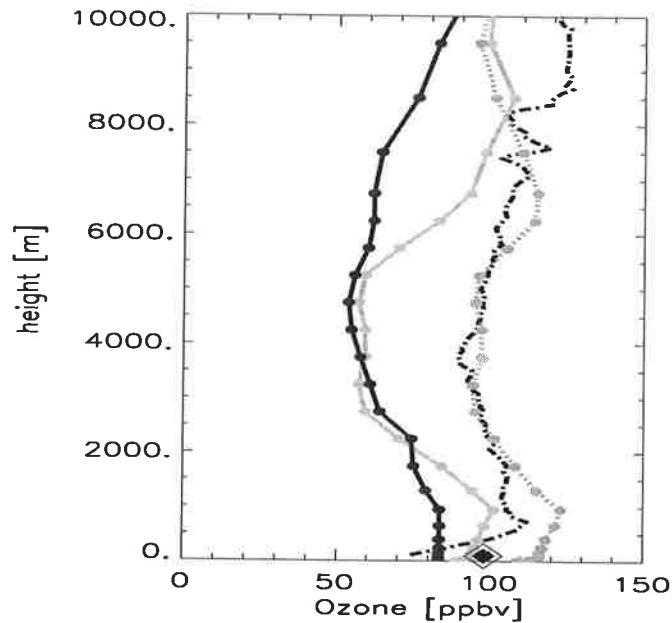
Figure 6.6: Vertical ozone profiles at station Lindenberg on July 26. The observations (black dashed line) and the surface measurement (black diamond) are shown together with the REMO simulation (black solid line), the GESIMA standard simulation (grey solid line) and the GESIMA sensitivity experiment (grey dashed line). The modelled concentrations are marked by circles. The concentrations are shown in ppb_v.

the ozone concentrations at the top boundary remain unchanged so that towards the model top layer the results of the GESIMA standard and sensitivity run converge. Between the earth's surface and 2000 m height the sensitivity run shows an ozone increase of about 20 ppb_v, but the vertical gradient is retained. The near surface measurement (Fig.6.6, black diamond) shows that the standard experiment reproduces the near surface concentration whereas the sensitivity experiment leads to an overestimation.

The time dependent changes between the sensitivity and standard experiment close to the earth's surface for an urban and an rural station are presented in Fig.6.7. At the urban station Berlin-
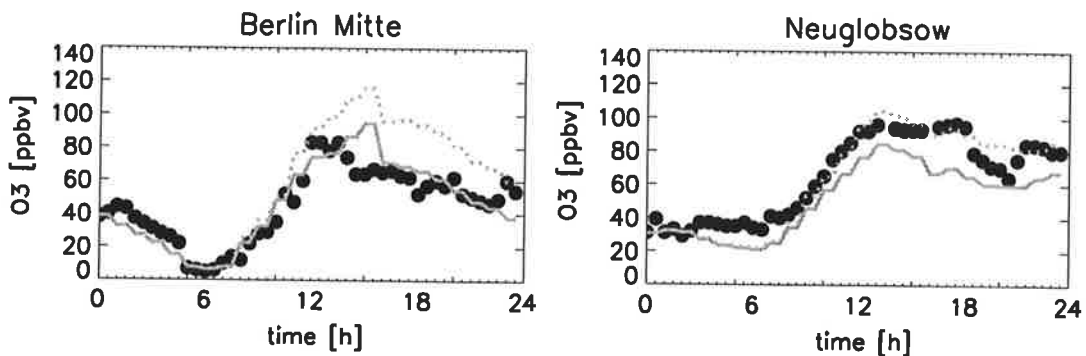
Figure 6.7: Measured (black circles) and the standard (solid line) and sensitivity (dotted line) experiment simulated near surface ozone concentrations at station Berlin-Mitte (left panel) and Neuglobsow (right panel). The concentrations are shown in ppb_v.

Mitte differences between the ozone concentrations as simulated by the standard and sensitivity run occur after 11 UTC. At that time convective vertical mixing leads to downward transport of ozone. Ozone concentrations increase about 20 ppb_v in the sensitivity experiment. At station Berlin-Mitte ozone is overpredicted in the sensitivity experiment during the second part of the day. This result is representative for all urban stations, where ozone was already reproduced with high accuracy by the standard experiment (section 5.2). Also at the rural station Neuglobsow an ozone increase of about 20 ppb_v is visible during the second part of the day. Here, the ozone simulation of the sensitivity run better represents the measurements. However, it is most likely that the near surface ozone concentrations in the rural environment are underpredicted
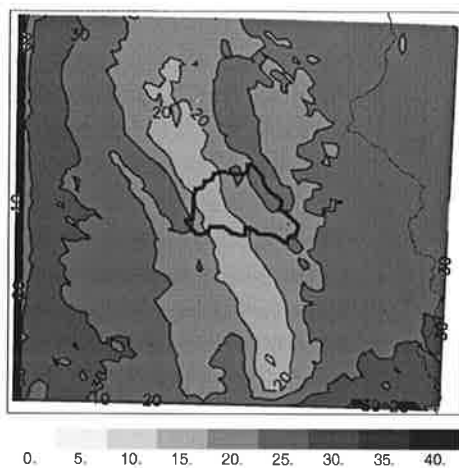
Figure 6.8: Difference in surface ozone concentrations (sensitivity - standard) at 14 UTC on July 26. The concentrations are shown in ppb_v.

by the standard experiment due to the underestimation of biogenic VOC emissions as discussed in section 5.4.3. Therefore, the sensitivity run shows better results but partly for the wrong reasons.

The influence on the surface concentrations is presented in Fig. 6.8 where the differences between the surface ozone concentrations (sensitivity - standard) are shown at 14 UTC. This picture can be compared to Fig. 5.38 (right panel) where the surface ozone concentrations at 14 UTC as simulated by the standard experiment are shown. The sensitivity run shows an increase of surface ozone in the whole model domain. The additional ozone originates at higher levels and is transported downward by vertical mixing. Fig. 5.38 shows a band of high surface ozone concentrations. In this region, where ozone has it's local maximum, ozone increases less in the sensitivity experiment, only by about 15 ppb_v. The pollutant precursors, the NO_x and VOC species, decrease by about 10% in the sensitivity run. However, besides ozone, only H_2O_2, hydrogen peroxide, and some organic peroxide species show a significant increase during day time. This leads to the assumption that in the polluted air masses additional ozone increase the oxidizing capacity. Additional ozone leads to enhanced photolytical production of OH-radicals which in turn increase the oxidation of the ozone precursors. The strong increase of H_2O_2 indicates the enhancement of the catalytic cycle. The H_2O_2 level depends on whether the atmosphere is in a high or a low NO_x regime. Because of unchanged emissions and enhanced oxidation the catalytic cycle is interrupted by the unavailability of NO. More radicals are formed that can react with NO_x and the excess radicals are removed by radical - radical reactions that are a source for peroxide. For example:

$$HO_2 \cdot + HO_2 \cdot \longrightarrow H_2O_2 + O_2 \tag{6.1}$$

Therefore, the local ozone production is not enhanced in the sensitivity experiment.

The influence of the sensitivity experiment on the ozone concentrations above the surface layer but still within the planetary boundary layer is demonstrated by the following two comparisons:
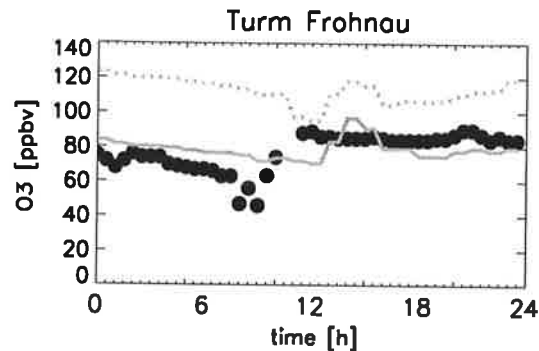
Figure 6.9: Measured (black circles) and the standard (solid line) and sensitivity (dotted line) experiment simulated near surface ozone concentrations in ppb$_v$ at Turm Frohnau in 324 m altitude.
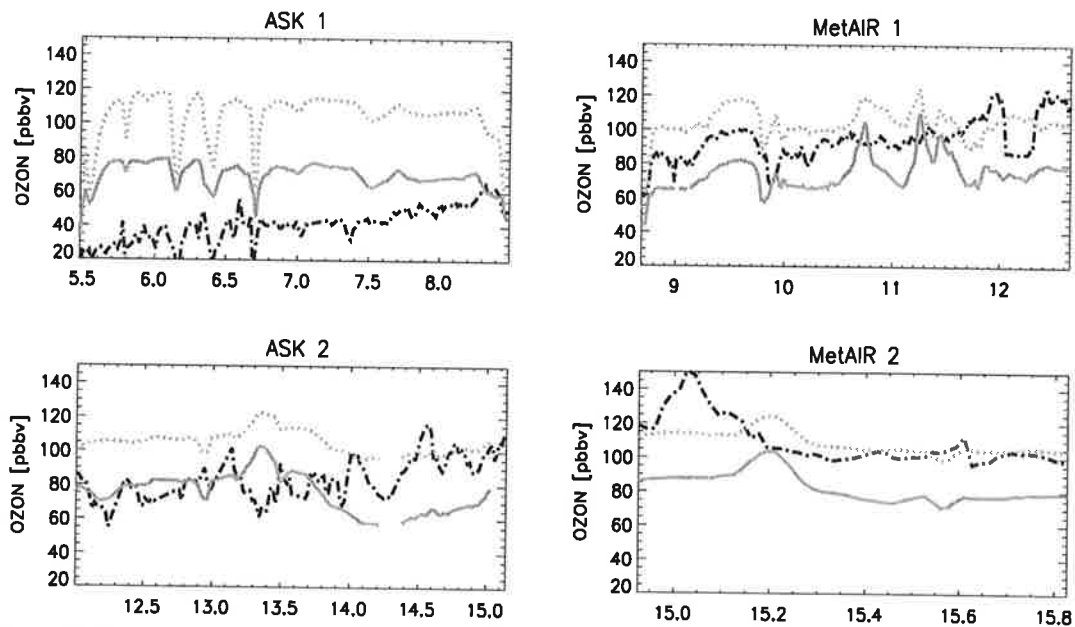
Figure 6.10: Ozone concentration in ppb$_v$ as measured by aircraft (black dashed line), and simulated by the standard (grey solid line) and sensitivity experiments (grey dotted line), for the four flights on July 26.

Turm Frohnau provides measurements at 324 m height above the surface (Fig. 6.9). The sensitivity experiment shows roughly 40 ppb$_v$ more ozone compared to the standard experiment. The standard run captures the observed ozone concentrations already quite well and the sensitivity overestimates ozone at 324 m height. Again this supports the statement that the amount of urban ozone is well simulated by the standard experiment in the lowest 300 m of the troposphere. Figure 6.10 presents the ozone concentrations in comparison with the aircraft measurements. The aircraft measurements are taken mostly at 500 m height together with some vertical soundings as described in section 5.5.2. Again the sensitivity results show equal variability in space and time but ozone is increased by about 30 - 40 ppb$_v$ as added to the lateral inflow boundaries.

6.2.2   Discussion

The results of the sensitivity experiment can be summarized in the following points:

- In the free troposphere, the ozone concentrations are strongly linked to the ozone concentrations provided at the lateral model boundaries and it's initial conditions.

- Also in the planetary boundary layer ozone increases linearly by the amount of ozone which is added at the lateral inflow boundaries. This is demonstrated by the results at 500 and 300 m height.

- Close to the earth's surface, net ozone production is reduced due to changes in the oxidizing capacity of the polluted atmosphere.

The analysis of the FLUMOB episode shows, that even during a blocking high pressure situation, Germany and also Central Europe is influenced by longrange transported ozone. The sensitivity experiment demonstrates the importance of precise three-dimensional information of ozone at the lateral model boundaries. Model results in the free troposphere are strongly defined by the initial and the boundary concentrations. Due to vertical mixing they also influence surface concentrations. The validation of the model simulations, as discussed in the previous chapters, clearly shows that ozone is systematically underpredicted in both models. The few ozone radio sonde soundings observe increasing ozone concentrations in the entire troposphere during the FLUMOB episode. This accumulation of ozone is not covered by the models. As longer living trace species are well mixed in the troposphere the documented systematic underprediction of surface ozone must also be partially due to the underrepresentation of ozone in the whole troposphere which in turn is strongly correlated to the model's chemical boundary conditions. In this simulated episode even a European wide simulation, REMO $0.5°$, is insufficient to study a long living species like ozone, because its origin is beyond the scope of the model domain.
More vertical ozone observations, three-dimensional analysis or global chemistry simulations are necessary to overcome these discrepancies.

7 The Aerosol Experiment

During the FLUMOB episode, radiation flux measurements show differences in solar irradiance depending on whether the measurements are carried out in the upwind or in the downwind direction of Berlin. An example of measured global irradiation in the upwind and downwind direction of Berlin is presented in Fig. 7.1 for July 23, 1994. On this day, which has been discussed in detail in section 5.4, the atmospheric conditions lead to higher air pollution in the downwind than in the upwind direction of the city. Fig. 7.1 shows that the three stations, Neuglobsow, Kyritz, and Premnitz, located in the downwind position of Berlin on that particular day, measured up to 100 W/m^2 less radiation flux compared to stations located in the upwind position, Eisenhüttenstadt and Cottbus. During the FLUMOB episode global radiation decreased day by day. Certainly, this is also caused by the increasing absolute humidity during this period, but this effect may additionally be caused by accumulation of smog aerosol in the planetary boundary layer. Especially, on the 23rd with cloud-free weather conditions and the development of a city plume downwind of Berlin, the observed irradiance reduction is potentially caused by primary and secondary aerosols in the planetary boundary layer.

On hot days with smog in metropolitan areas the cloud-free sky shows a milky yellowish color, the result of scattering of solar radiation by particles. Generally, aerosols influence the solar radiation directly via scattering and absorption processes and indirectly by acting as cloud condensation nuclei. The indirect effect occurs only in the presence of clouds and therefore does not influence the radiation conditions during this cloud-free summer smog event. The direct aerosol effect can be observed visually as haze in the atmosphere. The result of the process of scattering of sunlight is an increase in the amount of light reflected by the planet and a decrease in the amount of solar radiation reaching the ground. The magnitude of the direct forcing of aerosols depends on the size and optical properties of the particles, their abundance, the relative humidity, the solar zenith angle, and the albedo of the underlying surface. Urban aerosols are mixtures of primary particulate emissions and secondary material formed by gas to particle conversion. During smog conditions they turbidy the atmosphere inside the planetary boundary layer.
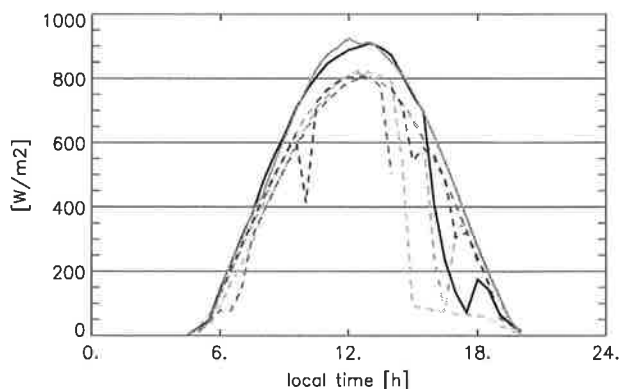
Figure 7.1: Comparison of measured global irradiation [W/m^2] at different stations in the upwind (full line) and downwind (dashed lines) direction of Berlin on July 23, 1994.

The following study was motivated by the radiation measurements in Berlin-Brandenburg. Many studies have provided evidence for this effect, especially since the 1970s when air pollution began to gain relevance (*Oke*, 1976). Measurements in 1973 and 1987 showed that downward UV irradiance within the planetary boundary layer in the California Basin were up to 50% less than those above the boundary layer due to smog effects (*Jacobsen*, 1999) within the planetary boundary layer. Compared to smog free regions total solar irradiance was reduced by 14%. Longterm observations in Mexico D.F. -the largest and most polluted urbanization in the world- show up to 250 W/m^2 reduction in global radiation (*Jáuregui and Luyando*, 1999), more than 20% of the incoming solar energy.

7.1 The Radiation Model

GESIMA includes a rather complex line-by-line radiation transfer model (*Schmetz and Raschke*, 1979; *Schmetz*, 1984; *Beniston and Schmetz*, 1985; *Schmetz and Beniston*, 1986; *Rockel et al.*, 1991). In the solar range it resolves 37 spectral bands and 51 bands in the terrestrial range. The radiation module is described briefly in section 2.2. Aerosols influence the radiation scheme only in the solar spectrum via the following parameters in Equ. 2.2: $\tilde{\omega}$, the single scattering albedo, δ, the vertical optical depth, and β, the fraction of backward scattering.

The single scattering albedo, $\tilde{\omega}$, describes the fraction of energy removed from the incident wave which reappears as scattered radiation. A perfectly absorbing aerosol has a single scattering albedo equal to zero. A single scattering albedo equal to 1 describes a completely scattering aerosol. Fig. 7.2 (left panel) shows the dependence of $\tilde{\omega}$ on wavelength as assumed for aerosols in the GESIMA model. At all wavelengths below 2.5 μm scattering dominates clearly over absorption.

The asymmetry factor describes the preferred direction of the scattered radiation. The backward scattering, $\beta(\lambda)$, is derived from the asymmetry factor. A positive asymmetry factor is assumed in the GESIMA model (Fig. 7.2, middle panel). Therefore, aerosol particles scatter preferentially
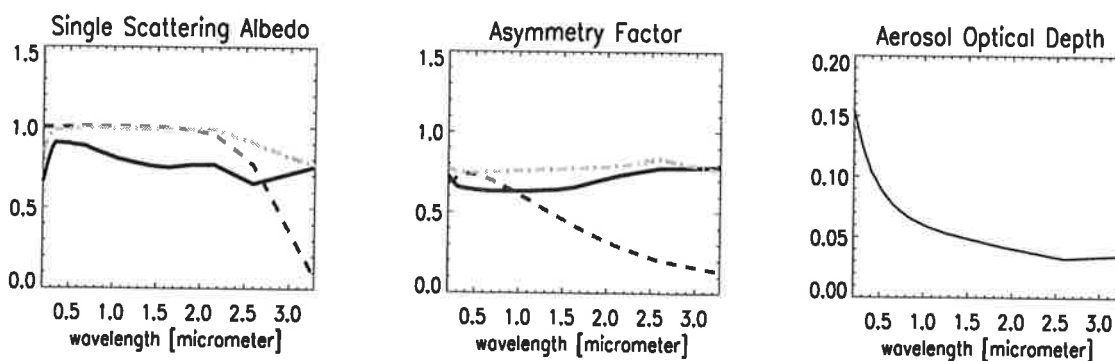
Figure 7.2: Wavelength dependent single scattering albedo (left panel), asymmetry factor (middle panel) and aerosol optical depth (right panel) as assumed in the GESIMA radiation model. The conditions in the upper (dashed dotted line), middle (solid line), and lower (dashed line) atmosphere are shown.

in the forward direction.

The vertical optical depth describes the light extinction due to aerosols along a vertical path through the atmosphere. Figure 7.2 (right panel) shows the wavelength dependence of aerosol optical depth as assumed in the GESIMA radiation model. The optical depth decreases rapidly as λ increases. As a result aerosols influence radiation mainly in the solar region of the spectrum.

7.2   Modification of Optical Properties

The above described optical properties of aerosols characterize typical continental background aerosol conditions (*d'Almeida et al.*, 1991). To investigate the influence of smog aerosols on meteorological parameters the radiative properties need to be changed to represent higher polluted urban conditions. Because no ambient aerosol measurements have been carried out during the FLUMOB experiment, values from literature (*d'Almeida et al.* (1991), *Kondratyev* (1969), *Kaufmann and Fraser* (1983), *Radinov et al.* (1999), *O'Neill et al.* (1993), *Jacovides et al.* (1999), *Horvath* (1996), *Matthias* (2000b)) are used to characterize smog conditions. The literature study shows that the representations of the single scattering albedo and the asymmetry factor can remain unchanged since the chemical composition and the size distribution of urban aerosols still leads to a domination of the scattering properties. This assumption is not valid unrestictely if high soot concentrations are included in the urban aerosol mix because soot also influence the single scattering albedo. However, in contrast to the background conditions, extinction is enhanced in the polluted urban atmosphere. Aerosols in the polluted atmosphere are characterized by higher values of the aerosol optical depth.

The values of aerosol optical depth and vertical distribution, which are based on literature data to represent urban smog aerosols, are shown in Fig. 7.3. The vertical distribution shows that the aerosols are mainly present in the planetary boundary layer. The optical thickness reaches unity close to a wavelength of 0.5 μm and is therefore considerably higher compared to the background aerosol condition (Fig. 7.2).
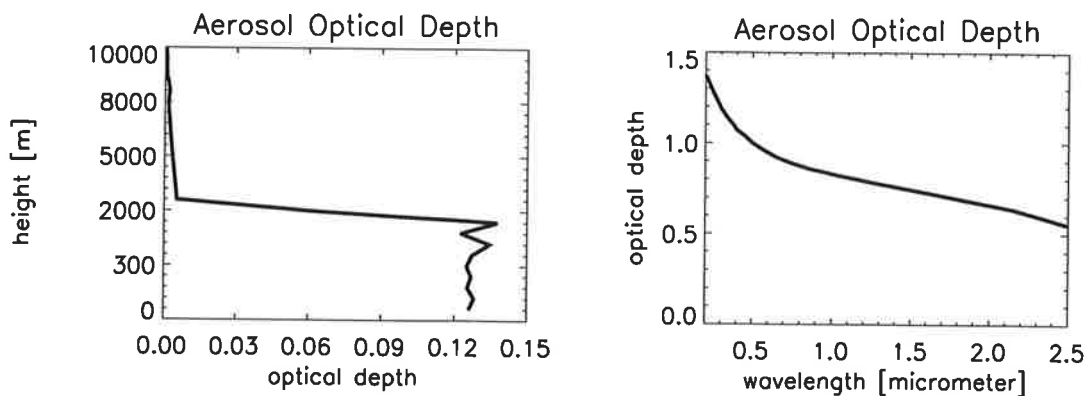
Figure 7.3: Vertical distribution of the modified aerosol optical depth (left panel) and wavelength dependence (right panel).

7.3 Results of the Simulations

Three model runs, all simulating July 23, are carried out each including a different aerosol characteristic: One experiment is carried out where aerosols are neglected completely, thus none of the three aerosol characterizing parameters, $\tilde{\omega}$, δ, and β are included in the radiative transfer module. This experiment is called 'no aerosol'. The second experiment, called 'standard aerosol', includes the standard and thus continental aerosol characteristics as presented in Fig. 7.2. The third experiment, 'urban aerosol', includes the modified optical thickness as discussed in Fig. 7.3.
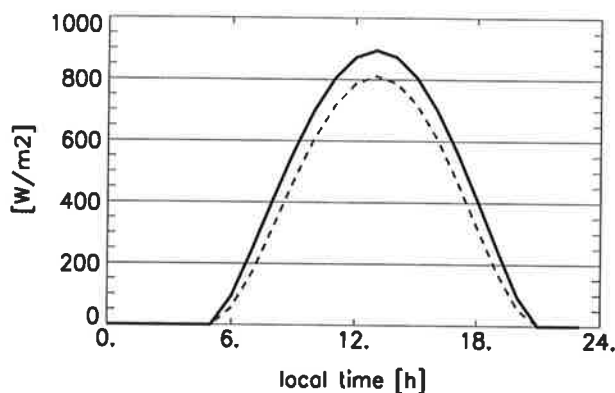
Figure 7.4: GESIMA results for solar irradiance for the 'no aerosol' (solid line) and the 'urban aerosol' (dashed line) simulation on July 23, 1994.

The comparison of the results of experiment 'no aerosol' and 'standard aerosol' shows only very weak differences. The maximum surface solar radiation is reduced in the standard aerosol run only by about 5 W/m^2. In accord all further influences are very weak.

Because of this extremely weak effect the 'no aerosol' experiment is chosen as basis case for the comparison with the 'urban aerosol' case. Fig. 7.4 shows that urban aerosols decrease surface solar radiation by 80 W/m^2 during peak daylight hours. This is a reduction of irradiance of around 10 %. The calculated decrease of 80 W/m^2 in surface solar radiation is comparable to the observed radiation reduction of 100 W/m^2 (Fig. 7.1). This decrease in solar radiation influences the heat and radiation fluxes. Latent heat flux is most strongly influenced with a reduction of up to 40 W/m^2 (30 %) at midday. The sensible heat flux decreases most strongly in the afternoon hours by about 10%. Net longwave radiation is also reduced by 10 %.
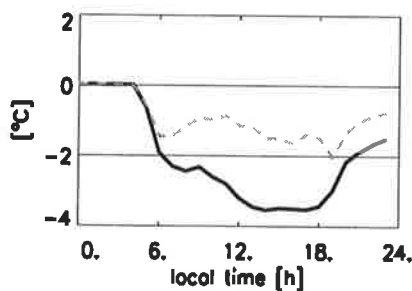
Figure 7.5: Time series of differences ('no aerosol' - 'urban aerosol') in surface temperature at a city (solid line) and a forest (dashed line) grid point.

The changes in radiation parameters lead to further influences: During the day aerosols attenuate direct solar radiation to the ground and cool the surface by about 1 - 3 °C relative to the 'no aerosol' case. Fig. 7.5 shows the change in surface temperature as simulated at a city and a forest grid point. Due to differences in their surface properties, e.g. albedo and heat capacity, the urban area shows stronger changes in surface temperature. Aerosol induced changes of more than −3 °C are simulated at the city grid point and a weaker response is calculated under forest conditions.
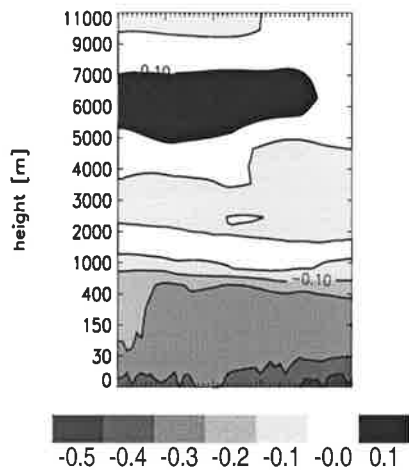
Figure 7.6: Vertical temperature distribution along 52.5°N latitude at 12 UTC. Differences between the experiments neglecting and including aerosol ('no aerosol' - 'urban aerosol') are shown in K.

The influence on atmospheric temperatures is presented in Fig. 7.6. Atmospheric temperatures decrease in the planetary boundary layer by about 0.5 K close to the earth's surface and 0.1 K at 1 km height. A weak increase in temperature is simulated at 6 - 7 km height induced by the increased scattered radiation. Since higher layers warm and the surface layer cools, stability of the atmosphere increases and influences the inversion height. Humidity is also affected by the change in heat and temperature fluxes. Due to the presence of aerosol humidity increases in the lower atmosphere, mostly in the forested regions by up to 8%.

The effects on the meteorological parameters are small but not negligible. The results are comparable to other model studies. For example calculations with an aerosol and radiation model (*Jacobsen et al.*, 1996; *Jacobsen*, 1997a) applied in the Los Angeles Basin (*Jacobsen*, 1997b) showed that the presence of aerosol reduced the peak daytime surface solar radiation by approximately 6.4 % (55 W/m^{-2}). It increased nighttime temperatures by about 0.77 °C, decreased daytime temperatures by about 0.08 °C, and increased overall temperatures (day plus night) by 0.43 °C compared to a 'no aerosol' case.

7.4 Discussion

The discussed model runs investigate the influence of urban aerosols on the meteorological parameters during cloud-free conditions. Aerosols have been crudely assumed by estimating an optical depth for urban smog conditions. In comparison to the FLUMOB radiation measurements and to other numerical investigations the model shows a plausible response. This model study was rather simple and primarily a test of the radiative transfer model. Chemistry was not considered in the simulations. The experiment should motivate further advanced aerosol studies including more physical and chemical aerosol properties. Such simulations which should include gas-phase chemistry, aerosol, and meteorological processes are important for analyses of the feedback and interaction processes in the changing atmosphere. 'On-line' models, such as REMO and GESIMA, build up the basis for these kinds of future studies.

The relevance of investigating radiative effects together with gas-phase chemistry in the polluted urban atmosphere has been demonstrated by *Dickerson et al.* (1997). He showed that greater UV flux in the boundary layer, due to an increase in scattered radiation, accelerates the rate of production of secondary sulfate and organic aerosol particles. These represent positive feedback mechanisms between particles and ozone. Enhanced scattered radiation increases photochemical activity and can potentially lead to increased ozone concentrations. On the other hand photochemical activity can be reduced by UV-absorbing aerosols such as mineral dust and

soot. But also changed atmospheric stability and temperatures affect photochemical production. Scattering aerosols tend to cool the boundary layer and stabilize the atmosphere with respect to convection. Lower temperature leads to less smog, but greater stability leads to more smog. A further very important point, beside heterogeneous chemical effects, is the ability of aerosol particles to affect cloud microphysics and thus indirectly impact on atmospheric stability and radiation.

However, these processes are not that important in Germany, where the UV radiation flux is moderate and large air pollution episodes occur only infrequently. But in other parts of the world these effects are of much greater importance. For example in the tropics where radiation is very strong and aerosols are released from megacities or by biomass burning. Investigations with interactive models in combination with LIDAR measurements, observing aerosol optical properties and ozone concentrations (*Matthias*, 2000a; *Immler*, 1999), could be of great interest for the analysis of feedback mechanisms between radiation and chemistry.

8 Summary and Conclusions

In this thesis, a summer smog episode, which was observed during the measurement campaign FLUMOB in summer 1994 in the area of Berlin-Brandenburg, was analysed with a complex high resolution atmosphere-chemistry model. In addition, the observed data sets of meteorological parameters and concentrations of chemical species were used for a detailed evaluation of the model results.

Within the framework of this thesis an atmospheric chemistry model was included in the non-hydrostatic atmosphere model GESIMA. The gas-phase chemistry mechanism RADM II was implemented for 'on-line' integrations together with the corresponding transport, deposition and emission modules. Furthermore GESIMA was embedded in the regional atmosphere-chemistry model REMO through a nesting technique of meteorological and chemical parameters. Thus, a mesoscale atmosphere-chemistry model chain was developed. To analyse observations made during the field experiment FLUMOB, the models were chosen to focus on the areas of Europe, Germany and Berlin-Brandenburg with increasing spatial resolution. The simulations covering Europe and Germany were carried out by the regional model. For the simulation covering the area of the measurement campaign Berlin-Brandenburg, the GESIMA model was applied.

The aim of the FLUMOB project was to measure the three-dimensional distribution of the concentrations of ozone and its precursors. The objective of the FLUMOB project was to increase the understanding of the ozone formation processes in the urban polluted atmosphere of Berlin and its rural environment and to create suitable emission control strategies for ozone reduction.

8.1 Conclusions with Respect to the FLUMOB Project

1) The two phases of FLUMOB
The FLUMOB period can be divided in two phases. They were induced by the meteorological conditions which lead to advection of relatively clean air masses from north easterly directions during the first days (first phase of FLUMOB) and to transport of polluted air masses to Brandenburg coming from south eastern directions during the following days (second phase of FLUMOB). During phase one, the air pollutants in Berlin-Brandenburg were mainly formed by local emitted precursors. Enhanced pollutant concentrations were found in the downwind direction of the strongest emission sources. During phase two, an increase of ozone and further air pollutants were observed in the entire domain. Additionally to local production, aged polluted air masses were transported to Brandenburg, originating from South Germany. Furthermore, the investigated domain was influenced by increased ozone concentrations in the free troposphere which, due to vertical mixing, also influenced the surface concentrations.

2) Dominance of biogenic hydrocarbons
The composition of hydrocarbons in Berlin-Brandenburg during the FLUMOB episode was made up by about 70-80% of biogenically emitted hydrocarbons, i.e. monoterpene and isoprene, and by about 20-30% of anthropogenically emitted hydrocarbons. Thus, natural emissions released by trees in the widely forested areas of Brandenburg dominate over anthropogenic emissions. This is of special importance for the process of ozone formation in the investigated area

because ozone production during FLUMOB was hydrocarbon limited so that their availability define the potential for ozone production and the peak concentrations.

This result is of fundamental importance for the FLUMOB project because the dominant role of biogenic hydrocarbons was completely underestimated. Measurements of hydrocarbons emitted by vegetation are complicated, because trees emit different types of hydrocarbons and the emission rates are very sensitive to temperature and irradiation. Especially monterpene emissions are known to increase exponentially at high temperature. These emissions are the major source of natural emissions in Berlin-Brandenburg because of the dominance of coniferous forests. To make an accurate estimate of the flux of various compounds from a given region requires a detailed knowledge of vegetation species composition and the emission characteristics. With respect to the objectives of FLUMOB, i.e. the study of ozone reduction strategies, the important role of the hydrocarbons has to be taken into account. This would possibly lead to the requirement of considerably stronger NO_x emission reduction strategies (*Roselle and Schere*, 1995; *Chameides et al.*, 1992) to reduce the occurrence of ozone episodes in this region.

As this conclusion was not drawn by previous studies of the FLUMOB project, the subsequent ozone measurement campaign in Berlin-Brandenburg, BERLIOZ (*Becker*, 2000; *Andersson and Steinhagen*, 2000), carried out in summer 1998, did not focus on biogenic hydrocarbons. However, the measurements made during BERLIOZ confirm the conclusions of this thesis concerning the composition of hydrocarbons in the Berlin-Brandenburg area during summer (*Becker*, 2000; *Winkler et al.*, 2000).

3) Increased ozone concentrations in the free troposphere
In spite of the stagnant high pressure weather conditions during FLUMOB, Brandenburg was influenced by long range transported ozone concentrations. Unusually high ozone concentrations were measured by the few ozone balloon soundings. In contrast to previous analysis, this investigation showed that the high ozone concentrations in the free troposphere must originate from outside of Europe. Due to vertical mixing process these high concentrations influenced the near surface concentrations during the second phase of FLUMOB. The influence of upper level ozone on near surface concentrations was also monitored during the BERLIOZ experiment. In contrast to the FLUMOB situation, the BERLIOZ case was even more influenced by transport processes. Therefore, observations of long lived trace gases, e.g. ozone, must include three-dimensional measurements especially when the processes of local ozone formation and distribution are investigated.

8.2   Conclusions Regarding the Model System

1) Validation of the GESIMA model
The FLUMOB case was characterized by homogeneous meteorological conditions and a complex chemical situation, a summer smog event. As a result the meteorological conditions were mostly driven by the large scale weather conditions. The meteorological validation shows high correlation between simulations and observations and provides therefore very satisfying results, although the FLUMOB case was not very demanding for the evaluation of the meteorological model performance. Nevertheless, it simplifies the analysis of the chemical simulation. The

validation of the chemical trace gas distributions exposes the high quality of the simulated urban ozone and nitrogen species. Primarily, this is an indication of the high quality of the anthropogenic emission data set. This is an important result because anthropogenic emission inventories are often assumed to introduce the largest source of uncertainty in chemical modelling. In general, the model validation detected a systematic underprediction of ozone. This underestimation was especially remarkable in the rural environment and in the free troposphere. The ozone underprediction inside the planetary boundary layer is mainly caused by two reasons: underestimation of local ozone production and of advected concentrations. The underpredicted ozone production is caused by underestimation of biogenic hydrocarbons by the models internal emission module. This emission module could not be validated because of lacking measurements. The underpredicted ozone transport into the model domain has to be attributed to the regional model. As the models GESIMA and REMO include several similar modules to calculate atmospheric gas-phase chemistry the analysed underprediction of biogenic emissions also happens in the regional model, so that deficiencies in the biogenic emission model are jointly responsible for a systematic underpredition of ozone. Certainly, a second reason for the underpredition of ozone in the lower atmosphere is the dramatically lack of ozone in the free troposphere because of vertical mixing causes also near surface concentrations to be influenced by the ozone concentrations above the planetary boundary layer.

However, the validation demonstrates the ability of the model system to reproduce realistic concentrations levels. Beside the discussed deficiencies in the emission module, which should be improved, the model system shows very satisfying results, so that further forecast, hindcast or scenario studies can be carried out.

2) Sensitivity to lateral boundary conditions

Ozone was dramatically underestimated by the model system in the free troposphere. The sensitivity study figured out that above the planetary boundary layer the amount of simulated ozone in GESIMA is completely dependent on the concentrations given to its lateral boundaries. Certainly, this result was expected and the lacking ozone in the free troposphere of GESIMA must be addressed to deficiencies in the regional model. The analysis of backward trajectories led to the assumption that the unusually high concentrations of upper tropospheric ozone originate from outside of Europe. Even the European wide simulation was not able to rebuild this situation because climatological conditions were assumed for the concentrations of the transported species at the lateral boundaries. Therefore global information about the three dimensional distribution of longer living chemical trace gases are necessary for regional modelling (*Langmann and Bauer*, 2000).

As the FLUMOB episode was characterized by the stagnant weather conditions this is an important result. The FLUMOB case should be investigated again with global chemical information at the boundaries of the mesoscale model system to study the combination of large local ozone production due to the summer smog event and the advection of long range transported ozone concentration.

3) Radiation reduction due to summer haze

The measured reduction of irradiance during the FLUMOB project could be explained by scattering of solar radiation by smog aerosols (direct aerosol effect). Thus, the influence of the chemical composition on the radiative budget was demonstrated. This experiment presented a

possible link between chemistry and meteorology, and should motivate further studies with the 'on-line' model system concentrating on chemical-physical feedback mechanisms.

8.3 Outlook

To increase the understanding of atmospheric chemistry in the investigated region a next step would be to further analyse the role of biogenic hydrocarbons in the urban polluted atmosphere. All conclusions were drawn on the basis of a theoretical study and could only be verified by ambient measurements focusing on natural emissions associated with high atmospheric temperatures and strong solar radiation. These measurements are also necessary to improve the knowledge about biogenic emissions and their inclusion into inventories. In respect to these aspects new emission control studies should be tested.

Furthermore, the embedding of the mesoscale model chain into a global model framework is planned. Comparisons of measured and modelled vertical profiles of chemical concentrations and meteorological parameters will be very useful to analyse the interplay between long lived transported species and the fast reacting compound which are most active in the boundary layer. Conversely, high resolving simulations are needed to analyse the impact of chemically active regions, e.g. megacities, industrial complexes, biomass burning, on the global budget of chemical compounds. Such investigations, for example, are important to assess possible changes in the oxidizing capacity of the atmosphere.

With respect to the GESIMA model, further validation is needed to test the model under different weather and chemical conditions and in different geographical areas. Especially the meteorological parameters should be validated for more complex weather conditions including cloud processes. Very interesting studies could be carried out in the area of Mexico D.F. where significant air pollution, complex topography (Mexico D.F. is embedded in a chain of mountains) and tropical meteorology interact. GESIMA includes very detailed physical parameterization schemes. Therefore, the model is particularly suitable to also include heterogeneous chemistry and thus couple the chemistry with cloud and radiation processes. Process studies could be performed to investigate, for example, the anthropogenic influence on cloud formation or feedback mechanisms between gas-phase and aerosol chemistry, radiation and photolysis rates. GESIMA is therefore not restricted to air pollution studies in urban environments, but could address several important other issues.

A   Chemical Species

Chemical species list of the RADM II mechanism.

Specie	chemical formula	nomenclature
Inorganic Compounds:		
Nitrogen dioxide	NO_2	NO2
Nitric oxide	NO	NO
Nitrous acid	HNO_2	HONO
Nitrogen trioxide	NO_3	NO3
Dinitrogen pentoxide	N_2O_5	N2O5
Nitric acid	HNO_3	HNO3
Pernitric acid	HNO_4	HNO4
Ozone	O_3	O3
Hydrogen peroxide	H_2O_2	H2O2
Sulfur dioxide	SO_2	SO2
Sulfuric acid	H_2SO_4	SULF
Carbon monoxide	CO	CO
Carbon dioxide	CO_2	product only
Ground state oxygen	O^3P	O3P
Excited oxygen	$O'D$	O1D
Hydroxy radical	OH	HO
Hydroperoxy radical	HO_2	HO2
Ammonia	NH_3	NH3
Molecular oxygen	O_2	O2
Molecular nitrogen	N_2	N2
Water	H_2O	H2O
Organic Compounds:		
Alkanes:		
Methane	CH_4	CH4
Ethane	C_2H_6	ETH
C3 to C5 Alkanes	C_3H_8	HC3
C6 to C8 Alkanes	C_5H_{12}	HC5
higher Alkanes	C_8H_{18}	HC8
Alkenes:		
Ethene	C_2H_4	OL2
terminal alkenes	C_3H_6	OLT
internal alkenes	C_4H_8	OLI
Isoprene	C_5H_8	ISO
Aromatics:		
Toluene	$CH_3C_6H_5$	TOL
Cresol	$HOC_6H_4\text{-}CH_3$	CSL
Xylane	$(CH_3)_2C_3H_4$	XYL

Carbonyls:		
Formaldehyde	H_2CO	HCHO
Acetaldehyde	R-CHO	ALD
Ketones	$CH_3CH_2\text{-}CO\text{-}CH_3$	KET
Glyoxal	$(CHO)_2$	GLY
Methylglyoxal	$CHO\,CO\,CH_3$	MGLY
other Dicarbonyls	$R\text{-}(CO)_2\text{-}R$	DCB
Organic nitrogen:		
Peroxyacetylnitrate	$CH_3\,CO_3\,NO_2$	PAN
TPAN	$CHOCH{=}CH\,CO_3\,NO_2$	TPAN
other organic nitrate	$R\text{-}NO_3$	ONIT
Organic peroxides:		
Methyl hydrogen peroxyde	CH_3O_2H	OP1
other organic peroxides	$R\text{-}O_2H$	OP2
Peroxyacetic acid	$CH_3CO\,OOH$	PAA
Organic acids:		
Formic acid	$HC\,OOH$	ORA1
Acetic acid	$CH_3\,COOH$	ORA2
Organic short lived intermediates:		
Methyl peroxy radical	CH_3O_2	MO2
Peroxy radical from ETH	$C_2H_5O_2$	ETHP
Peroxy radical from HC3	$R\text{-}O_2$	HC3P
Peroxy radical from HC5	$R\text{-}O_2$	HC5P
Peroxy radical from HC8	$R\text{-}O_2$	HC8P
Peroxy radical from OL2	$HO\,C_2H_4O_2$	OL2P
Peroxy radical from OLT	$HO\,C_4H_8O_2$	OLTP
Peroxy radical from OLI	$HO\,C_4H_8O_2$	OLIP
Peroxy radical from TOL	$HO\,CH_3C_6H_5O_2$	TOLP
Peroxy radical from XYL	$HO\,(CH_3)_2C_6H_4O_2$	XYLP
Acetyl peroxy radical	$CH_3\text{-}CO_3$	ACO3
Peroxy radical frem KET	$R\text{-}CO\text{-}R\text{-}O_2$	KETP
	$H(CO)\,CH{=}CHCO_3$	TCO3
NO_3-alkene adduct		OLN
additional organic nitrate		XNO2
NO-to-NO_2 conversion species		XO2

B Reaction Mechanism

RADM II: The gas-phase mechanism after Stockwell et al. (1990)

Nr.	Photolytical Reactions		
1	NO2 + $h\nu$	$\longrightarrow$	O3P + NO
2	O3 + $h\nu$	$\longrightarrow$	O1D + O2
3	O3 + $h\nu$	$\longrightarrow$	O3P + O2
4	HONO + $h\nu$	$\longrightarrow$	OH + NO
5	HNO3 + $h\nu$	$\longrightarrow$	OH + NO2
6	HNO4 + $h\nu$	$\longrightarrow$	HO2 + NO2
7	NO3 + $h\nu$	$\longrightarrow$	NO + O2
8	NO3 + $h\nu$	$\longrightarrow$	NO2 + O3P
9	H2O2 + $h\nu$	$\longrightarrow$	OH + OH
10	HCHO + $h\nu$	$\longrightarrow$	H2 + CO
11	HCHO + $h\nu$	$\longrightarrow$	HO2 + HO2 + CO
12	ALD + $h\nu$	$\longrightarrow$	MO2 + HO2 + CO
13	OP1 + $h\nu$	$\longrightarrow$	HCHO + HO2 + OH
14	OP2 + $h\nu$	$\longrightarrow$	ALD + HO2 + OH
15	PAA + $h\nu$	$\longrightarrow$	MO2 + CO2 + OH
16	KET + $h\nu$	$\longrightarrow$	ACO3 + ETHP
17	GLY + $h\nu$	$\longrightarrow$	0.13 HCHO + 1.87 CO
18	GLY + $h\nu$	$\longrightarrow$	0.45 HCHO + 1.55 CO + 0.8 HO2
19	MGLY + $h\nu$	$\longrightarrow$	ACO3 + HO2 + CO
20	DCB + $h\nu$	$\longrightarrow$	0.98 HO2 + 0.02 ACO3 + TCO3
21	ONIT + $h\nu$	$\longrightarrow$	0.2 ALD + 0.8 KET + HO2 + NO2

Nr.	Thermal Reactions		
1	O3P + O2	$\longrightarrow$	O3
2	O3P + NO2	$\longrightarrow$	NO + O2
3	O1D + N2	$\longrightarrow$	O3P + N2
4	O1D + O2	$\longrightarrow$	O3P + O2
5	O1D + H2O	$\longrightarrow$	OH + OH
6	O3 + NO	$\longrightarrow$	NO2 + O2
7	O3 + OH	$\longrightarrow$	HO2 + O2
8	O3 + HO2	$\longrightarrow$	OH + 2 O2
9	HO2 + NO	$\longrightarrow$	NO2 + OH
10	HO2 + NO2	$\longrightarrow$	HNO4
11	HNO4	$\longrightarrow$	HO2 + NO2
12	HO2 + HO2	$\longrightarrow$	H2O2 + O2
13	HO2 + HO2 + H2O	$\longrightarrow$	H2O2 + O2 + H2O
14	H2O2 + OH	$\longrightarrow$	HO2 + H2O
15	NO + OH	$\longrightarrow$	HONO
16	NO + NO + O2	$\longrightarrow$	NO2 + NO2
17	O3 + NO2	$\longrightarrow$	NO3 + O2
18	NO3 + NO	$\longrightarrow$	NO2 + NO2
19	NO3 + NO2	$\longrightarrow$	NO + NO2 + O2
20	NO3 + HO2	$\longrightarrow$	HNO3 + O2
21	NO3 + NO2	$\longrightarrow$	N2O5

Nr.	Thermal Reactions		
22	N2O5	$\longrightarrow$	NO2 + NO3
23	N2O5 + H2O	$\longrightarrow$	HNO3 + HNO3
24	OH + NO2	$\longrightarrow$	HNO3
25	OH + HNO3	$\longrightarrow$	NO3 + H2O
26	OH + HNO4	$\longrightarrow$	NO2 + H2O + O2
27	OH + HO2	$\longrightarrow$	H2O + O2
28	OH + SO2 + H2O + O2	$\longrightarrow$	SULF + HO2
29	CO + OH + O2	$\longrightarrow$	HO2 + CO2
30	CH4 + OH + O2	$\longrightarrow$	MO2 + H2O
31	ETH + OH + O2	$\longrightarrow$	ETHP + H2O
32	HC3 + OH + O2	$\longrightarrow$	0.83 HC3P + 0.17 HO2 + 0.09 HCHO + 0.075 ALD + 0.025 KET + H2O
33	HC5 + OH	$\longrightarrow$	HC5P + 0.25 XO2 + H2O
34	HC8 + OH	$\longrightarrow$	HC8P + 0.75 XO2 + H2O
35	OL2 + OH	$\longrightarrow$	OL2P
36	OLT + OH	$\longrightarrow$	OLTP
37	OLI + OH	$\longrightarrow$	OLIP
38	TOL + OH	$\longrightarrow$	0.75 TOLP + 0.25 CSL + 0.25 HO2
39	XYL + OH	$\longrightarrow$	0.83 + XYLP + 0.17 CSL + 0.17 HO2
40	CSL + OH	$\longrightarrow$	0.1 HO2 + 0.9 XO2 + 0.9 TCO3 - 0.9 OH
41	HCHO + OH	$\longrightarrow$	HO2 + CO + H2O
42	ALD + OH	$\longrightarrow$	ACO3 + H2O
43	KET + OH	$\longrightarrow$	KETP + H2O
44	GLY + OH	$\longrightarrow$	HO2 + 2 CO + H2O
45	MGLY + OH	$\longrightarrow$	ACO3 + CO + H2O
46	DCB + OH	$\longrightarrow$	TCO3 + H2O
47	OP1 + OH	$\longrightarrow$	0.5 MO2 + 0.5 HCHO + 0.5 OH
48	OP2 + OH	$\longrightarrow$	0.5 HC3P + 0.5 ALD + 0.5 OH
49	PAA + OH	$\longrightarrow$	ACO3 + H2O
50	PAN + OH	$\longrightarrow$	HCHO + NO3 + XO2
51	ONIT + OH	$\longrightarrow$	HC3P + NO2
52	ISO + OH	$\longrightarrow$	OLTP
53	ACO3 + NO2	$\longrightarrow$	PAN
54	PAN	$\longrightarrow$	ACO3 + NO2
55	TCO3 + NO2	$\longrightarrow$	TPAN
56	TPAN	$\longrightarrow$	TCO3 + NO2
57	MO2 + NO	$\longrightarrow$	HCHO + HO2 + NO2
58	HC3P + NO	$\longrightarrow$	0.75 ALD + 0.25 KET + 0.09 HCHO + 0.36 ONIT + 0.96 NO2 + 0.96 HO2
60	HC5P + NO	$\longrightarrow$	0.38 + ALD + 0.96 KET + 0.08 ONIT + 0.92 NO2 + 0.92 HO2
62	HC8P + NO	$\longrightarrow$	0.35 ALD + 1.06 KET + 0.04 HCHO + 0.24 ONIT + 0.76 NO2 + 0.76 HO2
64	OL2P + NO	$\longrightarrow$	1.6 HCHO + HO2 + NO2 + 0.2 ALD
65	OLTP + NO	$\longrightarrow$	ALD + HCHO + HO2 + NO2
66	OLIP + NO	$\longrightarrow$	HO2 + 1.45 ALD + 0.28 HCHO + 0.1 KET + NO2
67	ACO3 + NO	$\longrightarrow$	MO2 + NO2
68	TCO3 + NO	$\longrightarrow$	NO2 + 0.92 HO2 + 0.89 GLY + 0.11 MGLY + 0.05 ACO3 + 0.95 CO + 2 XO2
69	TOLP + NO	$\longrightarrow$	NO2 + HO2 + 0.17 MGLY + 0.16 GLY + 0.7 DCB
70	XYLP + NO	$\longrightarrow$	NO2 + HO2 + 0.45 MGLY + 0.806 DCB

Nr.	Thermal Reactions		
71	ETHP + NO	$\longrightarrow$	ALD + HO2 + NO2
72	KETP + NO	$\longrightarrow$	MGLY + HO2 + NO2
73	OLN + NO	$\longrightarrow$	HCHO + ALD + 2 NO2
74	HCHO + NO3	$\longrightarrow$	HO2 + HNO3 + CO
75	ALD + NO3	$\longrightarrow$	ACO3 + HNO3
76	GLY + NO3	$\longrightarrow$	HNO3 + HO2 + 2 CO
77	MGLY + NO3	$\longrightarrow$	HNO3 + ACO3 + CO
78	DCB + NO3	$\longrightarrow$	HNO3 + TCO3
79	CSL + NO3	$\longrightarrow$	HNO3 + XNO2 + 0.5 CSL
80	OL2 + NO3	$\longrightarrow$	OLN
81	OLT + NO3	$\longrightarrow$	OLN
82	OLI + NO3	$\longrightarrow$	OLN
83	ISO + NO3	$\longrightarrow$	OLN
84	OL2 + NO3	$\longrightarrow$	HCHO + 0.42 CO + 0.4 ORA1 + 0.12 HO2
85	OLT + NO3	$\longrightarrow$	0.53 HCHO + 0.5 ALD + 0.33 CO + 0.2 ORA1 + 0.2 ORA2 + 0.23 HO2 + 0.22 MO2 + 0.1 OH + 0.06 CH4
86	OLI + O3	$\longrightarrow$	0.18 HCHO + 0.72 ALD + 0.1 KET + 0.23 CO + 0.06 ORA1 + 0.29 ORA2 + 0.09 CH4 + 0.26 HO2 + 0.31 MO2 + 0.14 OH
87	ISO + O3	$\longrightarrow$	0.53 HCHO + 0.5 ALD + 0.33 CO + 0.2 ORA1 0.2 ORA2 + 0.23 HO2 + 0.22 MO2 + 0.1 OH
88	HO2 + MO2	$\longrightarrow$	OP1
89	HO2 + ETHP	$\longrightarrow$	OP2
90	HO2 + HC3P	$\longrightarrow$	OP2
91	HO2 + HC5P	$\longrightarrow$	OP2
92	HO2 + HC8P	$\longrightarrow$	OP2
93	HO2 + OL2P	$\longrightarrow$	OP2
94	HO2 + OLTP	$\longrightarrow$	OP2
95	HO2 + OLIP	$\longrightarrow$	OP2
96	HO2 + KETP	$\longrightarrow$	OP2
97	HO2 + ACO3	$\longrightarrow$	PAA
98	HO2 + TOLP	$\longrightarrow$	OP2
99	HO2 + XYLP	$\longrightarrow$	OP2
100	HO2 + TCO3	$\longrightarrow$	OP2
101	HO2 + OLN	$\longrightarrow$	ONIT
102	MO2 + MO2	$\longrightarrow$	1.5 HCHO + HO2
103	MO2 + ETHP	$\longrightarrow$	0.75 HCHO + HO2 + 0.75 ALD
104	MO2 + HC3P	$\longrightarrow$	0.84 HCHO + HO2 0.77 ALD + 0.26 KET
105	MO2 + HC5P	$\longrightarrow$	0.77 HCHO + HO2 + 0.41 ALD + 0.75 KET
106	MO2 + HC8P	$\longrightarrow$	0.8 HCHO + HO2 + 0.46 ALD + 1.39 KET
107	MO2 + OL2P	$\longrightarrow$	1.55 HCHO + HO2 + 0.35 ALD
108	MO2 + OLTP	$\longrightarrow$	1.25 HCHO + HO2 + 0.75 ALD
109	MO2 + OLIP	$\longrightarrow$	0.89 HCHO + HO2 + 0.73 ALD + 0.55 KET
110	MO2 + KETP	$\longrightarrow$	0.75 HCHO + HO2 + 0.75 MGLY
111	MO2 + ACO3	$\longrightarrow$	HCHO + 0.5 HO2 + 0.5 MO2 + 0.5 ORA2
112	MO2 + TOLP	$\longrightarrow$	HCHO + 2 HO2 + 0.17 MGLY + 0.16 GLY + 0.7 DCB
113	MO2 + XYLP	$\longrightarrow$	HCHO + 2 HO2 + 0.45 MGLY + 0.8 DCB
114	MO2 + TCO3	$\longrightarrow$	0.5 HCHO + 0.5 ORA2 + 0.445 GLY + 0.55 MGLY + 0.025 ACO3 + 0.475 CO + 0.46 HO2 + XO2
115	ETHP + ACO3	$\longrightarrow$	ALD + 0.5 HO2 + 0.5 MO2 + 0.5 ORA2

Nr.	Thermal Reactions		
116	HC3P + ACO3	$\longrightarrow$	0.77 ALD + 0.26 KET + 0.5 HO2 + 0.5 ORA2 + 0.5 MO2
117	HC5P + ACO3	$\longrightarrow$	0.41 ALD + 0.75 KET + 0.5 HO2 + 0.5 ORA2 + 0.5 MO2
118	HC8P + ACO3	$\longrightarrow$	0.46 ALD + 1.39 KET + 0.5 HO2 + 0.5 ORA2 + 0.5 MO2
119	OL2 P + ACO3	$\longrightarrow$	0.8 HCHO + 0.6 ALD + 0.5 HO2 + 0.5 ORA2 + 0.5 MO2
120	OLTP + ACO3	$\longrightarrow$	ALD + 0.5 HCHO + 0.5 HO2 + 0.5 ORA2 + 0.5 MO2
121	OLIP + ACO3	$\longrightarrow$	0.725 ALD + 0.55 KET + 0.14 HCHO + 0.5 HO2 + 0.5 MO2 + 0.5 ORA2
122	KETP + ACO3	$\longrightarrow$	MGLY + 0.5 HO2 + 0.5 ORA2 + 0.5 MO2
123	ACO3 + ACO3	$\longrightarrow$	2 MO2
124	ACO3 + TOLP	$\longrightarrow$	0.17 MGLY + 0.16 GLY
125	ACO3 + XYLP	$\longrightarrow$	MO2 + 0.45 MGLY + 0.806 DCB + HO2
126	ACO3 + TCO3	$\longrightarrow$	MO2 + 0.92 HO2 + 0.89 GLY + 0.11 MGLY + 0.05 ACO3 + 0.95 CO + 2 XO2
127	XO2 + HO2	$\longrightarrow$	OP2
128	XO2 + MO2	$\longrightarrow$	HCHO + HO2
129	XO2 + ACO3	$\longrightarrow$	MO2
130	XO2 + XO2	$\longrightarrow$	
131	XO2 + NO	$\longrightarrow$	NO2
132	XNO2 + NO2	$\longrightarrow$	ONIT
133	XNO2 + HO2	$\longrightarrow$	OP2
134	XNO2 + MO2	$\longrightarrow$	HCHO + HO2
135	XNO2 + ACO3	$\longrightarrow$	MO2
136	XNO2 + XNO2	$\longrightarrow$	
137	N2O5	$\longrightarrow$	HNO3
138	MO2 + OLN	$\longrightarrow$	1.75 HCHO + 0.5 HO2 + ALD +NO2
139	ACO3 + OLN	$\longrightarrow$	HCHO + ALD + 0.5 ORA2 + NO2 + 0.5 MO2
140	OLN + OLN	$\longrightarrow$	2 HCHO + 2 ALD + 2 NO2

C Statistical Methods for Time Series Analysis

Statistical parameters, based on recommendations by *Willmott* (1981, 1982) and *Willmott et al.* (1985) which in turn are based on *Fox* (1981), are used here to evaluate the meteorological and chemical simulation of near surface variables. This method is chosen because it is developed especially for the comparison of 1-dimensional variables and therefore suitable for the comparison of the simulated data with observed time series. The following quantitative measures will be introduced in the order of their appearance in the statistical tables in chapter 4 and 5:

(1) n denotes the number of measurements or model data included in the analysis.
(2 - 3) $\overline{O}$ and $\overline{M}$ show the observed and modelled means, respectively:

$$\overline{O} = \langle O_i \rangle \tag{C.1}$$

The angle brackets denote the time averaging operators.
(4 - 5) The standard deviations of the observed and simulated quantities are represented by δ_O and δ_M, respectively:

$$\delta_O = \sqrt{\langle (O_i - \overline{O})^2 \rangle} \tag{C.2}$$

(6) b stands for the slope of the least-squares linear regression between the simulated and observed values:

$$b = \frac{\langle M_i O_i - \overline{MO} \rangle}{\langle M_i^2 - \overline{M}^2 \rangle} \tag{C.3}$$

(7) and a for the according intercept:

$$a = \overline{O} - b * \overline{M} \tag{C.4}$$

(8) E denotes the root-mean-squared error:

$$E = \sqrt{\langle (M_i - O_i)^2 \rangle} \tag{C.5}$$

After *Willmott* (1981) the mean-square error, E^2, can be broken down into two components E_S and E_U with:

$$E^2 = \langle (\hat{M}_i - O_i)^2 \rangle + \langle (M_i - \hat{M}_i)^2 \rangle = E_S^2 + E_U^2 \tag{C.6}$$

$\hat{M}_i$ describes the the least-squares linear regression between the modelled and observed values:

$$\hat{M}_i = a + bO_i \tag{C.7}$$

(9 - 10) The two terms E_S^2 and E_U^2 are the systematic and unsystematic components of the mean-square error respectively. The systematic error component is made up entirely of errors due to additive and proportional systematic errors, as follows:

$$E_S^2 = a^2 + (b-1)^2 \langle O_i^2 \rangle + 2a(b-1)\langle O_i \rangle \tag{C.8}$$

When the least-square linear regression has zero intercept, a, and a slope, b of unity, the systematic mean-error vanishes *Hedley and Singleton* (1997). The unsystematic mean-square error contains all other types of errors due to any nonlinear relationship between M and O. *Willmott* (1981, 1982) argumented that removing systematic errors from a model prediction should involve only minor modifications to the model parameterizations, while unsystematic errors could be interpreted as the precision of the model, or alternatively, as the potential accuracy of the model after the removal of systematic errors.
(11) r^2 a linear correlation coefficient of two vectors calculated with:

$$r = \frac{\sum_{i=0}^{n-1}(O_i - \overline{O})(M_i - \overline{M})}{\sqrt{\sum_{i=0}^{n-1}(O_i - \overline{O})^2(M_i - \overline{M})^2}} \tag{C.9}$$

(12) The index-of-agreement, d, which is calculated as

$$d = 1 - \frac{E^2}{\langle(|M_i'| + |O_i'|)^2\rangle}, \quad 0 \le d \le 1 \tag{C.10}$$

where the primed quantities are the departures from the mean observed value ($O_i' = O_i - \overline{O}$). A value of $d = 1$ indicates perfect agreement, and $d = 0$ indicates absolutely no agreement. This index specifies the degree to which the observed deviations about $\langle O_i \rangle$ correspond in magnitude and sign to the modelled deviations about $\langle M_i \rangle$.

References

Al-Wali, K. I., and P. J. Samson, Preleminary sensitivity analysis of urban airshed model simulations to temporal and spatial availability of boundary layer wind measurements, *Atmos. Environ.*, *30*, 2027–2042, 1996.

Anderson, D. A., J. C. Tannehill, and R. H. Flechter, *Computational Fluid Dynamics and Heat Transfer*, Hemisphere Publishing Corporation, New York, 1984.

Andersson, S., and H. Steinhagen, Untersuchungen zur Dynamik der atmosphärischen Grenzschicht und von Vertikalverteilungen ausgewählter Spurenstoffe mit Hilfe von Windprofiler-Radar/RASS und Fesselballonsondierungen zur Oxidantienbildung und Oxidationskapazität. Deutscher Wetterdienst, Met. Observatorium Lindenberg, 2000.

Atkinson, R., Gas-phase tropospheric chemistry of organic compounds: A review, *Atmos. Environ.*, *24A*(1), 1–41, 1990.

Becker, K. H., Förderschwerpunkt Troposphärenforschung 1996-2000, Kurzübersicht Leitthema 3: Prozeßstudien zur Oxidantienbildung und Oxidationskapazität, Bundesministerium für Bildung und Forschung, Institut für Physikalische Chemie, Bergische Universität GH Wuppertal, 2000.

Beniston, M., and J. Schmetz, A three-dimensional study of mesoscale model response to radiative forcing, *Boundary Layer Meteorol.*, *31*, 149–175, 1985.

Bott, A., A positive definite advection scheme obtained by nonlinear renormalization of the advective fluxes, *Mon. Wea. Rev.*, *117*, 1006–1015, 1989.

Bouchet, V. S., R. Laprise, E. Torlaschi, and J. C. McConell, Studying ozone climatology with a regional climate model 1. Model description and evaluation, *J. Geophys. Res.*, *104*(D23), 30351–30371, 1999a.

Bouchet, V. S., R. Laprise, E. Torlaschi, J. C. McConell, and D. A. Plummer, Studying ozone climatology with a regional climate model 2. Climatology, *J. Geophys. Res.*, *104*(D23), 30373–30385, 1999b.

Brasseur, G. P., D. A. Hauglustaine, S. Walters, P. J. Rasch, J. F. Muller, C. Granier, and X. X. Tie, MOZART, a global chemical transport model for ozone and related chemical tracers 1. Model description, *J. Geophys. Res.*, *103*(D21), 28265–28289, 1998.

Briggs, G. A., Plume rise prediction, *Letters of Airpollution and Environmental Impact Analysis. American Meteorological Society, Boston, MA*, pp. 59–111, 1975.

Brost, R. A., The sensitivity to input parameters of atmospheric concentrations simulated by a regional chemical-model, *J. Geophys. Res.*, *93*(D3), 2371–2387, 1988.

Bruckmann, P., et al., *Bewertung temporärer Maßnahmen zur Senkung von Ozonbelastungsspitzen*, Schriftreihe des LAI. Vol. 14, Erich Schmidt Verlag, Berlin, 1997.

Bruckmann, P., and M. Wichmann-Fiebig, The efficiency of short term actions to abate summer smog results from field studies and model calculations, vol. 19 of *EUROTRACT Newsletter*, 1997.

Businger, J. A., Turbulent transport in the atmospheric surface layer, in *Workshop on Micrometeorology, American Meteorological Society, Boston, MA*, pp. 67–100, 1973.

Carpenter, K. M., An experimental forecast using a non-hydrostatic mesoscale model, *Quart. J. Roy. Meteor. Soc.*, *105*, 629–655, 1979.

Chameides, W. L., et al., Ozone precursor relationships in the ambient atmosphere, *J. Geophys. Res*, *97*(D5), 6037–6055, 1992.

Chandrasekhar, S., *Radiative Transfer*, Dover Publ. Inc., New York, 393 pp., 1960.

Chang, J., R. A. Brost, I. S. A. Isaksen, S. Madronich, P. Middleton, W. R. Stockwell, and C. J. Walcek, A three-dimensional Eulerian acid deposition model: Physical concepts and formulation, *J. Geophys. Res.*, *92*(D12), 14681 –14700, 1987.

Clark, T. L., A small-scale dynamic model using terrain following coordinate transformation, *J. Comp. Phys.*, *24*, 186–215, 1977.

Crassier, V., K. Suhre, P. Tulet, and R. Rosset, Development of a reduced chemical scheme for use in mesoscale meteorological models, *Atmos. Environ.*, *24*, 2633–2644, 2000.

d'Almeida, G. A., P. Koepke, and E. P. Shettle, *Atmospheric Aerosols. Global Climatology and Radiative Characteristics*, A. DEEPAK Publishing, 1991.

DeMore, W. B., S. P. Sander, M. J. Molina, D. M. Golden, R. F. Hampson, M. J. Kurylo, C. Howard, and A. R. Ravishankara, Chemical kinetics and photochemical data for use in stratospheric modeling, evaluation number 8, in *National Aeronautics and Space Administration, Jet Propulsion Laboratory, California Institute of Technology, Pasadena*, 1988.

Derwent, R. G., Evaluation of a number of chemical mechanisms for their application in models describing the formation of photochemical ozone in Europe, *Atmos. Environ.*, *24A*(10), 2615–2624, 1990.

Devantier, R., and A. Raabe, Application of a quasispectral cloud parameterization scheme to a mesoscale snowfall event over the Baltic Sea, *Contr. Atmosph. Phys.*, *69*, 375–384, 1996.

Dickerson, R. R., S. Kondragunta, G. Stechnikov, K. Civerolo, B. G. Doddridge, and B. B. Holben, The impact of aerosols on solar ultraviolet radiation and photochemical smog, *Science*, *278*(31), 827–830, 1997.

Durran, D., and J. Klemp, A compressible model for the simulation of moist moutain waves, *Mon. Wea. Rev.*, *111*, 2341–2361, 1983.

Eppel, D. P., H. Kapitza, M. Claussen, D. Jacob, W. Koch, L. Levkov, H.-T. Mengelkamp, and N. Werrmann, The non-hydrostatic mesoscale model GESIMA. Part II: Parameterizations and applications, *Contr. Atmosph. Phys.*, *68*, 15–41, 1995.

Fox, D. G., Judging air quality model performance: A summary of the AMS workshop on dispersion of model performance, *Bull. Amer. Met. Soc.*, *62*, 599–609, 1981.

Gao, D., W. Stockwell, and J. B. Milford, Global uncertainty analysis of a regional scale gas phase mechanism, *J. Geophys. Res.*, *101(D4)*, 9071–9078, 1996.

Geb, M., and B. Naujokat, Nordhemisphärischer Klimabericht zum Juli 1994. Beilage zur Berliner Wetterkarte Nr. 86/94, Amtsblatt des Instituts für Meteorologie, 1994.

Gery, M. W., G. Z. Whitten, J. P. Killus, and M. Dodge, A photochemical kinetics mechanism for urban and regional scale computer modeling, *J. Geophys. Res.*, *94*(D10), 12925–12956, 1989.

Golding, B. W., An efficient non-hydrostatic forecast model, *Meteorol. Atmos. Phys.*, *50*, 89–103, 1992.

Golding, G. W., The meteorological office mesoscale model, *Meteorol. Mag.*, *119*, 81–96, 1990.

Guenther, A. B., R. K. Monson, and R. Fall, Isoprene and monoterpene emission rate variability: Observations with eucalyptus and emission rate algorithm development, *J. Geophys. Res.*, *96*(D6), 10799–10808, 1991.

Guenther, A. B., P. K. Zimmermann, P. C. Harley, R. K. Monson, and R. Fall, Isoprene and monoterpene emission rate variability: Model evaluations and sensitivity analysis, *J. Geophys. Res.*, *98*(D7), 12609–12617, 1993.

Hass, H., Description of the EURAD chemistry-transport-model version 2 (CTM2), eds. A. Ebel, F. M. Neubauer and P. Speth, Report 83, Institut of Geophysics and Meteorology, University of Cologne, Germany, 1991.

Hassel, D., P. Jost, F.-J. Weber, F. Dursbeck, K.-S. Sonnenborn, and D. Plettau, Das Abgas-Emissionsverhalten von Personenkraftwagen in der Bundesrepublik Deutschland im Bezugsjahr 1990, *Technischer Überwachungsverein Rheinland. Erich Schmidt Verlag. Berichte Umweltbundesamt 8/94. Berlin*, 1994.

Hassel, D., P. Jost, F.-J. Weber, F. Dursbeck, K.-S. Sonnenborn, and D. Plettau, Das Abgas-Emissionsverhalten von Nutzfahrzeugen in der Bundesrepublik Deutschland im Bezugsjahr 1990, *Technischer Überwachungsverein Rheinland. Erich Schmidt Verlag. Berichte Umweltbundesamt 5/95. Berlin*, 1995.

Hassel, D., F.-J. Weber, and T. Schmitz, Zusammensetzung der Kohlenwasserstoffe für unterschiedliche Fahrzeugkonzepte, *Technischer Überwachungsverein Rheinland Sicherheit und Umweltschutz GmbH, Forschungszentrum Jülich GmbH. TFS-Projekt, LT2, Projekt A.2, Köln*, 1998.

Hauglustaine, D. A., G. P. Brasseur, S. Walters, P. J. Rasch, J. F. Muller, L. K. Emmons, and C. A. Carroll, MOZART, a global chemical transport model for ozone and related chemical tracers 2. Model results and evaluation, *J. Geophys. Res.*, *103*(D21), 28291–28335, 1998.

Hedley, M., and D. Singleton, Evaluation of an air quality simulation of the lower fraser valley: 1. Meteorology, *Atmos. Environ.*, *31*(11), 1605–1615, 1997.

Heimann, D., Ein Drei-Schichtenmodell zur Berechnung mesoskaliger Wind- und Immisionsfelder über komplexem Gelände, Ph.D. thesis, Universität München, 1985.

Hesstvedt, E., Ø. Hov, and I. S. A. Isaksen, Quasi-steady state approximation in air pollution modeling: Comparison of the two numerical schemes for oxidant prediction, *Int. J. Chem. Kinet.*, *10*, 971–994, 1978.

Horvath, H., Spectral extinction coefficients of rural aerosol in southern Italy - a case study of cause and effect of variability of atmospheric aerosol, *J. Aerosol Sci.*, *27*(3), 437–453, 1996.

Immler, F., Lidar-Fernerkundung von troposphärischem Ozon und Aerosole in einer urbanen Umgebung, Ph.D. thesis, Institut für Experimental Physik, Frei Universität Berlin, 1999.

Jacob, D., and R. Podzun, Sensitivity studies with the regional climate model REMO, *Meteorol. Atmos. Phys.*, *63*(1-2), 119–129, 1997.

Jacobsen, M. Z., Development and application of a new air pollution modelling system - Part II. Aerosol module structure and design, *Atmos. Environ.*, *31*(2), 131–144, 1997a.

Jacobsen, M. Z., Development and application of a new air pollution modelling system - Part III. Aerosol - phase simulations, *Atmos. Environ.*, *31*(4), 587–608, 1997b.

Jacobsen, M. Z., Isolating nitrated and aromatic aerosols and nitrated aromatic gases as sources of ultraviolet light absorption, *J. Geophys Res.*, *104*(D3), 3527–3542, 1999.

Jacobsen, M. Z., A. Tabazadeh, and R. P. Turco, Development and application of a new air pollution modelling system - Part I. Gas-phase simulations, *Atmos. Environ.*, *30B*, 1939–1963, 1996.

Jacovides, C. P., D. N. Asimakopoulos, and M. D. Steven, On the optical properties of the polluted Athens atmosphere, during May 1995, *Atmos. Environ.*, *33*, 3427–3431, 1999.

Jáuregui, E., and E. Luyando, Global radiation attenuation by air pollution and its effects on the thermal climate in Mexico City, *Int. J. Climatol.*, *19*, 683–694, 1999.

Joseph, J. H., W. J. Wiscombe, and J. A. Weinmann, The delta-Eddington approximation for radiative flux transfer, *J. Atmos. Sci.*, *33*, 2452–2458, 1976.

Kanter, H. J., R. Schmidt, and F. Slemr, Flugzeugmessungen von Ozon und Vorläuferstoffen über Berlin und Umgebung. Abschlußbericht. Frauenhofer-Institut für Atmosphärische Umweltforschung, Kreuzeckbahnstraße 19, D-82467 Garmisch-Partenkirchen, 1995.

Kapitza, H., Truncated incomplete factorizations for conjugate-gradient methods in two and three dimensions, *Appl. Math. Comp.*, *28*, 73–87, 1988.

Kapitza, H., *GESIMA Documentation Manual*, GKSS Research Centre, Max-Planck-Str. D-21502 Geesthacht, 1999.

Kapitza, H., and D. P. Eppel, A 3-d Poisson solver based on conjugate gradients compared to standard iterative methods and its performance on vector computers, *J. Comp. Phys.*, *68*, 474–484, 1987.

Kapitza, H., and D. P. Eppel, The non-hydrostatic mesoscale model GESIMA. Part I: Dynamical equations and tests, *Contr. Atmosph. Phys.*, *65*, 129–146, 1992.

Kato, T., Hydrostatic and non-hydrostatic simulations of moist convection: Review and further studies, *Meteorol. Atmos. Phys.*, *63*, 39–51, 1997.

Kaufmann, Y. J., and R. S. Fraser, Light extinction by aerosols during summer air pollution, *J. Clim. and Appl. Met*, *22*, 1694–1706, 1983.

Kerschgens, M., U. Pilz, and E. Raschke, A modified two-stream approximation for computations of the solar radiation budget in a cloudy atmosphere, *Tellus*, *30*, 429–435, 1978.

Kleinman, L. I., Photochemical formation of peroxides in the boundary layer, *J. Geophys. Res.*, *91*, 10889–10904, 1986.

Kleinman, L. I., et al., Ozone formation at a rural site in the southeastern United States., *J. Geophys. Res.*, *99*, 3469–3482, 1994.

Kondratyev, K. Y., *Radiation in the Atmosphere*, Academic Press, 1969.

Krüger, K., personal communication.

Kühlwein, J., R. Friedrich, A. Obermeier, and J. Theloke, Abschätzung und Bewertung der Unsicherheiten hochauflösender NO_x und NMVOC-Emissionsdaten, *PEF Projekt Bericht. Institut für Energiewirtschaft und Rationelle Energieanwendung (IER), Stuttgart*, 1999.

Kumar, N., and A. G. Russell, Comparing prognostic and diagnostic meteorological fields and their impacts on photocemical air quality modeling, *Atmos. Environ.*, *30*, 1989–2010, 1996.

Langmann, B., Numerical modelling of regional scale transport and photochemistry directly together with meteorological processes, *Atmos. Environ.*, *34*, 3585–3598, 2000.

Langmann, B., and S. E. Bauer, On the importance of reliable initial and boundary concentrations of ozone for regional scale air pollution modelling, *submitted to J. of Atm. Chem.*, 2000.

Madronich, S., Photodissociation in the atmosphere 1: Actinc flux and the effects of ground reflections and clouds, *J. Geophys. Res*, *92*, 9740–9752, 1987.

Majewski, D., The Europa Modell of the Deutscher Wetterdienst, Tech. Rep. 2, Seminar Proceedings ECMWF, pp. 114, 1991.

Marsik, F. J., K. W. Fischer, T. D. McDonald, and P. J. Samson, Comparison of methods for estimating mixing heights used during the 1992 Atlanta field itensive, *J. Appl. Met.*, *34*, 1802–1814, 1995.

Matthias, V., Vertikalmessungen der Aerosolextinktion und des Ozons mit einem UV-Raman-Lidar, Ph.D. thesis, Max-Planck Institut für Meteorologie, Hamburg, 2000a.

Matthias, V., peronal communication, 2000b.

Mellor, G. L., and T. Yamada, A hierarchy of turbulence closure models for planetary boundary layers, *J. Atmos. Sci.*, *31*, 1791–1806, 1974.

Mesinger, F., and A. Arakawa, Numerical methods used in atmospheric models, Tech. rep., GARP Publ. series No 17 Vol. 1, 64 p., 1976.

Middleton, P., W. R. Stockwell, and W. P. L. Carter, Aggregation and analysis of volatile organic compound emissions for regional modelling, *Atmos. Environ.*, *24A*(5), 1107–1133, 1990.

Mieth, P., S. Unger, R. P. Schäfer, and M. Schmidt, Simulation der Ozonproduktion in Berlin und Brandenburg für den Zeitraum der FLUMOB-Meßkampagne. GMD First im Auftrag der Senatsverwaltung für Stadtentwicklung und Umweltschutz Berlin und des Ministeriums für Umwelt, Naturschutz und Raumordnung des Landes Brandenburg, 1995.

Neininger, B., and B. Bäumle, Flugmeßdaten Berlin 1994. Projektbericht. Ein Auftrag der Länder Berlin und Brandenburg, vertreten durch die Fachhochschule Wildau, MetAir, Länggstraße 19, Postfach, CH-8308 Illnau, 1994.

Ogura, Y., and N. A. Phillips, Scale analysis of deep and shallow convection in the atmosphere, *J. Atmos. Sci.*, *19*, 173–179, 1962.

Oke, T. R., Review of urban climatology 1973-1978, WMO Technical Note 169, 100 pp., 1976.

O'Neill, M. T., A. Royer, and P. Cote, Relations between optically derived aerosol parameters, humidity, and air-quality data in an urban atmosphere, *J. Appl. Met.*, *32*, 1484–1498, 1993.

Orlanski, I., The quasi hydrostatic approximation, *J. Comp. Phys.*, *21*, 251–269, 1981.

Pielke, R. A., *Mesoscale Meteorological Modelling*, Academic Press, Inc., San Diego, 1984.

Pleim, J. E., J. S. Chang, and K. Zhang, A nested grid mesoscale atmospheric chemistry model, *J. Geophys. Res.*, *96*(D2), 3065–3084, 1991.

Radinov, V. F., E. Rusina, M. V. Lamakin, U. Leiterer, and A. M. Shalamyanskii, Experimental studies of aerosol optical thickness and ozone in large-city environs, *Izvestiya Atm. and Oc. Phys.*, *35*(5), 596–601, 1999.

Roberts, J. M., *Reactive odd-nitrogen (NO_y) in the atmosphere*, Composition, Chemistry and Climate of the Atmosphere, edited by H. B. Singh. Van Nostrand Reinhold, New York. pp. 176 - 215, 1995.

Rockel, B., E. Raschke, and B. Weyres, A parameterization of broad band radiative properties of water, ice and mixed phase clouds, *Contr. Atmosph. Phys.*, *64*, 1–12, 1991.

Roeckner, E., et al., The atmospheric general circulation model ECHAM-4: Model description and simulation of present-day climate, Tech. rep., MPI Report No 218, Hamburg, Germany., 1996.

Roeckner, E., L. Bengtsson, J. Feichter, L. Lelieveld, and H. Rodhe, Transient climate change simulations with a coupled atmosphere-ocean GCM including the tropospheric sulfur cycle, *J. Climate*, *12*(10), 3004–3032, 1999.

Roelofs, G. J., and J. Lelieveld, Distribution and budget of O_3 in the troposphere calculated with a chemistry general-circulation model, *J. Geophys. Res.*, *100*(D10), 20983–20998, 1995.

Roselle, S. J., and K. L. Schere, Modeled response of photochemical oxidants to systematic reductions on anthropogenic volatile organic compound and NO_x emissions, *J. Geophys. Res.*, *100*(D11), 22929–22941, 1995.

Rufeger, W., and P. Mieth, The DYMOS system and its application to urban areas, *Environmental Modelling & Software*, *13*, 287–294, 1998.

Schaller, E., and A. Wenzel, Evaluierung regionaler atmosphärischer Chemie-Transport-Modelle, Fall 1: TRACT, 16.9.1992, 13 - 17 Uhr MESZ, Brandenburgische Technische Universität, 1999.

Schmetz, J., On the parameterization of the radiative properties of broken clouds, *Tellus*, *36A*, 417–432, 1984.

Schmetz, J., and M. Beniston, Relative effects of solar and infrared radiative forcing in a mesoscale model, *Boundary Layer Meteorol.*, *34*, 137–155, 1986.

Schmetz, J., and E. Raschke, An application of a two stream approximation to calculations of the transfer of solar radiation in an atmosphere with fractional cloud cover, *Contr. Atmosph. Phys.*, *52*, 151–160, 1979.

Seinfeld, J. H., and S. N. Pandis, *Atmospheric Chemistry and Physics. From Air Pollution to Climate Change*, John Wiley and Sons, Inc. New York, 1998.

Shindell, D. T., J. L. Grenfell, D. Rind, C. Price, and V. Grewe, Chemistry-climate interactions in the GISS GCM. Part 1: Tropospheric chemistry model description and evaluation, submitted to *J. Geophys. Res.* June 15, 2000.

Sillman, S., The relation between ozone, NO_x and hydrocarbons in urban and polluted rural environments, *Atmos. Environ.*, *33*, 1821–1845, 1999.

Sillman, S., J. A. Logan, and S. C. Wofsy, The sensitivity of ozone to nitrogen oxides and hydrocarbons in regional ozone episodes, *J. Geophys. Res.*, *95*(D2), 1837–1851, 1990.

Sistla, G., N. Zhou, W. Hou, J.-Y. Ku, S. T. Rao, R. Bornstein, F. Freedman, and P. Thuns, Effects of uncertainties in meteorological inputs on urban airshed model predictions and ozone control strategies, *Atmos. Environ.*, *30*, 2011–2025, 1996.

Smolarkiewicz, P. K., A simple positive definite advection scheme with small implicit diffusion, *Mon. Wea. Rev.*, *111*(3), 479–486, 1983.

Smolarkiewicz, P. K., A fully multidimensional positive definite advection transport algorithm with small implicit diffusion, *J. Comp. Phys.*, *54*, 325–362, 1984.

Sorbjan, Z., On similarity in the atmospheric boundary layer, *Bound. Layer Meteor.*, *34*, 377–397, 1986.

Stark, B., H.-J. Abraham, P. Lutz, M. Reichenbächer, W. Reimer, and E. Scherer, Flugzeug- und Bodenmessungen von Ozon und Verläuferstoffen zur Abschätzung der Wirksamkeit von emissionsmindernden Maßnahmen im Großraum Berlin-Brandenburg (FLuMOB-Projekt), *Abschlußbericht im Auftrag der Senatverwaltung für Stadtentwicklung und Umweltschultz*

Berlin und des Ministeriums für Umwelt und Raumordnung des Landes Brandenburg, Berlin, 1995.

Stockwell, W. R., P. Middleton, and J. S. Chang, The second generation regional acid deposition model chemical mechanism for regional air quality modeling, *J. Geophys. Res.*, *95*(D10), 16343–16367, 1990.

Tapp, M. C., and P. White, A non-hydrostatic mesoscale model, *Quart. J. Roy. Meteor. Soc.*, *102*, 277–296, 1976.

Tiedtke, M., A comprehensive mass flux scheme for cumulus parameterization in large-scale models, *Mon. Wea. Rev.*, *117*, 1779–1800, 1989.

Trainer, M., et al., Observations and modeling of the reactive nitrogen photochemistry at a rural site, *J. Geophys. Res.*, *96*(D2), 3045–3063, 1991.

Trainer, M., et al., Correlation of ozone with NO_y in photochemically aged air, *J. Geophys. Res.*, *98*(D2), 2917–2925, 1993.

Tulet, P., A. Maalej, V. Crassier, and R. Rosset, An episode of photooxidant plume pollution over the Paris region, *Atmos. Environ.*, *33*, 1651–1662, 1999.

UBA, Handbuch für Emissionsfaktoren das Straßenverkehrs, *Umweltbundesamt, Bundesamt für Umwelt, Wald und Landschaftsschutz, Bern, INFRAS AG, Bern.(Erschienen als Software auf CD-ROM)*, 1995.

Walcek, C. J., and G. R. Taylor, A theoretical method for computing vertical distributions of acidity and sulfate production within cumulus clouds, *J. Atmos. Sci.*, *43*, 339–355, 1986.

Wesely, Parameterization of surface resistances to gaseous dry deposition in regional-scale numerical models, *Atmos. Environ.*, *23*, 1293–1304, 1989.

Wickert, B., personal communication.

Willmott, C. J., On the validation of models, *Phys. Geography*, *2*, 168–194, 1981.

Willmott, C. J., Some comments on the evaluation of model performance, *Bull. Amer. Met. Soc.*, *63*, 1309–1313, 1982.

Willmott, C. J., S. Acklestopn, R. E. Feddema, J. Klin, D. Legates, J. O'Donnell, and C. M. Rowe, Statistics for the evaluation and comparison of models, *J. Geophys. Res.*, *90*, 8995–9005, 1985.

Winkler, J., et al., Ground-based and airborne measurements of nonmethane hydrocarbons in BERLIOZ: Analysis and selected results, submitted September, 2000.

Wippermann, F., The applicability of several approximations in mesoscale modelling - a linear approach, *Contr. Atmosph. Phys.*, *54*, 298–308, 1981.

Zdunkowski, W. G., G. J. Korb, and C. T. Davies, Radiative transfer in model clouds of variable height and constant liquid water content as computed by approximate and exact methods, *Contr. Atmosph. Phys.*, *47*, 157–186, 1974.

Danksagung

Zunächst möchte ich mich bei Bärbel Langmann für die intensive Betreuung meiner Doktorarbeit und der damit verbundenen Entdeckung der spannenden Welt der Atmosphären-Chemie ganz herzlich bedanken.

Lennart Bengtsson und Guy Brasseur habe ich beiden für die Betreuung meiner Doktorarbeit zu danken. Lennart Bengtsson hat mich in das Institut aufgenommen und Guy Brasseur hat mich als Doktorandin übernommen. Beiden danke ich sehr für ihre hilfreiche Unterstützung besonders während der Endphase meiner Arbeit.

Hartmut Graßl danke ich für die motivierenden Gespräche und seine Betreitschaft diese Arbeit zu begutachten.

Für alle Fragen die den dynamischen Teil des Modells betreffen habe ich sehr viel Unterstützung von Hartmut Kapitza und Dieter Eppel bekommen. Dafür und für die zeitweilige Aufnahme bei der GKSS möchet ich mich sehr bedanken.

Diese Arbeit wurde im Rahmen des TFS-Projekts gefördert. Allen daran beteiligten Personen möchte ich für die Zusammenarbeit danken, besonders Burckhard Wickert für die Berechnungen der Emissionskataster.

Den Bewohnern des Erdgeschosses des Schlumps und auch vielen weiteren MPI-lern danke ich für die technische und moralische Unterstützung und die schöne Zeit am MPI.

Für die sprachliche und inhaltliche Überarbeitung meines Manuskriptes danke ich den folgenden Personen ganz besonders herzlich: Bärbel Langmann - Guy Brasseur - Lennart Bengtsson - Christiane Textor - Bruce Denby - Laura Klein - Stacy Walters - Hartmut Graßl - Christine Land - Hartmut Kapitza - Christoph Raible - Catherine Hahn - Marko Scholze.

DANKE !

EXAMENSARBEIT Nr. 59
August 1998

Variability on decadal scales in Pacific sea surface temperatures and atmosphere ocean interaction in the coupled general circulation model ECHAM4/OPYC3
Andreas Bacher

EXAMENSARBEIT Nr. 60
August 1998

Development of a Process-Based Model to Derive Methane Emissions from Natural Wetlands for Climate Studies
Bernadette Walter

EXAMENSARBEIT Nr. 61
Dezember 1998

On the benefit of the adjoint technique for inversion of the atmospheric transport employing carbon dioxide as an example of a passive tracer
Thomas Kaminski

EXAMENSARBEIT Nr. 62
Januar 1999

Modellierung der Chemie der globalen Strato- und Troposphäre mit einem drei-dimensionalen Zikulationsmodell
Benedikt Steil

EXAMENSARBEIT Nr. 63
Januar 1999

Ocean-atmosphere interactions on decadal timescales
Stephan Venzke

EXAMENSARBEIT Nr. 64
März 1999

Modes of Variability as Simulated by a Global Climate Model
Axel Timmermann

EXAMENSARBEIT Nr. 65
Juli 1999

Numerical Simulation of Scavenging Processes in Explosive Volcanic Eruption Clouds
Christiane Textor

EXAMENSARBEIT Nr. 66
Juli 1999

Grobstruktursimulation - eine Methode zur Berechnung turbulenter atmosphärischer Strömungen
Andreas Chlond

EXAMENSARBEIT Nr. 67
Dezember 1999

Satellitengestüzte Abschätzung der Einflüsse von kühler Haut und Schaumbedeckung des Ozeans auf den globalen CO_2-Fluß zwischen Ozean und Atmosphäre
Stefan Ewald

EXAMENSARBEIT Nr. 68
Februar 2000

Die direkte Strahlungswirkung von Aerosolteilchen auf ein Klimamodell
Anke Maria Allner

EXAMENSARBEIT Nr. 69
Februar 2000

Räumliche und zeitliche Variabilität von Wasserisotopen im polaren Niederschlag
(Spatial and Temporal Variability of Water Isotopes in Polar Precipitation)
Martin Werner

EXAMENSARBEIT Nr. 70
März 2000

Bestimmung des turbulenten Impulsflusses mit Hilfe von Doppler- und Interferometriemessungen eines Radar-RASS-Systems
Lutz Hirsch

EXAMENSARBEIT Nr. 71
Mai 2000

Entwicklung und Test eines massenerhaltenden semi-Lagrangschen Transportverfahrens auf einer Kugel
Markus Peter Olk

EXAMENSARBEIT Nr. 72
Mai 2000

Quantification of Natural Climate Variability in Paleoclimatic Proxy Data Using General Circulation Models: Application to Glacier Systems
Bernhard K. Reichert

EXAMENSARBEIT Nr. 73 Mai 2000	**Validation of Clouds in the ECHAM4 Model Using a Dynamical Adjustment Technique** Hans-Stefan Bauer
EXAMENSARBEIT Nr. 74 Juni 2000	**The Dynamical Link Between the Troposphere and Stratosphere and its Potential to Affect Climate** Judith Perlwitz
EXAMENSARBEIT Nr. 75 Juli 2000	**Fernerkundung von Eis- und Mehrschichtbewölkung über Meeresuntergrund aus Messungen rückgestreuter Solarstrahlung** Claudio Costanzo
EXAMENSARBEIT Nr. 76 Juli 2000	**Large-scale SST variability in the midlatitudes and in the tropical Atlantic** Dietmar Dommenget
EXAMENSARBEIT Nr. 77 Juli 2000	**HOAPS: Eine neue Klimatologie des Süßwasserflusses an der Meeresoberfläche abgeleitet aus Satellitendaten** Volker Jost
EXAMENSARBEIT Nr. 78 September 2000	**The potential influence of natural climate variability and uncertainty in the design of optimal greenhouse gas emission policies** Victor Ocaña
EXAMENSARBEIT Nr. 79 Oktober 2000	**Messungen des Reflexionsvermögen der Meeresoberfläche im infraroten Spektralbereich mit dem „Ocean Atmosphere Sounding Interferometer System" (OASIS)** Lars Fiedler
EXAMENSARBEIT Nr. 80 November 2000	**Vertikalmessungen der Aerosolextinktion und des Ozons mit einem UV-Raman-Lidar** Volker Matthias
EXAMENSARBEIT Nr. 81 Dezember 2000	**Photochemical Smog in Berlin-Brandenburg: An Investigation with the Atmosphere-Chemistry Model GESIMA** Susanne E. Bauer